2022

Passivity-Based Numerical Modeling and Grid Integration Strategies For Wave Energy Converter Arrays

Salman Husain
Michigan Technological University, shusain@mtu.edu

PASSIVITY-BASED NUMERICAL MODELING AND GRID INTEGRATION STRATEGIES FOR WAVE ENERGY CONVERTER ARRAYS

By

Salman Husain

A DISSERTATION

Submitted in partial fulfillment of the requirements for the degree of

DOCTOR OF PHILOSOPHY

In Mechanical Engineering - Engineering Mechanics

MICHIGAN TECHNOLOGICAL UNIVERSITY

2022

This dissertation has been approved in partial fulfillment of the requirements for the Degree of DOCTOR OF PHILOSOPHY in Mechanical Engineering - Engineering Mechanics.

- Department of Mechanical Engineering - Engineering Mechanics

Dissertation Advisor: *Dr. Gordon G. Parker*

Committee Member: *Dr. Wayne W. Weaver*

Committee Member: *Dr. Hassan Masoud*

Committee Member: *Dr. Guy Meadows*

Department Chair: *Dr. Jason R. Blough*

Dedication

To my Mother, Lubna, for all her sacrifices and for teaching me resilience, and my Father, Shadman, for showing me the meaning of diligence. Their unwavering support and unconditional faith in my success often perplexed me. They sacrificed everything they could and more.

To my Grandfather, Ashraf Zaman, for giving me my first book, telling me I was special, and that I mattered.

Contents

List of Figures

List of Tables

Preface

This thesis reused some content published as a conference paper and a journal article. The pertinent permission letters are appended as Appendix C. Chapter 4 draws content from a conference paper co-authored with Dr. Gordon G. Parker. He contributed towards defining the scope of the work, helping and checking the results, and editing the draft before submission. Chapter 6 draws from a published journal article, co-authored with Dr. Gordon G. Parker and Dr. Wayne W. Weaver. Dr. Parker contributed by helping with the analysis, checking the results and in the drafting of the original manuscript. Dr. Weaver contributed by checking the results and proof-reading the submitted manuscript.

Acknowledgments

> . . . There was so much I ought to have recorded, so many lives that have vanished - families, neighbours; people whose pockets were worn thin by hope. They were the loose change history spent without caring. Now they have become the air I breathe,. . .
>
> *- Excerpt from 'The Betrayal'*
>
> *Brian Patten, Liverpool*

I would like to express my deep gratitude to my advisor Dr. Gordon G. Parker. He has been an excellent mentor over the course of what is now almost five years. He has been generous in more ways than I can enumerate. If not for him I would not have been able to even start this PhD let alone look forward to taking up research as a career. Thanks to him I am hopeful about starting a career rather than doing a job. Back in the Summer of 2017, I was about to buy my tickets out of Houghton when he took me on board. He has been very supportive and has patiently taught me so many things, virtually holding my hand whenever I needed help, and often when I didn't know I needed help. He has taught me how to approach situations and problems, and I believe I would always trust his advice. I am grateful to have his trust, and the many opportunities and doors he opened up for me.

I would also like to thank the members of my committee Dr. Wayne W. Weaver, Dr. Hassan Masoud, and Dr. Guy Meadows. I am fortunate to be assessed by this committee of highly accomplished researchers. Their expertise in controls engineering, electrical engineering, fluid dynamics, and marine engineering would help assess this work from multi-disciplinary vantage points - all of which intersect at Wave Energy Converter (WEC) research and development. I am also thankful to the Mechanical Engineering-Engineering Mechanics Department for supporting me over the years. The department offered helpful courses and opportunities that helped deepen my understanding of dynamics and controls.

I was introduced to the field by Dr. Jiajun Song, Dr. Jianyang Lyu, and Dr. Shangyan Zou. I would especially like to thank Dr. Jiajun Song for teaching me WAMIT and the fundamental principles behind Wave Energy Converters. They introduced me to their advisor Dr. Ossama O. Abdelkhalik who invited me to participate in his research group's weekly meetings. I would like to extend my gratitude to Dr. Ossama O. Abdelkhalik and his research group for preparing me for this field and help appreciate the many areas and disciplines that are applied in marine energy research.

I am very thankful to Dr. Umesh A. Korde, who formally introduced me to marine energy research. He motivated me to work on the numerical modeling of wave farms (or more formally WEC arrays) which eventually became the primary theme of my

research. I have had the privilege of working with some of the most eminent experts in the field, thanks to the halo effect from my association with Dr. Parker. I would like to thank Dr. Enrico Anderlini from University College London, for his insights and sincere guidance whenever I needed his opinion. I would also like to thank Dr. David Forehand from the University of Edinburgh, for teaching me some of the intricate nuances of numerical modeling of WEC devices.

I have had the honor of working and learning - and it wouldn't be a hyperbole, from some of the global experts on the field at the National Renewable Energy Laboratory (NREL). I am very grateful to Dr. David Ogden, Dr. Nathan Tom, Dr. Thanh Toan Tran, and Dr. Yi-Hsiang Yu for involving me in some of their most interesting projects. They have been patient and approachable. They helped me polish up my numerical modeling skills and taught me some of the many techniques that I probably would not have ever known on my own. Thanks to them I could improve many of the analyses in this thesis and my research in general.

I am deeply indebted to my former advisor Dr. Oluremi A. Olatunbosun from the University of Birmingham (UK). If not for Dr. Olatunbosun, I wouldn't have had developed an interest in dynamics and controls.

I would like to thank my friends and colleagues, Robert Jane, Eddy Trinklein, Elizabeth VanHeusden, Serife Basbayandur, and John Naglak - for times that will always be on the wall of good old days.

I would especially like to thank my cat, Hammond, whose affection and friendship kept me happy and motivated.

Finally, I would like to thank McCall for believing in me especially when I couldn't myself, and to her parents for their support and encouragement.

Working towards my PhD, I learnt how to learn and desire a love for knowledge. I had more help than I know about, from places and people I didn't thank enough. I am grateful for the kindness and patience that I have experienced.

Abstract

The body of work presented here develops numerical time-domain models of Wave Energy Converter (WEC) arrays or wave farms. It will be shown here that a cluster of WECs can be more effective in extracting oceanic energy, can facilitate deployment logistics, and help with grid integration. The objectives of this work are: (i) developing a theoretical metric to evaluate the energy extraction potential of a WEC array, (ii) developing an algorithm that ensures the stability of the time-domain models of WEC arrays, and (iii) identifying strategies that facilitate grid integration and power management of a WEC array. In the process of developing the theoretical performance metric, the potential theory was used to develop expressions for wave potentials as the incoming wave reflects by and transmits through the WEC array. Decomposing the wave potential in horizontal and vertical parts enabled the application of boundary conditions based on continuity in terms of velocities and potentials. Incorporation of the hydrodynamic terms showed an increase of up to 28% in the low-frequency range. The knowledge of the wave potentials in and around the WEC array helped the application of robust system identification strategies that accurately described the physical phenomenon and ensured the numerical stability of the numerical models. The dissipative nature of the system enabled the application of the passivity property for system identification. The proposed approach could guarantee the numerical stability of time-domain modeling of WEC arrays while also ensuring

high accuracy of the emulated hydrodynamics and the motions of the bodies. For the case studies considered, the identified systems calculated the motion time-histories with $> 95\%$ accuracy for WEC array cases and $> 99\%$ accuracy for the single isolated body case. Finally, the dissertation addresses the grid integration and power management issues associated with the power generated by WEC arrays. The oscillatory nature of ocean waves introduces variability in the total power produced. This work develops the conditions that exploit the phase offsets in the wave received at individual WECs at any given time. The conditions developed here will result in constant power by imposing polyphase power profiles for the WECs in the array. Continuously constant power is desirable for grid integration and power management. Additionally, the objectives for an ideal power controller are developed that can make the overall produced by the WEC array constant.

Chapter 1

Introduction

> All models are wrong, but some are useful.
>
> George E. P. Box

This dissertation focuses on developing time-domain numerical models of WEC arrays that can facilitate effective model-based motion control and minimize the obstacles for grid integration. This work does not focus on control but develops numerical models that can be a robust framework for motion control design. This work takes a modular approach to the numerical modeling of WEC arrays such that the time-domain models developed can be integrated with and assist the onboard energy management. This Chapter discusses the motivation for working on WEC arrays, followed by the dissertation outline.

1.1 Motivation

Maintaining a competitive edge in the ongoing fourth industrial revolution requires automation of the manufacturing, services, and food production industries and can only be achieved through energy independence [104, 131]. Climate change and resource exhaustion necessitate that future energy needs have to be sourced from renewable sources. Oceans will exhibit the most manifest effects of climate change. These effects will range from rising sea levels and frequent hurricanes affecting coastal population centers to disruption of ocean currents resulting in the collapse of entire ecosystems. Oceans remain more unexplored than the Lunar, Martian, and Venusian surfaces [105, 125]. This has resulted in the lack of general awareness of the increased oceanic pollution. The accumulation of oceanic pollution such as the great pacific garbage patch, destroys delicate ecosystems and endangers a significant proportion of the human food supply [126]. The National Oceanic and Atmospheric Administration [124] and the National Geographic [28] cited the work by Peng et al. [90], reporting that plastic waste and other effects of pollution can now be found in the deepest reaches of the world's oceans, all the way down to the Mariana Trench (a US national monument [121, 128, 130]).

Exploring and understanding ocean environments could assuage the damage to marine ecosystems while the immense energy stored in the world's oceans can supplement

future energy needs. Oceans can serve as the most energy-dense renewable resource. Energy extraction from oceans can support a significant amount of future energy needs, considering that over 33% of the global population lives within 60 miles of an oceanic coast. Interestingly, around 40% of Americans live in coastal counties [127]. Marine energy can potentially provide 2.64 trillion kWh per annum in the United States alone [64]. Further exploration of versatile applications for marine energy can help support the 'Powering the Blue Economy' initiative by the US Department of Energy's Water Power Technologies Office [129].

Design and numerical modeling of Wave Energy Converter (WEC) devices is based on principles of offshore engineering, developed as an amalgamation of concepts from multibody dynamics, mechanical vibrations, fluid dynamics, marine hydrodynamics, and naval architecture. While marine-hydrodynamics guide the dynamical analyses of floating structures such as ships and offshore platforms, the energy extraction objectives of WECs require that the design and dynamical analyses incorporate principles of hydrodynamics in synchrony with WEC motion control and grid integration.

The design objective for a WEC could be suggested as being as straightforward as maximizing WEC motions. However, the design workflow is additionally influenced by other factors such as structural load-bearing capacity and fluctuations in the peak-to-average ratio of the power produced. Therefore, the design of a WEC should maximize energy extraction in a form that can be efficiently integrated into a grid

serving prospective energy customers.

The logistics of deployment and energy extraction efficiency considerations make a strong case for an array of WECs. A WEC array can desensitize the energy extraction dependence on the ocean-climate variability. Innovative marine microgrid solutions can support the energy demands of remote communities, scientific exploration, and the establishment of Forward Operating Bases (FOBs). Marine Energy Grids (MEGs) can address the aforementioned issues by reducing the dependency on traditional energy grids while expanding the scope of scientific research and exploration. Persistent sensing of offshore environments requires a robust energy supply for powering marine energy hubs serving energy customers such as Ocean Observation Buoys and Underwater Unmanned Vehicles (UUVs). Oceans have a high energy density, but this energy extraction is challenging because of the required infrastructure and the challenging working environment. WEC devices are good candidates for providing power to MEGs, producing, storing, and transferring energy at sea. Monitoring and exploration of oceans can be supported by deploying offshore remote energy hubs such as WEC arrays and offshore wind farms. An expected attribute of a MEG is that its energy production and storage may need to change over time due to changing at-sea electrical load requirements. Wave energy converter arrays offer a possible solution to the scalability requirement of MEGs.

1.2 Dissertation Outline

After discussing the relevant literature in Chapter 2, Chapter 3 highlights the Potential Theory-based modeling of oceans, both before and after the introduction of floating bodies. The Potential Theory-based mathematical description is then used to identify the equations of motion necessary for the time-domain modeling of WEC arrays. After laying the theoretical background required for the analyses of WEC arrays, the author's research is presented in Chapters 4 - 6.

A high-level outline is as follows:

1. Identifying a performance metric that evaluates the theoretical limit of the energy available for extraction in Chapter 4.

2. Proposing a novel algorithm to generate passive Linear Time-Invariant (LTI) WEC array models with high accuracy in Chapter 5. Ensuring the passivity property can help assuage numerical stability of MIMO systems such as WEC arrays,

3. Identifying WEC array layout-design criteria that reduce power fluctuation and storage requirements that can help the WEC array present itself as a constant source to the grid (Chapter 6).

1.2.1 Effects of Hydrodynamic Coupling on Energy Extraction Performance of Wave Energy Converter Arrays

The design space for a WEC array has many variables, including inter-WEC spacing, individual WEC output capacity, WEC type, array geometry, and the control approach. Although hydrodynamically decoupled analyses facilitate decentralized control, they miss a potential opportunity to exploit the hydrodynamic coupling of a more tightly packed array. A compact array model, parameterized with a non-dimensional WEC packing ratio, was proposed by Garnaud and Mei [45]. This work extended those results to include the hydrodynamic coupling between individual WECs in the array showing an increase in the theoretical energy extraction.

This analysis was then implemented on a numerical model using a 25-WEC, compact array example. The hydrodynamic radiation coefficients were generated using WAMIT (Wave Analysis MIT) and were incorporated into the dynamic equations introduced by Garnaud and Mei [45]. An energy extraction efficiency metric, considering the energy dissipated due to the waves reflected by and transmitted through the array, was used to quantify the effect of the added terms. Incorporation of the hydrodynamic terms showed an increase of up to 28% in the low-frequency range. This is significant for wave energy conversion as it corresponds to waves with higher speeds and wavelengths. Analyzing the theoretical limit of the energy available to the

WEC array helped quantify the effect of packing density on the potential for energy extraction, which can then inform the WEC array design.

1.2.2 Radiation Force Modeling for a Wave Energy Converter Array

This Chapter focuses on developing linear, stable models for the radiation force effects in floating marine structures, such as Wave Energy Converters (WECs), that can be used for model-based control strategies. Model-based control strategies need accurate dynamic models, in particular, for radiation force effects. The current state-of-the-art Linear Time-Invariant (LTI) WEC array modeling strategies do not guarantee passivity. Time-domain motion dynamics are commonly described using the Cummins' equation for floating bodies. Motion control can increase the energy extracted from a WEC array. The control design for WEC arrays, whether for analysis or implementation, is challenging because the Cummins' equation requires a convolution operation that calculates the radiation forces due to fluid-memory effects of the radiation field in real-time. This work presents a passivity-based approach to estimate radiation force transfer functions that accurately replace the convolution operation, preserve physical properties of the radiation Frequency Response Function (FRF), and ensure the stability of the motion dynamics model by explicitly enforcing passivity of the estimated transfer functions.

The approach developed here can be considered a frequency domain estimation method when the initial reference function is the radiation FRF $H_r(\omega)$, and a hybrid of frequency-domain and time-domain estimation methods when the initial reference function is the radiation Impulse Response Function (IRF) $h_r(t)$. The proposed approach has a final optimization routine that enforces the physical properties of the radiation FRF and minimizes the error between the magnitude and phase of the estimated transfer functions and the radiation FRF $H_r(\omega)$. The time-domain route further investigates that if the choice of numerical integration algorithm that calculates the radiation force IRF, and the estimated systems. This method preserves the physical properties of the radiation FRF, explicitly enforces passivity, and ensures the stability of the motion-dynamics model. The multibody dynamics involved in a MIMO system entail estimating transfer function arrays. The case studies presented contrast the effect of hydrodynamic couplings and interactions by comparing different layout configurations of a nine WEC array.

The effect of hydrodynamic coupling is investigated by comparing a sparsely spaced array and a compact array. This work presents a time-domain modeling framework for hydrodynamically-coupled multibody dynamics in floating body clusters. The proposed algorithm can be used for heterogeneous WEC arrays that may not have the same geometry. The transfer function array models developed here are an essential step towards designing motion control strategies that can respond to changing ocean conditions in real-time.

1.2.3 Storage Minimization of Marine Energy Grids using Polyphase Power

A maritime domain with gravity waves has significant spatial variability in phase, causing the power produced by a WEC array to have high peak-to-average ratios. Minimizing these power fluctuations reduces the demand for large energy storage by WEC array-powered DC microgrids while reducing losses in the undersea cable to the shore. Designs that minimize energy storage requirements are desirable to reduce deployment and maintenance costs. This work demonstrates that polyphase power, in conjunction with an energy storage system, can maintain constant power. It is shown that an N WEC array geometry can be designed to reduce the energy storage requirements needed to mitigate the power fluctuations if the WEC array produces constant, polyphase power. The conditions that identify the wave frequencies and control effort required to produce polyphase power are developed. Increasing the number of WECs in an array reduces aggregate power fluctuations. Finally, the simulated WEC array power profiles are investigated to verify the mathematical conditions developed for a three and six WEC case.

Chapter 2

Literature Review

After presenting a general background on WECs and WEC arrays, this Chapter discusses the relevant literature on the three major themes of this dissertation. Section 2.2 reviews the research on different assumptions, analyses methods, and numerical modeling approaches used for WEC arrays. The time-domain modeling with motion control requires the system's Linear Time-Invariant (LTI) model. However, the motion simulation of LTI models of WEC arrays is challenged by numerical stability issues. Section 2.3 starts with discussing different time-domain LTI models and their applicability to Multiple Input Multiple Output (MIMO) models needed for simulating a WEC array. This is followed by a discussion on the challenges in the grid integration of WEC arrays in Section 2.4.

2.1 WECs and WEC Arrays - Background

Clément et al. presented a detailed review of the state of WEC research in 2002 [14]. They outlined the historical development and prominent research institutes around Europe and discussed the wide variety of WEC devices investigated over the years. They identified that Denmark, Ireland, Norway, Portugal, Sweden, and the United Kingdom were the earliest to consider wave energy as a viable energy source. However, the earliest interest in extracting oceanic energy can be traced back to 1799 when a patent was issued to Girard and Son in France [14, 66, 101]. They also mentioned the work by Leishman and Scobie [72] which was commisioned by the UK Department of Energy - Wave Energy Programme 1974-1983. Leishman and Scobie documented 340 patents related to WECs starting from 1855 when the first British patent was issued, to 1973 [72]. The 1970s are often considered the starting point of modern WEC research [66, 76, 101].

The 1970s energy crisis motivated a renewed interest in wave energy [66]. Stephen Salter pioneered WEC research at the University of Edinburgh by introducing a tear-drop-shaped pitching device (The Salter Duck) in 1974 [41]. Soon after, numerical modeling and experimental validation were done by Count [17, 18], Mynett et al. [81], Serman [106], and [110]. Evans[29], Nebel [82], and Pizer [96] further researched the numerical modeling of WECs in general and the Salter Duck in particular.

Around the same time, Chiang C. Mei [79] at the Massachusetts Institute of Technology (MIT), John V. Wehausen at the University of California, Berkeley [136], T. Francis Ogilvie at the University of Michigan [86] advanced WEC research at American universities. Their work lead to the development of Boundary Element Method (BEM) based numerical solver WAMIT (Wave Analysis at Massachusetts Institute of Technology) [133]. Improvements in computational capabilities led to the development of numerical codes that solved Green's theorem to calculate the hydrodynamic coefficients needed for the numerical modeling of WECs.

Other notable work was carried out by Johannes Falnes, Thor I. Fossen, Reza Taghipour, and Tristan Perez at the Norges Teknisk-Naturvitenskapelige Universitet (NTNU), Norway. It led to the development of the Marine Systems Simulator (MSS) toolbox [37, 43, 92, 115]. WEC numerical modeling efforts at the École centrale de Nantes, France, led to the development of the numerical codes AQUADYN and AQUAPLUS by Delhommeau [22, 23], followed by the FORTRAN based code NEMOH [4, 60], and most recently the python-based BEM code CAPYTAINE by Ancellin [2]

Le Méhauté remarked that much of the early numerical modeling used the Linear Potential theory. Albeit its limitations, the linear wave theory has been extensively used for numerical modeling of WECs and was found to be satisfactory when compared to experimental validations. Le Méhauté presented a graphical summary (Figure 2.1) of

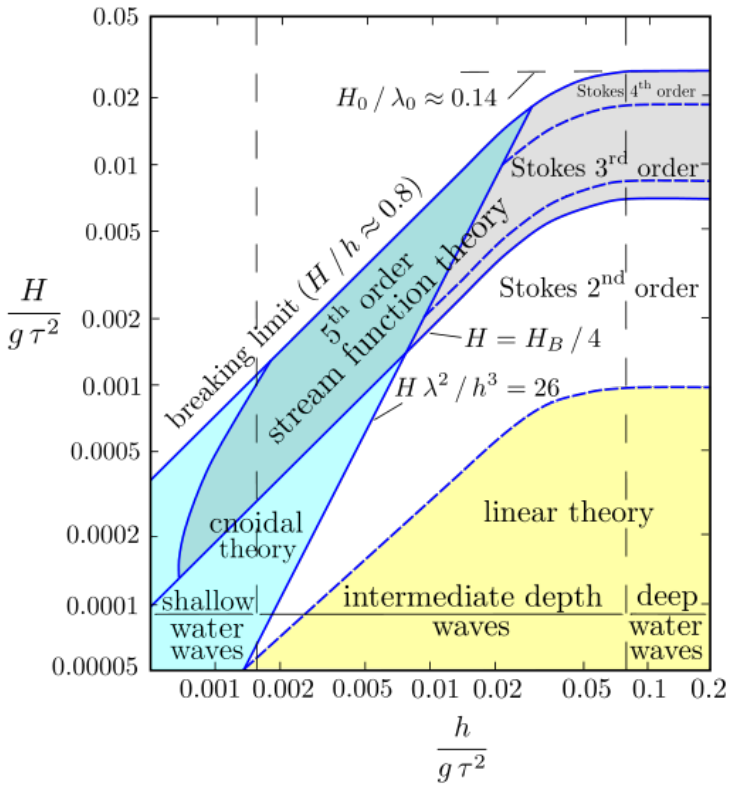

Figure 2.1: H is the wave height, τ is the wave period, and h is the water depth. Comparison of the validity of different wave theories and their assumptions by Le Méhauté [71].

the validity of different wave theories [71].

One of the foremost objectives of numerical solvers for hydrodynamics coefficients was to develop time-domain models. And early deployment efforts by Haren and Mei [54], Thomas and Evans [117] recognized the need for deployment of multiple WECs as a WEC array wave farm. Retzler conceptualized an array of Salter Duck devices on a a curved spine [98, 99]. Appendix A models a WEC array of Salter Duck devices on a curved spine. The Pelamis device can be considered evolution and physical

realization of the work by Retzler [140].

Chiang C. Mei showed that a compact WEC array could produce more power than the comparable single monolithic WEC [45]. However, the time-domain modeling of WEC arrays is beset by numerical instabilities when the radiation force is calculated using Linear Time-Invariant (LTI) models generated using system identification[42]. The LTI system identification of radiation force is crucial for control. This is because although the radiation force is smaller than the hydrostatic and excitation forces, it is crucial for dynamic stability and motion control. For instance, the complex-conjugate control which maximizes energy extraction relies on the accurate knowledge of the radiation damping term. The field has long recognized the significance of motion control, starting from Greenhow to the most recent developments in machine learning[3, 5, 51, 65, 100]. This dissertation does not focus on motion control. However, the motivation for the models developed here is for control design.

Physical deployment of WECs therefore needs,

1. The setting up of an array of WECs (Section 2.2,

2. Their time-domain Linear Time-Invariant (LTI) models,

3. And finally grid integration and power management strategies.

In the literature review that follows, the discussion starts with the performance metrics that have been used for WEC arrays in Section 2.2, followed by the time-domain modeling techniques that address the numerical instabilities in Section 2.3. Finally, the challenges to the grid integration of WEC arrays are reviewed in Section 2.4.

2.2 Performance metrics for Energy Extraction from WEC Arrays

Mavrakos and McIver present a comparison of hydrodynamic characteristics of WEC arrays [75]. They suggested three analysis methods

1. Multiple-scattering method,
2. Plane-wave method,
3. Point-absorber approximation method.

The multiple-scattering method combines the radiation and diffraction effects using a matched eigenfunction expansion with Hankel and Bessel functions.

The plane-wave method uses a wide-spacing approximation solving the diffraction and radiation problems for an isolated buoy. This method ignores the imaginary

eigenfunctions and, therefore, the evanescent modes.

The point-absorber approximation assumes the device to be smaller than incident wavelengths and uses the q-factor performance metric that is insensitive to device geometry and displacement. Mavrakos and McIver suggest these methods are a more practical model for only arrays with wider spacings operating at higher wavenumbers [75].

Göteman et al. used irregular short-crested waves in their analysis, capturing the radiation and diffraction effects for linear 2D arrays using the q-factor [53]. Using the multiple-scattering and point-absorber approaches to model the array in irregular waves, they included the effect of varying sea conditions where the devices were far apart. The wider spacing resulted in neglecting hydrodynamic coupling.

Whittaker and Folley used point-absorber assumptions to optimize for an interaction factor [137]. Child and Venugopal used genetic algorithms to optimize energy extraction efficiency [12]. McGuinness and Thomas also use the point-absorber approximation and optimized the q-factor for relatively close devices. Their results recommend devices that are far apart [77].

Ringwood and Bacelli proposed control strategies for WEC arrays by either taking a Global Control (GC) or an Independent Control (IC) approach [5] [100]. Their approach used the plane-wave and point-absorber assumptions to optimize q-factor

and was well-suited for sparse arrays.

Falnes and Budal considered infinite linear arrays parallel to each other. They introduced the 'array radiation resistance matrix,' which is affected by the array members and also by the groups of arrays [38] . Thomas and Evans considered arrays of three-dimensional WECs and corroborated Havelock's results for heaving spheres for a double row array [55, 117]. Two articles, Siddorn and Taylor and Walker and Taylor, discuss the trapping effect in an array such that the potential equation gets modified in the array region and, therefore, modify the hydrodynamics of the array members [108, 132].

Wider spacing poses practical problems to actual deployment and misses the opportunity that inter-array interactions can offer. In practical applications, the lower wave frequencies are more important from an energy extraction perspective as they correspond to waves with higher speeds [85]. It will be shown here that for lower wave frequencies, there is a considerable improvement in energy available for extraction in compact arrays due to hydrodynamic couplings.

2.3 Linear Time-Invariant System Estimation

Real-time motion control of a Wave Energy Converter (WEC) requires a time-domain model that captures the system's motion dynamics and hydrodynamic interactions. The Cummins ' equation has been typically used to describe time-domain dynamics for WECs [66, 85].

Marine structures emanate a radiation wave field when excited by an incoming wave-field, resulting in radiation forces [84]. Modeling motion dynamics using the Cummins' equation requires a convolution operation to calculate the radiation forces. The radiation force is causal and needs the body's velocity information in real-time for the convolution. The radiation force in the time-domain is calculated using the frequency domain hydrodynamic coefficients, solved using a Boundary Element Method (BEM) solver, such as commercial software packages like Wave Analysis MIT (WAMIT). The frequency-domain hydrodynamic coefficients are then used to calculate an Impulse Response Function (IRF). Convoluting the IRFs with the buoy velocity gives the radiation force in real-time. This model-based control design requires a transfer function matrix or state space realization of the system instead of the convolution model [91, 115]. The approach proposed in Chapter 5, circumvents the convolution operation by proposing an algorithm to generate a transfer function matrix between the radiation force and body velocities. A passivity-based approach ensures fidelity

to the physical system because radiation forces are dissipative in nature. Duarte et al. present a thorough comparison of different approaches taken by researchers over the years [26]. Their comparative review is expanded here with recent developments since their publication. The main approaches to approximate replacement for the convolution-based calculation of radiation force $\vec{F}_R(t)$ can be classified as,

1. Frequency domain estimation methods use the radiation function $H_r(\omega)$ to estimate state-space or transfer function models. The main routes taken are,

   (a) Identifying continuous-time filter parameters from frequency response data,

   (b) The moment matching method.

2. Time-domain estimation methods first numerically calculate the radiation IRF $h_r(t)$ and then use the IRFs to estimate state-space or transfer function models. The main routes taken for this approach are,

   (a) Curve fitting methods based on Least Squares curve fitting of the IRFs,

   (b) The realization theory method is based on Hankel Singular Value Decomposition (SVD), followed by order reduction strategies such as balanced-realization order reduction.

2.3.1 Frequency domain estimation methods

Frequency domain estimation methods estimate the radiation force transfer functions using the radiation FRF. These methods can be potentially more accurate than time domain methods because the two staged process of time domain estimation can introduce computational errors such as round-off errors. Additionally, time domain methods may introduce high frequency content in the estimated transfer function array, due to truncation of the reference functions (the radiation FRF and its IRF).

2.3.1.1 Identifying continuous-time filter parameters from frequency response data

Duarte et al. summarize the least-squares methods used over the years [26]. These methods minimize the least-squares error between the radiation function and the estimated LTI system, such that the quantity J is minimized,

$$J = \Lambda \left(H_r(\omega_l) - \tilde{H}_r(\omega_l) \right)^2 \tag{2.1}$$

where ω_l are the wave frequencies being considered for the optimization, spaced with the step size $\Delta\omega$, Λ is some weighting function, $H_r(\omega_l)$ is the radiation function, while

$\tilde{H}_r(\omega_l)$ is the frequency response of the estimated LTI system. The weighting function, Λ, is varied with the frequencies being considered, ω_l, such that the optimization effort can be biased for some particular values of the frequencies. This can be implmented by using the $invfreqs()$ command in MATLAB that uses a based on Gauss-Newton iterative search optimization. Originally developed for ship motions, this approach was developed at Norges Teknisk-Naturvitenskapelige Universitet - NTNU and is packaged as the Marine Systems Simulator (MSS toolbox) [92, 115].

The MSS toolbox has the FDI (Frequency Domain Identification) utility, approximating LTI models using the frequency-dependent radiation function $H_r(\omega)$. The FDI utility first filters out the frequencies with discontinuous points owing to numerical errors in the hydrodynamic coefficients data. The process also rejects zero frequency lines in the estimation process. The estimation process starts from a second-order system. Then the order is increased to improve the match in the frequency response of the estimated system and the radiation function $H_r(\omega)$. The package then iteratively reduces the error between the radiation IRF, and the approximated transfer function.

The estimation process then checks for unstable eigenvalues (eigenvalues with their real-part in the right-hand plane of the Laplace plane). If unstable eigenvalues are found, they are reflected about the imaginary axis by multiplying the positive real-parts by -1, and the estimation process is reinitialized with the new eigenvalues.

The rejection of zero frequency points and 'wild points' and the weighting process itself does risk losing the physical nuances of the marine system, especially for multiple bodies in WEC arrays. Iterative increase of orders also risks the overestimating issue discussed by Perez and Fossen [92]. The process requires the user to pick a frequency range for estimation. As pointed out by Perez and Fossen, the matches with this method work best for low-frequency ranges, and it does not guarantee stability and passivity [92]. Taghipour et al. also observe that the improper scaling of the input data can be crucial for numerical stability [115].

Forehand et al. also generate a transfer function and a state-space model, with the added feature that their code package can be used for a WEC array [42]. They estimate the transfer function using the $invfreqs()$ command in MATLAB by minimizing the root mean square error between the estimated transfer function's frequency response and the radiation effects' frequency response using the $freqreqs()$ command in MATLAB. These estimations are done for different orders, and the estimated transfer function with the least error is chosen. The order of the transfer function system is then minimized further to estimate the state-space model. The stability and conditionality for the estimated system are checked but not enforced in the estimation process.

2.3.1.2 The moment matching method

Recently, some promising developments have been made in frequency domain estimation methods. Faedo et al. at Maynooth University developed a novel approach using moment matching to estimate LTI systems [31]. In this context, a *moment* refers to the radiation function $H_r(\omega)$ at some specific frequency. The method uses a few points or *moments* on the $H_r(\omega)$. Faedo et al. then used these estimated models to devise an energy maximizing controller model [35]. They also extend this approach for an MDOF problem [33].

The moment matching method shows promising results with very low normalized root mean squared errors (NRMSE) between body motions calculated using their estimated system and those from the convolution [32, 34, 94]. This method relies on choosing the *moments* corresponding to the radiation function $H_r(\omega)$ peaks. However, this becomes difficult to judge if the $H_r(\omega)$ has a multi-lobed frequency response, especially for multibody MDOF systems. Although regular geometries like spheres and cylinders usually have a single-lobed $H_r(\omega)$, disparate marine structures or innovative WECs will have multi-lobed $H_r(\omega)$, making it difficult to choose the *moments*, especially in situations where coupled modes exist.

Similarly, WEC arrays, especially compact WEC arrays, will be a challenging system

for a moment matching-based method. When marine structures are in close proximity, such as in a compact WEC array, the velocity field within the area occupied by the structures gets modified. This results in a trapping effect which introduces the additional lobes in the hydrodynamic coefficients. These trapping effects are extensively discussed Eatock Taylor et al. [52, 108, 116]. Wolgamot et al. also described trapping effects in WEC arrays [138, 139]. These phenomena show that each frequency line is coded with critical hydrodynamic information about the system. Faedo et al. remarked that an additional constraint could introduce passivity to their optimization [31]. More recently, the same authors have proposed a passivity preserving method [30]. In that work, Faedo et al. introduced the conditions needed to guarantee passivity for a single body. In the numerical example shown, the authors selected a set of *moments* for a passive model. The accuracy for coupled modes, whose radiation damping characteristics usually have multiple lobes, can only be enforceable in a limited bandwidth [36, 88].

2.3.2 Time-domain estimation methods

Time-domain estimation methods are carried out in two stages: the numerical integration for the radiation IRF , followed by estimating an LTI system based on this radiation IRF. The general approach for the numerical integration for the cosine transform is to use either Euler integration or Trapezoidal integration methods. For

instance, NEMOH, developed by LHEEA Centrale Nantes, uses Euler integration [60]. Whereas the WEC-Sim package, developed by the National Renewable Energy Laboratory (NREL) and Sandia National Laboratories, uses the trapezoidal integration method by calling the $trapz()$ function in MATLAB [102]. Prony's method can also be used to calculate the radiation IRF, $h_r(t)$ [91]. However, Prony's method only works for single bodies. WAMIT uses the $f2t$ utility tool to output radiation IRFs using Filon's trapezoidal numerical integration (See Chapter 13 of the WAMIT manual for the $f2t$ utility manual)[133]. The WAMIT manual for the $f2t$ utility recognizes that the Fourier transform (and more specifically, the cosine transform for the radiation IRF) is more accurately calculated by Filon's integration method, especially for large values of the time variable.

2.3.2.1 The Least Squares (LS) curve fitting method

Yu and Falnes presented their, in some ways, pioneering work, outlining the different ways the real-time convolution could be circumvented [142]. They proposed that the estimated system may need a higher-order approach to describe the radiation IRF. Yu and Falnes used numerical integration to form companion form matrices for the radiation and excitation forces. However, the stability and passivity properties of the estimated state-space models were not considered. Taghipour et al. point out that the LS methods result in LTI systems whose frequency responses have very poor matches

with the respective radiation function $H_r(\omega)$ [115].

Another notable example of an LS curve fitting model was presented by Alves et al. [1]. They used the MATLAB function *prony* to find a discrete transfer function. However, this method does not ensure stability, especially for higher-order radiation functions [26].

2.3.2.2 The Realization theory method using the SVD Hankel decomposition

Unneland et al. and Kristiansen et al. created a state-space realization using the Markovian property of state-space models [69, 122, 123]. The MATLAB function $imp2ss$ can be used for the SVD Hankel decomposition. Additionally, Taghipour, Perez, and Fossen showed that overfitting could be mitigated by a balanced order reduction using the *balmr* command in MATLAB [91, 115]. This approach does not enforce stability or passivity, although Taghipour et al. and Perez et al. recognize that the approximation process should ideally result in a passive LTI system. Perez and Fossen point out that the realization theory method does not necessarily satisfy the low-frequency asymptotic values and the relative degree requirements of the radiation function $H_r(\omega)$ [91, 115]. This approach has been widely cited and was incorporated in the WEC-Sim package developed by Sandia National Laboratories and National

Renewable Energy Laboratory (NREL) [102]. Subsequent reports published by Sandia National Laboratories highlight the difficulty of ensuring stability for a complete dynamics model that has the radiation force implemented as negative feedback [15]. However, this approach will become difficult to implement for a multibody MDOF system.

2.4 WEC Array Design to Facilitate Grid Integration

A significant hurdle in mainstream adoption of marine energy is the lack of consensus and research in grid integration strategies [42, 97]. While wind and solar energy devices have largely achieved design convergence facilitating their grid integration strategies, marine energy, and especially wave energy research, is still exploring different devices and their respective grid integration [8, 42, 97, 118]. Preziuso et al. presented a literature review on grid integration of marine energy assets [97]. They surveyed the grid integration viability for wave energy, tidal energy, and ocean current energy assets. They further identified that the grid integration of marine energy assets requires arrays of multiple marine energy assets integrated as microgrids. The fluctuation of waves in nature causes power and voltage fluctuations in a WEC's Power Take-Off (PTO). The power fluctuations from a WEC can be mitigated by WEC

array control, aggregation of a large number of WECs in an array, and using energy storage systems (ESS) [8, 42, 97, 118]. WEC arrays that produce constant power are desirable as they (1) reduce storage requirements and (2) reduce transmission losses.

The motivation of the work discussed later in Chapter 5, is to explore ways to achieve constant power through design and WEC force control, thereby facilitating the grid integration of WEC arrays. The ESS can be supplemented by control action so that the power injections from the WEC array are maximized while ensuring that the power fluctuations are minimized.

Sjolte et al. showed that ESS could reduce the WEC array's power fluctuation by as much as 18 % [109, 112]. They recognized that ESS is essential to mitigate power fluctuation in a MEG. They also analyzed the Levelized Cost of Energy (LCOE) and showed a cost analysis of using a battery as the ESS for a MEG operating at six different sea-states. Yu et al. showed that power smoothing techniques could reduce power fluctuation in a MEG by an order of magnitude and thereby directly affect the LCOE [141].

The mitigation of power fluctuation using ESS for the WEC array microgrid can be accomplished using a battery as investigated by Stefek et al. , a super-capacitor proposed by Brando et al. or a hybrid of battery and super-capacitor as modeled by Parwal et al. [8, 87, 112]. Brando et al. base their ESS selection on power quality, bridging power, and energy management [8]. They also considered the charging and

discharging response times of various ESS to maintain the microgrid's bus voltage during power shortfalls. They control the microgrid such that the ESS is connected to the DC side of their circuit through a buck-boost chopper as the DC side interfaces with a three-phase AC grid (AC side) using a Voltage Sensitive Relay (VSR). The VSR control ensures that the active power transfer with the grid from the DC side is as constant as possible. At the same time, the ESS absorbs the excess power produced instantaneously by the WECs or compensates for the shortfalls as needed to maintain the bus voltage. Zhou et al. presented a numerical framework for sizing ESS for WEC applications [143]. They also show that the dynamics and the motion-control of the WEC and control strategy of the electrical drive must be integrated to model the ESS accurately [143].

The physical nature of oceanic waves entails phase offsets in the wave elevations received at individual members of a WEC array as a function of array layout. Rollano et al. quantified the effect of phase information on the power output of a virtual WEC array [118]. They compared the power output performance of a WEC array in a phase-averaging wave model using Simulating WAves Nearshore (SWAN) against a phase-resolving wave model FUNWAVE-TVD [11, 107]. A phase-averaging wave environment can be used for a WEC array with a large number of WECs because each WEC at a different location in the array will have the opportunity to sample a different phase of the incoming wave to reduce the variability of the aggregate power [118]. However, they point out that power systems are vulnerable to large wave amplitudes

making a phase-resolved wave environment crucial to avoid underestimating such wave events. Rollano et al. conclude that the phase-resolving wave environment is especially apposite for modeling arrays with a small number of WECs.

Tidal energy researchers have identified the theoretical advantages of using multiple tidal energy assets installed such that they produce staggered power profiles at mutually complementary phase differences [97]. The advantage thereof is that the sum of the power profiles generated at staggered phases is a relatively smooth power profile that can theoretically be a constant flat-line power profile. Giorgi and Ringwood used a multi-objective optimization to evaluate eleven tidal energy sites around Ireland. Their optimization simultaneously maximized the mean power and the minimum power while minimizing variance by minimizing the variance in the total power by using two variables at each site: number of installed turbines and type of installed turbines [49]. Preziuso et al. remark that the multi-objective optimization used by Giorgi and Ringwood often have conflicting objectives. Clarke et al. also acknowledge the practical challenges in generating staggered power profiles using tidal energy assets [13].

Interestingly, the phase profile of gravity waves varies over much more local scales when compared to the phase profiles of tidal energy harvesting sites. This implies that the staggered phase profiles received at each WEC in an array can be capitalized such that the phase of the power produced by each member of the WEC array is

complementary to each other, and the array produces constant power.

Renewable energy assets produce stochastic power, and therefore many researchers have used DC microgrids for their grid integration [16, 119, 134]. Cook et al. showed the advantages of using a mode-adaptive control scheme over decentralized N-state droop control, either of which can be a compelling control strategy as a localized WEC array control law [16]. A bi-directional flow of power between the WEC array and the microgrid can further enhance the power produced by the WEC array using control action. Forehand et al. observed that not much work has been done on the coupling of WEC arrays and electrical grids, and even less work has been done on a bi-directional coupling between a WEC array and electrical grid [42]. They introduced a bi-directional WEC array model that was coupled with a microgrid. Their bi-directional model can be used to identify individual and collective contributions to the power quality, as well as the effect of the power faults in the microgrid on the PTO. Active control of WEC arrays supplemented with ESS can further mitigate voltage fluctuation in the microgrid [97].

by

Chapter 3

The Nature of Ocean Waves, Hydrodynamics of Floating Bodies, and their Time-Domain Models

This Chapter will discuss the general characteristics of oceanic waves, identify the pertinent boundary conditions and relations that affect the general motion of floating bodies and the hydrodynamic effects surrounding them. Ocean waves can be generated by a wide range of natural phenomena such as the Coriolis effects from earth's rotation, astronomical gravitation: tides, weather patterns, plate tectonics:

tsunamis, among others. This Chapter discusses hydrodynamics theory drawing extensively from the works by Sir Lamb, Newman, Falnes, Folley, and Korde & Ringwood [37, 40, 66, 70, 85].

3.1 Nature of Ocean Waves - Potential Theory

Oceanic waves are often described using a linear combination of sinusoidal waves as a consequence of the sinusoidal-series summation techniques introduced by Jean-Baptiste Joseph Fourier [44, 113]. Discussion on the hydrodynamics governing equations and the boundary conditions were formally compiled and discussed by Sir William Thomson (Lord Kelvin) [61, 62]. The periodic nature of the waves can be expressed as a field effect in terms of the velocity potential of the fluid. The contributing sinusoidal waves can then also be expressed in terms of the wave velocity potential as described in the correspondence between Lord Kelvin and Sir Stokes [114], further elaborated by Sir Stokes in the compilation of his hydrodynamics related works [113].

Let $\Phi(x, y, x; t)$ represent the wave velocity potential. Assuming two-dimensional waves such that all changes in displacements and pressure occur in the XZ-plane. The wave velocity potential can be written as,

$$\Phi(x, z; t) = P(z) \sin(kx - \omega t) \tag{3.1}$$

Where $P(z)$ is some function of z, and the wave propagates along the positive X-axis (left-to-right). The wave velocity potential can describe the wave characteristics and the forces the waves impose on floating bodies through hydrodynamic interactions. The work by Journee and Massie [27] summarized the conditions that the wave velocity potential $\Phi(x, y, z; t)$ is required to satisfy,

1. Continuity condition - Laplace equation,

2. Sea-bed boundary condition,

3. Free-surface kinematic boundary condition - Cauchy-Poisson Condition, and,

4. Free-surface dynamic boundary condition.

The above conditions help relate the temporal frequency ω and the spatial frequency or the wave-number k using the dispersion equation.

3.1.1 Continuity condition - Laplace equation

Assuming the fluid is ideal, surface tension can be neglected Linearized relations by ignoring the second order and higher order terms. The continuity condition can be represented as,

$$\vec{v} = \nabla\Phi = \frac{\partial\phi}{\partial x} + \frac{\partial\phi}{\partial y} + \frac{\partial\phi}{\partial z} \tag{3.2}$$

which can then be expressed as,

$$\nabla^2\Phi = \frac{\partial^2\phi}{\partial x^2} + \frac{\partial^2\phi}{\partial y^2} + \frac{\partial^2\phi}{\partial z^2} = 0 \tag{3.3}$$

Equation 3.3 represents the Laplace equation. Imposing the Laplace equation on Equation 3.1,

$$\nabla^2\Phi = \frac{d^2P(z)}{dz^2} - k^2P(z) = 0 \tag{3.4}$$

The general solution of which will be of the form,

$$\Phi(x, z; t) = (C_1 \exp +kz + C_2 \exp -kz) \sin(kx - \omega t) \tag{3.5}$$

Where C_1 and C_2 are some constants that shall be determined using the boundary conditions identified in the rest of this Section.

3.1.2 Sea-bed Boundary Condition

Assuming an impermeable sea-floor at a depth of $-h$, the boundary condition at the sea-floor ($z = -h$)becomes,

$$\frac{\partial \phi}{\partial z} = 0, \quad \text{at } z = -h \tag{3.6}$$

Now imposing the boundary condition in Equation 3.6 on Equation 3.5,

$$kC_1 \exp(-kh) - kC_2 \exp + kh = 0 \tag{3.7}$$

Therefore, the general solution can now be written as,

$$\Phi(x, z; t) = C \cosh\left(k(h + z)\right) \sin\left(kx - \omega t\right) \tag{3.8}$$

Where the constant C shall be determined by imposing all of the boundary conditions discussed in this Section.

3.1.3 Free-surface kinematic condition - Cauchy-Poisson Condition

The free surface kinematic condition was introduced in detail by Cauchy [10] and then Poisson, and discussed in a more accessible form by Pidduck [95], Sir Lamb [70], and then Craik [19]. The exact kinematic boundary condition can be written by equating the substantial derivative (represented by upper-case D) of the wave elevation η with that of vertical displacement z, such that,

$$\frac{D(z-\eta)}{Dt} = \frac{\partial \phi}{\partial z} - \frac{\partial \eta}{\partial t} - \frac{\partial \phi}{\partial x}\frac{\partial \eta}{\partial x} - \frac{\partial \phi}{\partial y}\frac{\partial \eta}{\partial z} = 0 \tag{3.9}$$

If η is small enough, the partial derivative terms representing the slopes $\frac{\partial \eta}{\partial x}$ and $\frac{\partial \eta}{\partial z}$ can be ignored such that,

$$\frac{\partial \phi}{\partial z} = \frac{\partial \eta}{\partial t} \tag{3.10}$$

Which represents the approximate boundary condition at the free surface such that the vertical velocity of the free surface and fluid particles are equal.

3.1.4 Free-surface Dynamic Boundary Condition

Conservation of mass can be represented using Bernoulli's equation, such that the

$$\frac{p}{\rho} + \frac{\partial \phi}{\partial t} + \frac{1}{2}\nabla\phi.\nabla\phi + g\eta = \text{Constant} \tag{3.11}$$

Substituting η for z and linearizing the taylor series expansion of ϕ at the free-surface ($z = 0$ plane), gives the free-surface dynamic boundary condition,

$$\frac{\partial \phi}{\partial t} + g\eta = 0 \tag{3.12}$$

the derivative of which can be written as,

$$\frac{\partial^2 \phi}{\partial t^2} + g\frac{d\eta}{dt} = 0 \tag{3.13}$$

Note, the derivative of Equation 3.13 can be combined with the free-surface kinematic boundary condition to arrive at a single boundary condition equation,

$$\frac{\partial^2\phi}{\partial t^2} + g\frac{d\phi}{dz} = 0 \quad \text{at the plane, } z = 0 \tag{3.14}$$

3.1.5 General equation for wave velocity potential $\Phi(x, z; t)$

The wave elevation using Equation 3.8, and with $z = 0$, can be expressed as,

$$\eta = -\frac{\omega C}{g}\cosh(kh)\cos(kx - \omega t) \tag{3.15}$$

Eliminating the constant C by substituting Equation 3.15 in 3.8, the general wave velocity potential can be written as,

$$\Phi(x, z; t) = \frac{g\eta}{\omega}\frac{\cosh(k(h+z))}{\cosh(kz)}\sin(kx - \omega t) \tag{3.16}$$

3.1.6 Dispersion relation

Substituting the free-surface kinematic condition, Equation 3.10 in Equation 3.15

$$-\omega^2 C\sinh(k(h+z))\sin(kx - \omega t) + gkC\cosh(k(h+z))\sin(kx - \omega t) = 0 \tag{3.17}$$

equating $z = 0$ and simplifying,

$$\frac{\omega^2}{g} = \pm \tanh(kh) \tag{3.18}$$

Equation 3.18 is commonly referred to as the dispersion equation. The solution of Equation 3.18 when the right side of the equation is positive results in positive and real eigenvalues, while the complex eigenvalues are discussed in further detail in Chapter4.

3.2 Hydrodynamics of Floating Bodies

In this Section, the potential theory is extended to the situation when the fluid domain contains floating bodies. The presence of the floating bodies alters the wave velocity potentials as the incoming wave potential interacts with the floating bodies, and consequently, the floating bodies emanate a potential field. The expressions for the potential theory and their boundary conditions are then used to identify expressions for the hydrodynamic coefficients, forces, and moments.

3.2.1 Potential Theory in the Presence of Floating Bodies

The Bernoulli's equation while retaining only the first order ($O(n)$) terms, can also be seen as an expression for dynamic pressure. The general form of hydrodynamic forces ($\vec{F_{hd}}$) and moments ($\vec{M_{hd}}$) acting on a body can be expressed by integrating the dynamic pressure over the immersed surface area, S_b, such that,

$$\begin{pmatrix} \vec{F_{hd}} \\ \vec{M_{hd}} \end{pmatrix} = -\rho \iint_{S_b} \frac{\partial \Phi}{\partial t} \begin{pmatrix} \vec{n} \\ \vec{r} \times \vec{n} \end{pmatrix} \, dS_b = -\rho \iint_{S_b} \left(\frac{\partial \Phi}{\partial t} + gz \right) dS_b \tag{3.19}$$

where the velocity potential, $\Phi(x, y, z; t)$ has contributions from the incoming wave field and the resulting wave field emanating from the floating body due to the diffraction and radiation effects. Consider plane progressive waves that are two-dimensional and oscillate in the XZ-plane, with an amplitude A, then the real part of velocity potential can be expressed as,

$$\Phi(x, y, z; t) = \Re \left(\left(\Sigma_{j=1}^{6} \eta_j \phi_j(x, y, z) + A \Phi_A(x, y, z) \right) e^{i\omega t} \right) \tag{3.20}$$

Where the real part is represented here using the notation $\Re$. The $\Sigma_{j=1}^{6} \eta_j \phi_j(x, y, z)$ terms correspond to the *radiation* problem and represent the velocity potential of the body motion with unit amplitude without any contributions from the incoming waves, i.e., in otherwise calm water. Alternatively stated, the $\Sigma_{j=1}^{6} \eta_j \phi_j(x, y, z)$ terms

correspond to the velocity potential if the body were floating in still water and then an external actuator were to act on the body, causing the body to oscillate with unit amplitude. The forces and moments act on the body as an equal and opposite reaction to the wave field radiated by the body due to its motion (as though there were no incoming waves) are the radiation forces.

The $A\Phi_A(x, y, z)$ terms correspond to the wavefields generated due to the incoming waves and their interactions with the body and are solutions to the *diffraction* problem. The forces and moments due to the incoming wave field agnostic to the body are the Froude-Krylov forces. The incoming wave fields interact then with the body and are scattered, i.e., diffracted by the body, as though it were held fixed, resulting in the diffraction forces and moments.

3.2.1.1 Body Surface Boundary Conditions

The ϕ_j terms for $j = 1, 2, ..6$, are subject to the boundary condition that the normal derivative of $\Phi(x, y, z; t)$ in Equation 3.20 should be same as the normal velocity of the body on the body surface, S_b, such that,

$$\frac{\partial \phi_j}{\partial n} = i\omega n_j, \quad j = 1, 2, 3 \quad \text{and,} \ \frac{\partial \phi_j}{\partial n} = i\omega(\vec{r} \times \vec{n})_{j-3}, \quad j = 4, 5, 6 \tag{3.21}$$

The $A\Phi_A(x, y, z)$ terms are independent of the body motion and are subject to the boundary condition,

$$\frac{\partial \Phi_A}{\partial n} = 0 \quad \text{on} \quad S_b \tag{3.22}$$

The velocity potential Φ_A can be expressed as the combination of the incoming wave potential corresponding to the Froude-Krylov force and the disturbance to the incoming wave potential by the diffracted velocity potential, corresponding to the diffraction force. The Φ_A can therefore be written as,

$$\Phi_A = \phi_0 + \phi_7 \tag{3.23}$$

where the ϕ_0 corresponds to the incoming wave potential (calculated using Equation 3.16) and the ϕ_7 to the diffracted wave potential which is subject to the boundary condition,

$$\frac{\partial \phi_7}{\partial n} = -\frac{\partial \phi_0}{\partial n} \quad \text{on} \quad S_b \tag{3.24}$$

Equations 3.21,3.23, and 3.24 represent the body boundary conditions.

3.2.1.2 Fluid Domain Boundary Conditions

All potential terms ϕ_j where $j = 0, 1, 2, ..., 7$ in the Equation 3.20 should satisfy the Laplace equation for the entire fluid domain such that,

$$\nabla^2 = 0, \quad j = 0, 1, 2, ..., 7 \tag{3.25}$$

All potential terms should also satisfy the sea-bed boundary condition that the $\frac{\partial \phi_j}{\partial z} = 0$ at $z = -h$ for $j = 0, 1, 2, ..., 7$ (Equation 3.6), and the free-surface boundary condition,

$$-\frac{\omega^2}{g}\phi_j + \frac{\partial \phi_j}{\partial t}, \quad j = 0, 1, 2, ..., 7 \tag{3.26}$$

3.2.1.3 Radiation Boundary Condition

Finally, imposing the radiation boundary condition to ensure that the incoming wave potential acts on the body and all other wave potentials - diffraction and radiation potentials, emanate out from the body, such that,

$$\phi_j \propto e^{\pm ikx}, \quad j = 0 \quad \text{and, } \phi_j \propto e^{\mp ikx}, \quad j = 1, 2, ..., 7 \quad \text{as, } x \to \pm\infty \tag{3.27}$$

Where ϕ_0 is used to calculate the Froude-Krylov force directed towards the body, while the radiation and diffraction potentials emanate away from the body.

3.2.2 Hydrodynamic Forces and Moments

The wave relation for wave potentials and the appropriate boundary conditions can be used for the expressions for hydrodynamic forces and moments. Substituting Equation 3.20 in Bernoulli's equation while retaining only the I order linearized terms, the expression for pressure exerted on the body can be written as,

$$P_{hd} = -\rho\Re\left(\left(\Sigma_{j=1}^{6}\eta_j\phi_j(x,y,z) + A\Phi_A(x,y,z)\right)e^{i\omega t}\right) - \rho g z \tag{3.28}$$

The expression for forces and moments on the body can be expressed by integrating the fluid pressure over the immersed wetted body surface, S_b, such that,

$$\begin{pmatrix} F_{hd} \\ M_{hd} \end{pmatrix} = \underbrace{-\rho g \iint_{S_b} \begin{pmatrix} \vec{n} \\ \vec{r}\times\vec{n} \end{pmatrix} z \; dS}_{F_K} \underbrace{-\rho\Re\left(\Sigma_{j=1}^{6} i\omega\eta_j e^{i\omega t} \iint_{S_b} \begin{pmatrix} \vec{n} \\ \vec{r}\times\vec{n} \end{pmatrix} \phi_j \; dS\right)}_{F_R}$$
$$\underbrace{-\rho\Re\left(i\omega A e^{i\omega t} \iint_{S_b} \begin{pmatrix} \vec{n} \\ \vec{r}\times\vec{n} \end{pmatrix} (\phi_0+\phi_7) dS\right)}_{F_{exc}=F_{FK}+F_{Diff}} \tag{3.29}$$

Equation 3.29 ascribe the forces and moments on a floating body to:

1. Hydrostatic Force, F_K: The force due to the pressure that was being applied, on the bulk of the displaced fluid, before the body was introduced,

2. Radiation Force, F_R: The reaction force to the wave field radiated by the body due to its motion. The radiation force is a combination of evanescent local effects manifested as the so-called added mass and the propagating effects represented as the radiation damping,

3. Excitation Force, F_{exc}: The combination of the Froude-Krylov force, F_{FK}, exerted by the incoming wave; and the diffraction force, F_{Diff}, which is the disturbance to the F_{FK} due to the diffraction or the scattering by the floating body.

3.3 Development of Time-Domain Models

Time-domain modeling of the hydrodynamics of WECs is fundamental to the modeling, control design, and eventual deployment of WECs. The relations for the radiation and excitation forces in the previous Section are frequency dependent. Time-domain modeling requires the use of Fourier transforms to generate an Impulse Response Function (IRF) for the radiation and excitation forces, which can then be convoluted

with the body velocity and wave elevation, respectively.

The Equation 3.29 describes the hydrostatic and hydrodynamic forces for a single body. While describing the necessary equations for time-domain modeling, this Section develops the equations of motion for an array of WECs in the time-domain. Also, the boundary conditions and assumptions discussed in the previous Section are still imposed.

The equations of motion shown here can be used for both hydrodynamically coupled and uncoupled arrays. A WEC array is hydrodynamically coupled when a WEC is affected by the motion of other WECs in the array. An array can be considered hydrodynamically uncoupled when its members are far enough apart to have minimal mode-couplings, i,e. the motion of any WEC in the array is independent of the motion of any other WEC.

The motion of WECs is commonly described using the Cummins' equation that uses the equation shown in (3.30) [66, 85]. The viscous drag forces can be ignored for large marine structures, as they are small compared to radiation damping [66].

$$(\mathbf{M} + \mathbf{a}_\infty)\vec{\ddot{q}}(t) + \int_0^t \mathbf{h_r}(t-\tau)\vec{\dot{q}}(\tau)d\tau + \mathbf{K}\vec{q}(t) = \vec{Q}(t) \tag{3.30}$$

Where the $\vec{q}(t)$ are generalized motion coordinates, and the coefficient of $\vec{\ddot{q}}(t)$ is the

summation of the inertia of the system and the asymptotic added mass. That is, for an n degree-of-freedom system, $\mathbf{M} \in \mathbb{R}^{nxn}$ is the inertia matrix, and $\mathbf{a}_\infty \in \mathbb{R}^{nxn}$ is the added mass matrix at infinite frequency. The second term is the convolution operation needed to calculate the radiation force, $\vec{F}_R(t)$. Also, $\mathbf{K} \in \mathbb{R}^{nxn}$ is the hydrostatic and gravitational stiffness matrix are multiplied with the body displacement to calculate the hydrostatic force, $\vec{F}_K(t)$, and the $\vec{Q}(t)$ contains the Froude-Krylov, diffraction, PTO, and friction generalized forces. For a rigid body moving in 6 DOF (degrees of freedom), the $\vec{q}(t)$ are surge, sway, heave, roll, pitch, and yaw modes, and the matrices $\mathbf{M}, \mathbf{a}_\infty, \mathbf{h_r}(t)$, and $\mathbf{K}$ are 6×6 matrices.

For multiple bodies forming an array of N rigid bodies, each moving in 6 DOF, these matrices become $6N \times 6N$ matrices, and the off-diagonal terms contain the appropriate coupling terms. Superposition of hydrodynamic coefficients forces and moments may suggest mutual exclusivity; however, they are related. For instance, the radiation force and the excitation force are related using the Haskind relations and Green's theorem while the added-mass and radiation damping are related by the Kramers-Kronig relation, an alternative form of Bode's gain and phase relationship [7, 25].

The linear assumptions entail that the incoming waves have small amplitude and steepness and that the body motions are also small. Note, in this Section, the excitation force coefficients and the radiation function are represented as $H_{exc}(j\omega)$ and

$H_r(j\omega)$ to emphasize that they are complex functions. The excitation force is the input to the system, as shown in (3.31). The excitation force Impulse Response Function (IRF) is expressed as (3.32). Therefore, the convolution in (3.31) models the excitation force acting on the system for a known wave elevation time-history η as shown in (3.33). The excitation force can be calculated in advance without affecting the real-time dynamic model because the excitation force depends on the incoming wave profile. However, for irregular wave inputs, with wave profiles changing in real-time, prediction of the incoming wave profile becomes critical.

$$\vec{F}_{exc}(t) = \int_{-\infty}^{\infty} \Big[h_{exc}(\tau)\eta(t-\tau) \Big] d\tau \tag{3.31}$$

where,

$$h_{exc}(t) = \frac{1}{2\pi} \int_{-\infty}^{\infty} \Big[H_{exc}(j\omega) e^{j\omega t} \Big] d\omega \tag{3.32}$$

and,

$$\eta(t) = \frac{1}{2\pi} \int_{-\infty}^{\infty} \Big[\eta(j\omega) e^{j\omega t} \Big] d\omega \tag{3.33}$$

The second term in (3.30), together with the $\mathbf{a}_\infty \ddot{\vec{q}}(t)$ term, corresponds to the radiation force. This term is the convolution of the radiation force IRF with the body's velocity. This follows from defining the radiation FRF $H_r(j\omega)$, using the hydrodynamic radiation effects of the body, i.e., added mass $\mathbf{a}(\omega)$ and radiation damping $\mathbf{b}(\omega)$, which are obtained using numerical solvers like WAMIT. The radiation FRF

can therefore be expressed as,

$$H_r(j\omega) = [j\omega\tilde{\mathbf{a}}(\omega) + \mathbf{b}(\omega)], \tag{3.34}$$

where $\tilde{\mathbf{a}}(\omega) = \mathbf{a}(\omega) - \mathbf{a}_\infty(\omega)$, such that the asymptotic added mass that converges to a constant $\mathbf{a}_\infty$ at higher frequencies is subtracted from the radiation function $H_r(j\omega)$, and added to the inertia matrix $\mathbf{M}$ as shown in (3.30). The inverse Fourier transform of $H_r(j\omega)$ in (3.34) results in the radiation IRF, as shown in (3.35)

$$h_r(t) = \frac{1}{2\pi}\int_{-\infty}^{\infty}\Big[H_r(j\omega)e^{j\omega t}\Big]d\omega \tag{3.35}$$

which becomes,

$$h_r(t) = \frac{1}{2\pi}\int_{-\infty}^{\infty}\Big[[i\omega\tilde{\mathbf{a}}(\omega) + \mathbf{b}(\omega)](\cos(\omega t) + j\sin(\omega t))\Big]d\omega \tag{3.36}$$

Note, the radiation function, $H_r(j\omega)$ itself is a complex function; however, the corresponding IRF is a real function. This is physically justified by associating the added mass, which is an evanescent local effect represented as the imaginary-part of the complex radiation function, and the radiation damping part, which propagates with the real-part, such that the radiation force, $\vec{F_r}(t)$, is a real causal force experienced in the vicinity. This can be shown mathematically by observing that sine is an odd function, while cosine is an even function, and that both the $\tilde{\mathbf{a}}(\omega)$ and $\mathbf{b}(\omega)$ are even

functions [66]. Therefore the imaginary part of (3.36) is, an odd function and thus vanishes, while the real part being an even function is twice its value when the lower limit is *zero* and the upper limit is ∞. Changing the lower limit of (3.36) to *zero* and doubling the real part,

$$h_r(t) = \frac{1}{2\pi} \int_{-\infty}^{\infty} \Big[\mathbf{b}(\omega) \cos(\omega t) - \omega \tilde{\mathbf{a}}(\omega) \sin(\omega t) \Big] d\omega \tag{3.37}$$

The Kramers-Kronig relations relate the added mass $\mathbf{a}(\omega)$ and radiation damping $\mathbf{b}(\omega)$. The Ogilvie equations use the Kramers-Kronig relations to simplify (3.37) such that $h_r(t)$ can be expressed as either a cosine transform of the radiation damping FRF $\mathbf{b}(\omega)$ or the sine transform of the FRF of the added mass $\mathbf{a}(\omega)$ [86].

$$\begin{aligned} h_r(t) &= \frac{2}{\pi} \int_{0}^{\infty} \Big[\mathbf{b}(\omega) \cos(\omega t) \Big] d\omega \\ &= -\frac{2}{\pi} \int_{0}^{\infty} \Big[\omega \tilde{\mathbf{a}}(\omega) \sin(\omega t) \Big] d\omega \end{aligned} \tag{3.38}$$

Therefore, the radiation IRF is real-valued and causal. Motion-dynamics modeling of a marine structure will require the convolution of (3.38) with the body velocity to calculate the radiation force in real-time. Physically, this means the body will only experience the radiation force after a wave has hit it, and the body generates a radiation field around it that, in turn, becomes the radiation force experienced by

the body. The expression for the radiation force in the time-domain can therefore be expressed as,

$$\vec{F}_R(t) = \mathbf{a}_\infty \ddot{\vec{q}}(t) + \int_0^t \left[h_r(t-\tau) \dot{\vec{q}}(\tau) \right] d\tau \tag{3.39}$$

such that, $h_r(\tau) = 0$, for $\tau < 0$. When numerically integrating (3.39), the limits of the integral can go from the $max(0, t - t_d)$ to t, where t_d is the duration of the radiation IRF (i.e., the radiation IRF is zero for $t > t_d$).

Chapter 4

Effects of Hydrodynamic Coupling on Energy Extraction Performance of Wave Energy Converter Arrays

The incident ocean waves get reflected, absorbed or diffracted by a WEC, therefore in an array of such devices, the reflection and diffraction results in a diffracted wave field [103]. Diffraction effects, such as Bragg scattering, can be observed in a WEC array if the buoy dimensions are much smaller than the incident wavelength[47]. Therefore, WEC array design, that maximizes energy extraction, should be influenced by an understanding of the radiation and diffraction phenomena. This Chapter is adapted from Husain and Parker [56]. The work in this Chapter was conceptualized by Parker

and the theoretical development and simulations were done by Husain.

The wave potential equations shown in Chapter 3, show the equations for the wave potentials when no floating bodies exist, which is then super-imposed by the wave potentials generated due to introduction of floating bodies. The discussion in Chapter 3 is extended here for a compact WEC array. The underlying assumption being that the incoming wave field gets reflected-by and transmitted-through the WEC array. The reflected wave field superimposes with the incoming wave-field, the transmitted wave field is the wave field in the wake of of the WEC array, while the the difference between the transmitted and reflected wave fields is the theoretical limit of the energy available to the WEC array.

A compact array model, parameterized with a non-dimensional WEC packing ratio, was proposed by Garnaud and Mei[45]. Garnaud and Mei showed that a WEC array offers the potential for higher energy extraction than a single, large WEC[46]. This chapter extends those results to include the hydrodynamic coupling between individual WECs in the array showing an increase in the theoretical energy extraction. This chapter considers a 25-WEC, compact array example to:

1. Demonstrate the trapping-effect that occurs due to the hydrodynamic coupling within a WEC array,

2. Demonstrate the potential advantages of WEC arrays over isloated WECs,

3. Develop a framework for evaluation of theoretical limit of the energy extraction efficiency for a given WEC array, based on its packing density.

The hydrodynamic coefficients were generated using WAMIT (Wave Analysis MIT) and were incorporated into the dynamic equations introduced by Garnaud and Mei. An energy extraction efficiency metric, considering the energy dissipated due to the waves reflected by and transmitted through the array, was used to quantify the effect of the added terms. This is important for wave energy conversion as it corresponds to waves with higher speeds and wavelengths.

4.1 Model Description

Figure 4.1 illustrates the array layout and parametric dimensions. The incoming waves are assumed to be parallel to the positive x direction and two dimensional, i.e. the wave profile is same across the y direction. As shown in Figure 4.1, a^* is the buoy radius, H^* is the buoy draft and d^* is the center to center distance between two adjacent buoys. The normalized array width is denoted by L and the water depth by h^*. The water depth is much larger than the buoys draft. The incident wave region, with no buoys is named Region I, the array region with buoys is named Region II and the region beyond the WEC array along x direction is named Region III.

The area fraction of the array or the packing ratio f for the compact array is defined as [46],

$$f = \frac{\pi a^{*2}}{d^{*2}} \quad \text{Therefore,} \quad d^* = \sqrt{\frac{\pi a^{*2}}{f}} \tag{4.1}$$

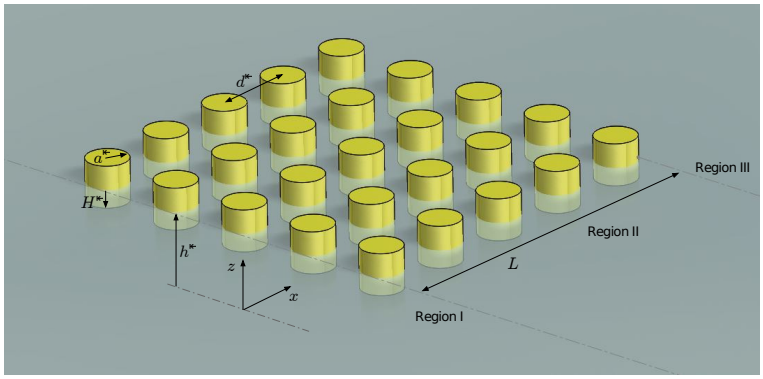

Figure 4.1: WEC array layout. The Figure was adapted from Husain and Parker [56].

4.2 Multi-scaled dynamics relations

A WEC buoy can be modeled as a spring-damper system, with frequency dependent added mass and radiation damping contributions due to hydrodynamics[66]. Garnuad and Mei ignore the resonance and hydrodynamic effects, citing the small size of the buoys [46]. The development here introduces the hydrodynamic effects to the equations of motion. Starting analysis with the single buoy dynamics equation of motion [46].

$$
\begin{aligned}
M^* \frac{\partial^2 \zeta^*}{\partial t^{*2}} + \lambda_d^* \frac{\partial \zeta^*}{\partial t^*} + \pi a^{*2} \rho g \zeta^* &= -\iint_{S_b} \rho \frac{\partial \phi^*}{\partial t^*} dS \\
M^* = \rho \pi a^{*2} H^*; \zeta^* = A^* \zeta; t^* = t' \sqrt{\frac{h^*}{g}}; \Phi^* &= A^* \sqrt{g h^*} \Phi;
\end{aligned}
\tag{4.2}
$$

where M^* is buoy mass and ζ^* is its heave displacement. The linear load force proportionality constant, λ_d^* is the damping of the power take off (PTO) . The water density, gravitational acceleration and velocity potential are denoted by ρ, g and ϕ respectively. The excitation force is in the Haskind form, where the bottom surface of the cylindrical buoy is defined as the physical domain S_b over which the surface integral is evaluated [85]. The superscript asterisk denotes the buoy's physical variables and prime denotes normalized variables.

We now extend Eq. 4.2 to incorporate hydrodynamic effects of frequency dependent added mass, m_a, and radiation damping, B_ω^*. The nondimensional added mass m_a', buoy mass M, radiation damping B_ω and the PTO's linear load force damping constant λ_d are given in Eq. 4.3.

$$
\begin{aligned}
\mu m_a' &= \frac{m_a}{\pi a^{*3}\rho} \\
M &= \frac{a^* H^*}{h^* a^*}; \text{defining}, \quad H' = \frac{H^*}{a^*}; \text{hence}, \quad M = \mu H' \\
B_\omega &= \frac{B_\omega^*}{\pi a^{*2}\rho g}\sqrt{\frac{g}{h^*}} \\
\lambda_d &= \frac{\lambda_d^*}{\pi a^{*2}\rho g}\sqrt{\frac{g}{h^*}}
\end{aligned}
\tag{4.3}
$$

The superscript prime denotes normalized single buoy variables. The ratio μ relates the buoy microscale to the array macroscale, such that $\mu \equiv \frac{a^*}{h^*}$. The WAMIT generated hydrodynamic coefficients, the added mass and the radiation damping values, are normalized and added to the normalized buoy mass $\mu H'$ and the normalized PTO damping λ_d respectively. Substituting Eq. 4.3 into Eq. 4.2 gives

$$
\left(\mu(H' + m_a')\right)\frac{\partial^2 \zeta}{\partial t'^2} + (\lambda_d + B_\omega)\frac{\partial \zeta}{\partial t'} + \zeta = -\frac{1}{\pi}\iint_{S_b}\frac{\partial \phi}{\partial t'}dS' \tag{4.4}
$$

At this point, the analysis of a single buoy can be extended to the macroscale motion of the aggregate compact array. This is described in detail by Garnaud and Mei using the method of multiple scales where the macroscale solution arises from the 0^{th} order term in the potential function expansion. The multiscale expansions introduced by Garnaud and Mei are shown in Eq. 4.5.

$$\begin{aligned}
\phi &= e^{-i\omega t'}[\phi_0(\vec{x'},\vec{x}) + \mu\phi_1(\vec{x'},\vec{x}) + \mu^2\phi_2(\vec{x'},\vec{x}) + ...] \\
\eta &= e^{-i\omega t'}[\eta_0(\vec{x'},\vec{x}) + \mu\eta_1(\vec{x'},\vec{x}) + \mu^2\eta_2(\vec{x'},\vec{x}) + ...] \\
\zeta &= e^{-i\omega t'}[\zeta_0(\vec{x'},\vec{x}) + \mu\zeta_1(\vec{x'},\vec{x}) + \mu^2\zeta_2(\vec{x'},\vec{x}) + ...]
\end{aligned} \tag{4.5}$$

The multiscale equation of motion can then be written by substituting Eq. 4.5 into Eq. 4.4

$$\begin{aligned}
(-\mu(H' + m_a')\omega^2 - i(\lambda_d + B_\omega)\omega + 1)[\zeta_0 + \mu\zeta_1 + \mu^2\zeta_2 + ...] \\
= \frac{i\omega}{\pi}\iint_{S_b}[\phi_0 + \mu\phi_1 + \mu^2\phi_2 + ...]dS'
\end{aligned} \tag{4.6}$$

Considering the ζ_0 and ϕ_0 terms in Eq. 4.6, the ratio of forcing function and heave displacement can then be written as,

$$\frac{1}{(-\mu(H' + m_a')\omega^2 - i(\lambda_d + B_\omega)\omega + 1)} = \frac{1}{\zeta_0}\frac{i\omega}{\pi}\iint_{S_b}\phi_0 dS' \tag{4.7}$$

The quantity on the left side in Eq. 4.7, can be simplified by using a Laurent series expansion of the terms such that,

$$\frac{1}{1 - i(\lambda_d + B_\omega)\omega - \mu(H' + m'_a))\omega^2} = \sum_{j=0} \mu^j F_j(\omega) \tag{4.8}$$

where the left side is expanded in a Laurent series, shown in Eq. 4.9, where $x = 1 - i(\lambda_d + B_\omega)\omega$ and $y = \mu(H' + m'_a))\omega^2$. The first two terms of the expansion of $F_j(\omega)$ are shown in Eq. 4.10.

$$\frac{1}{x - y} = \frac{1}{x} + \frac{y}{x^2} + \frac{y^2}{x^3} + \frac{y^3}{x^4} + \frac{y^4}{x^5} + O\bigg(1/x)^6\bigg) \tag{4.9}$$

$$\begin{aligned} F_0(\omega) &= \frac{1}{1 - i(\lambda_d + B_\omega)\omega} \\ F_1(\omega) &= \frac{(H' + m'_a)\omega^2}{(1 - i(\lambda_d + B_\omega)\omega)^2} \end{aligned} \tag{4.10}$$

The analysis below uses only the $F_0(\omega)$ term where the radiation damping, B_ω, is apparent. The $F_1(\omega)$ term illustrates the role of added mass if additional terms are used.

4.3 Eigenfunction Analysis by Region

4.3.1 Region I

The velocity potential in Region I can be expressed in terms of horizontal and vertical eigenfunctions [46]. The subscripts I and 0 for ϕ denote the velocity potential in Region I for the 0^{th} term of the multiscale velocity potential expansion shown in Eq. 4.5. The lower case ψ and f_n denote horizontal and vertical eigenfunctions in Region I respectively. Note, the vertical eigenfunction f_n should not be confused with packing ratio f, which does not have a subscript.

$$\phi_{I,0}(\vec{x}) = \sum_{n=0}^{\infty} \psi_n(x,y) f_n(z) \tag{4.11}$$

where,

$$f_0(z) = c_0 \cosh(k_0(z+1)) \quad \text{and} \quad f_n(z) = c_n \cos(\kappa_n(z+1)) \tag{4.12}$$

are vertical eigenfunctions for normalized depth in z direction i.e. $-1 < z < 0$, and $(k_0, k_1, ...)$ are the eigenvalues of the wave dispersion equation, with the choice of

$$c_0 = \sqrt{\frac{2}{1+\omega^{-2}\sinh^2 k_0}} \quad \text{and} \quad c_n = \sqrt{\frac{2}{1+\omega^{-2}\sinh^2 k_n}} \tag{4.13}$$

The wave dispersion equation is stated as,

$$\omega^2 = k_n \tanh(k_n), \quad n = 0, 1, 2, ... \tag{4.14}$$

The above equations are solved using interior point optimization for k_n eigenvalues at each frequency steps such that, k_0 is the positive real root and $k_n \equiv i\kappa_n, n = 1, 2, ...$ is the n^{th} imaginary root, i.e.

$$\omega^2 = k_0 \tanh(k_0), \quad \omega^2 = -\kappa_n \tanh(\kappa_n), n = 1, 2, 3... \tag{4.15}$$

These k_n eigenvalues are then used to solve for $f_n(z)$ eigenfunctions as a function of water depth z. The absolute value of the real and imaginary parts of the eigenvalues increases with increase in wavenumber for the first eigenvalue but largely remains constant for other imaginary eigenvalues which are pertinent to evanescent modes.

4.3.2 Region II

Garnaud and Mei propose that the compact WEC array region can be seen to have a modified velocity potential and wave dispersion equation. The $F_n(z)$ eigenfunctions in the Region II are a function of depth and are affected by packing ratio and the first order Laurent series term $F_0(\omega)$. A packing ratio of $f = 0.2$ was used for the numerical solutions of these equations.

The velocity potential in Region II , $\phi_{II,0}$, can be expressed in terms of horizontal $\Psi_n(x, y)$ and vertical $F_n(z)$ eigenfunctions [46].The upper case Ψ and F_n denote horizontal and vertical eigenfunctions in Region II respectively.

$$\phi_{II,0}(x) = \sum_{n=0}^{\infty} \Psi_n(x, y) F_n(z) \tag{4.16}$$

$F_n(z)$ are vertical eigenfunctions for normalized depth in z direction i.e. $-1 < z < 0$, and $(K_0, K_1, ...)$ are the eigenvalues of the modified dispersion relation

$$F_n(z) = C_n \cos(K_n(z + 1)) \tag{4.17}$$

with the choice of

$$C_n = \sqrt{\frac{2}{1 + \sigma^{-2} \sinh^2 K_n}} \tag{4.18}$$

defining σ^2 such that,

$$\sigma^2 \equiv \omega^2 [f F_0(\omega) + (1 - f)] \tag{4.19}$$

The dispersion relation in Region II is modified by considering the packing ratio f and the Laurent series term $F_0(\omega)$ that includes the hydrodynamic effects of the normalized radiation damping. The modified dispersion equation is given by Eq. 4.20

$$\sigma^2 = K_n \tanh(K_n), n = 0, 1, ... \tag{4.20}$$

Note, σ^2 is complex and therefore eigenfunctions $F_n(z)$ are complex.

The above equations are solved using interior point optimization for K_n eigenvalues at each frequency step, such that K_n eigenvalues for $n = 0$ are almost real and K_n eigenvalues for $n = 1, 2, ...$ are almost imaginary for all frequency steps. These K_n eigenvalues are then used to solve for $F_n(z)$ eigenfunctions as a function of water depth z. The absolute value of the real and imaginary parts of the eigenvalues increases

with increase in wavenumber for the first almost real eigenvalue but largely remains constant for other almost imaginary eigenvalue which are pertinent to evanescent modes.

4.3.3 Region III

Region III has a free surface similar to Region I. Therefore, the eigenvalues and eigenfunctions calculated for Region I are used for Region III.

4.4 Energy extraction efficiency for a linear WEC array

Garnuad and Mei consider a long array of normalized width L, with its edges parallel to the crests of incoming plane waves. The energy extraction efficiency of the array is calculated by subtracting the energy lost due to energy reflected back by the array in Region I and the energy transmitted to Region III.

The velocity potential equations can be expressed in terms of reflection coefficients R_n in Region I, Buoy propagation coefficients B_n and B'_n in Region II and transmission coefficients T_n in Region III. The equations for horizontal velocities and the

inner products of horizontal velocity and the corresponding region's velocity potential eigenfunctions are then used for the expressions for the aforementioned coefficients. The coefficients will then be substituted in the velocity potential equations in the three regions. Pressure continuity boundary condition will then be used to formulate a system of equations that will be solved for horizontal velocities at array boundaries.

The energy lost due to reflections and transmissions can be scrutinized by calculating the horizontal velocities at the interfaces of the array with Region I and Region III respectively.

4.5 Energy Reflection and Transmission Coefficients for Velocity Potentials

4.5.1 Velocity potentials

The velocity potential equation in Region I will have contributions from the incident wave and the reflections from the array. The potential equation in Region I is expressed in terms of $f_n(z)$ eigenfunctions of the velocity potential in Region I and

reflection coefficients denoted by R_n, such that,

$$\phi_{0,I}(x,z) = \frac{-i}{\omega f_0(0)}\left(e^{ik_0 x} f_0(z) + \sum_{n=0}^{\infty} R_n e^{-ik_n x} f_n(z)\right), \quad -\infty < x < 0, \tag{4.21}$$

In Region II, Garnaud and Mei express the velocity potential using buoy propagation coefficients, denoted by B_n and B'_n. Modifying the potential equation to include the Region II $F_n(z)$ eigenfunctions which imbibe the hydrodynamic considerations shown earlier.

$$\phi_{0,II}(x,z) = \frac{-i}{\omega f_0(0)} \sum_{n=0}^{\infty} (B_n e^{iK_n x} + B'_n e^{-iK_n x}) F_n(z), \quad 0 < x < L, \tag{4.22}$$

In Region III, the velocity potential equation will have contributions from only the energy that is transmitted through the array. The potential equation in Region III is written in terms of $f_n(z)$ eigenfunctions of the velocity and transmission coefficients denoted by T_n such that,

$$\phi_{0,III}(x,z) = \frac{-i}{\omega f_0(0)} \sum_{n=0}^{\infty} T_n e^{ik_n x} f_n(z), \quad L < x < \infty, \tag{4.23}$$

4.5.2 Horizontal Velocities at Interfaces

Using the velocity potentials, we can write the velocities at the junction of Region I and Region II as $U_I(z)$ and the velocity at the junction of Region II and Region III as $U_{II}(z)$. These are the horizontal velocities at $x = 0$ and $x = L$, respectively.

$$U_I(z) = \frac{\partial \phi_{0,I}}{\partial x}(0, z) \quad U_{II}(z) = \frac{\partial \phi_0}{\partial x}(L, z) \tag{4.24}$$

4.5.2.1 Horizontal velocity in region I

Now writing the horizontal velocity in Region I at $x = 0$, using the velocity potential equation in Region I.

$$U_I(z) = \frac{\partial \phi_{0,I}}{\partial x}(0, z) = \frac{1}{\omega f_0(0)} \left(k_0 f_0(z) + \sum_{n=0}^{\infty} R_n(-k_n) f_n(z) \right) \tag{4.25}$$

Using the inner product definition $\langle f_n | f_m \rangle = \int_{-1}^{0} f_n(z) f_m(z) dz$ and also, using the orthogonality property

such that $\langle f_n | f_m \rangle = 1$, if $n = m$ and $\langle f_n | f_m \rangle = 0$, if $n \neq m$, we have,

$$\langle U_I | f_0 \rangle = \frac{k_0}{\omega f_0(0)} \left[1 - R_0 \right] \tag{4.26}$$

4.5.2.2 Horizontal velocity in Region II

Similarly, in Region II the relation for velocity potential in Region II, $\phi_{0,II}$, can be used to get expressions for the horizontal velocities in buoy region.

$$\frac{\partial \phi_{0,II}}{\partial x}(x,z) = \frac{-i}{\omega f_0(0)} \sum_{n=0}^{\infty} (B_n e^{iK_n x} - B'_n e^{-iK_n x}) iK_n F_n(z) \tag{4.27}$$

Now writing the horizontal velocity in Region II at $x = 0$

$$U_I(z) = \frac{\partial \phi_{0,II}}{\partial x}(0,z) = \frac{-i}{\omega f_0(0)} \sum_{n=0}^{\infty} (B_n - B'_n) iK_n F_n(z) \tag{4.28}$$

and at $x = L$

$$U_{II}(z) = \frac{\partial \phi_{0,II}}{\partial x}(L,z) = \frac{-i}{\omega f_0(0)} \sum_{n=0}^{\infty} (B_n e^{iK_n L} - B'_n e^{-iK_n L}) iK_n F_n(z) \tag{4.29}$$

Now using the orthogonal property and taking the inner product with F_n at $x = 0$

$$\langle U_I | F_n \rangle = \frac{-i}{\omega f_0(0)} \sum_{n=0}^{\infty} (B_n - B'_n) iK_n \tag{4.30}$$

Similarly, using the orthogonal property and taking the inner product with F_n at $x = L$

$$\langle U_{II} | F_n \rangle = \frac{-i}{\omega f_0(0)} \sum_{n=0}^{\infty} (B_n e^{iK_n L} - B'_n e^{-iK_n L}) iK_n \tag{4.31}$$

4.5.2.3 Horizontal velocity in Region III

Now writing the horizontal velocity in Region III at $x = L$

$$U_{II}(z) = \frac{\partial \phi_{0,III}}{\partial x}(L,z) = \frac{-i}{\omega f_0(0)} \sum_{n=0}^{\infty} (T_n e^{ik_n L}) ik_n f_n(z) \tag{4.32}$$

Taking inner product with f_n at $x = 0$ will lead to

$$\langle U_{II}|f_n\rangle = \frac{-i}{\omega f_0(0)} \sum_{n=0}^{\infty} (T_n e^{ik_n L}) ik_n \tag{4.33}$$

4.5.3 ReflectionR_0, R_n, Buoy Propagation B_n, B'_n and Transmission CoefficientsT_n

The expressions for horizontal velocities at interfaces and their inner products with the corresponding region's vertical eigenfunctions can be simplified to get the following equations.

$$\begin{aligned} R_0 &= \left[1 - \omega f_0(0) \frac{\langle U_I|f_0\rangle}{k_0} \right] \\ R_n &= \omega f_0(0) \left[- \frac{\langle U_I|f_n\rangle}{k_n} \right] \end{aligned} \tag{4.34}$$

$$\begin{aligned} B_n &= -i\omega f_0(0) \frac{\langle U_{II} - e^{-iK_n L} U_I|F_n\rangle}{2K_n \sin K_n L} \\ B'_n &= -i\omega f_0(0) \frac{\langle U_{II} - e^{iK_n L} U_I|F_n\rangle}{2K_n \sin K_n L} \end{aligned} \tag{4.35}$$

$$T_n = \omega f_0(0) \frac{\langle U_{II}|f_n\rangle}{e^{ik_n L} k_n} \tag{4.36}$$

4.6 Velocity Potentials using Horizontal Velocities at Interfaces and Eigenfunctions

The coefficients shown in Eq.s 4.34, 4.35 and 4.36 can now be used to restate the velocity potential equations.

4.6.1 Region I

4.6.1.1 $\phi_{0,I}(0,z)$

Now, writing the potential equation at $x = 0$ by substituting Eq. 4.34 in Eq. 4.21, we get,

$$\phi_{0,I}(0,z) = \frac{-i}{\omega f_0(0)}\left(f_0(z) + \left(1 - i\omega f_0(0)\frac{\langle U_I|f_0\rangle}{ik_0}\right)f_0(z) - i\omega f_0(0)\sum_{n\geq 1}\left(\frac{\langle U_I|f_n\rangle}{ik_n}\right)f_n(z)\right) \tag{4.37}$$

$$\phi_{0,I}(0,z) = \left(\frac{-i}{\omega f_0(0)} 2f_0(z) + \left(-\frac{\langle U|f_0\rangle}{ik_0}\right) f_0(z) - \sum_{n\geq 1}^{\infty}\left(\frac{\langle U_I|f_n\rangle}{ik_n}\right) f_n(z)\right) \tag{4.38}$$

4.6.2 Region II

4.6.2.1 $\phi_{0,II}(0,z)$

Now, writing potentials at $x = 0$ by substituting Eq. 4.35 in Eq. 4.22, we get,

$$\phi_{0,II}(0,z) = \frac{-i}{\omega f_0(0)} \sum_{n=0}^{\infty}\left(-i\omega f_0(0)\frac{\langle U_{II} - e^{-iK_nL}U|F_n\rangle}{2K_n \sin K_nL} - i\omega f_0(0)\frac{\langle U_{II} - e^{iK_nL}U|F_n\rangle}{2K_n \sin K_nL}\right) F_n(z) \tag{4.39}$$

$$\phi_{0,II}(0,z) = -\sum_{n=0}^{\infty}\left(\frac{\langle U_{II} - \cos(K_nL)U_I|F_n\rangle}{K_n \sin K_nL}\right) F_n(z) \tag{4.40}$$

4.6.2.2 $\phi_{0,II}(L,z)$

Now, writing $\phi_{0,II}(L,z)$ at $x=L$ by substituting Eq. 4.35 in Eq. 4.22, we get, In Region II.

$$\begin{aligned}&\phi_{II}(L,z)\\&= \frac{-i}{\omega f_0(0)}\sum_{n=0}^{\infty}\Big(- i\omega f_0(0)\frac{\langle U_{II} - e^{-iK_nL}U_I|F_n\rangle}{2K_n\sin K_nL}e^{iK_nL}\\&- i\omega f_0(0)\frac{\langle U_{II} - e^{iK_nL}U_I|F_n\rangle}{2K_n\sin K_nL}e^{-iK_nL}\Big)F_n(z)\end{aligned} \tag{4.41}$$

Therefore,

$$\Phi_{II}(L,z) = -\sum_{n=0}^{\infty}(\frac{\langle U_{II}\cos K_nL - U_I|F_n\rangle}{K_n\sin K_nL})F_n(z) \tag{4.42}$$

4.6.3 Region III

4.6.3.1 $\phi_{III}(L,z)$

Writing potential at $x=L$ by substituting Eq. 4.36 in Eq. 4.23

$$\Phi_{III}(L,z) = \frac{-i}{\omega f_0(0)}\sum_{n=0}^{\infty} i\omega f_0(0)\frac{\langle U_{II}|f_n\rangle}{e^{ik_nL}ik_n}e^{ik_nL}f_n(z) \tag{4.43}$$

Therefore,

$$\Phi_{III}(L,z) = \sum_{n=0}^{\infty} \frac{\langle U_{II}|f_n\rangle}{ik_n} f_n(z) \tag{4.44}$$

4.7 Pressure continuity at the interfaces

We would now apply the pressure continuity condition at the array boundaries at $x = 0$ and $x = L$ and equate the velocity potentials at array boundaries. Following which, the orthonormal conditions are used to arrive at a system of equations which can be solved for horizontal velocities U_I and U_{II} respectively.

4.7.1 Expressing $\phi_I(0,z) = \phi_{II}(0,z)$ and $\phi_{II}(L,z) = \phi_{III}(L,z)$

$$\begin{aligned} &\frac{-i}{\omega f_0(0)} 2f_0(z) - \sum_{n\geq 0}^{\infty} \left(\frac{\langle U_I|f_n\rangle}{ik_n} f_n(z) \right) \\ &= -\sum_{n=0}^{\infty} \frac{\langle U_{II} - \cos(K_n L) U_I|F_n\rangle}{K_n \sin K_n L} F_n(z) \end{aligned} \tag{4.45}$$

$$-\sum_{n\geq 0}^{\infty} \left(\frac{\langle U_{II}\cos K_n L - U_I|F_n\rangle}{K_n \sin K_n L}\right) F_n(z) = \sum_{n\geq 0}^{\infty} \frac{\langle U_{II}|f_n\rangle}{ik_n} f_n(z) \tag{4.46}$$

4.7.2 Orthonormal expansions

Using the inner product property of orthonormal expansions we can simplify the inner products. We define M_{12} as the inner product of two eigenfunctions, f_1 and f_2. Therefore, $\langle F_q|f_n\rangle = M_{qn}$,

$$M_{qn} = \langle F_q|f_n\rangle = \int_{-1}^{0} F_q(z)f_n(z)dz \tag{4.47}$$

$$M_{qn} = \omega^2 f(1-F_0)\Big(\frac{c_n cosh(k_n)C_m cosh(K_q)}{K_q^2 - k_n^2}\Big) \tag{4.48}$$

Therefore we can express,

$$\begin{aligned} \langle U_I|f_n\rangle = \langle\sum_{q,n}(U_{I,q})F_q|f_n\rangle = \sum_{q,n} M_{qn}U_{I,q} \quad Also, \\ \langle U_{II}|f_n\rangle = \langle\sum_{q,n}(U_{II,q})F_q|f_n\rangle = \sum_{q,n} M_{qn}U_{II,q} \end{aligned} \tag{4.49}$$

4.7.3 System of equations for numerical solution

Note the system of equations here, ought to be solved numerically at each frequency step.

$$\frac{-i}{\omega f_0(0)} 2 f_0(z) - \sum_{q,n} \left(\frac{M_{qn} U_{I,q}}{i k_n} \right) f_n(z) = \sum_{n \geq 0} \left(- \frac{U_{II,n}}{K_n \sin K_n L} + \frac{U_{I,n}}{K_n \tan K_n L} \right) F_n(z) \tag{4.50}$$

$$\sum_{q,n} \left(\frac{M_{qn} U_{II,q}}{i k_n} \right) f_n(z) = \sum_{n \geq 0} \left(- \frac{U_{II,n}}{K_n \tan K_n L} + \frac{U_{I,n}}{K_n \sin K_n L} \right) F_n(z) \tag{4.51}$$

Now taking the scalar product with F_p for $p = 0, 1, 2, 3...$ we can further simplify to

$$\frac{-i}{\omega f_0(0)} 2 M_{0p} - \sum_{q,n} \left(\frac{M_{qn} U_{I,q}}{i k_n} \right) M_{np} = \left(- \frac{U_{II,p}}{K_p \sin K_p L} + \frac{U_{I,p}}{K_p \tan K_p L} \right) \tag{4.52}$$

$$\sum_{q,n}\left(\frac{M_{qn}U_{II,q}}{ik_n}\right)M_{np}=\left(-\frac{U_{II,p}}{K_p\tan K_pL}+\frac{U_{I,p}}{K_p\sin K_pL}\right) \tag{4.53}$$

We numerically solved the above system of equations for horizontal velocities corresponding to the compact array boundaries with incident region and transmission region.

4.8 Reflection Coefficient R_0, Transmission Coefficient T_0 and dimensionless Power-extraction Efficiency E

The horizontal velocities at the compact array boundaries with incident region and transmission region from Section IX can be used such that the transmission coefficient can be restated as

$$T_0=i\omega f_0(0)\frac{\langle U_{II}|f_n\rangle}{e^{ik_nL}ik_n} \tag{4.54}$$

And the Reflection coefficient can be restated as

$$R_0 = 1 - i\omega f_0 \frac{\langle U_I | f_0 \rangle}{ik_0} \tag{4.55}$$

Therefore, for calculating transmission and reflection ratios as performance criteria in terms of extraction rate, adding the contributions from all frequency steps and velocity steps. The transmission and reflection coefficients are then calculated at each depth.

$$T_0(z) = \sum_{q,k} i\omega(k) f_0(k) \frac{M_{q0}(0,q,k) U_{II,q}(q,k)}{e^{ik_0(k)L} ik_0(k)} \tag{4.56}$$

$$R_0(z) = 1 - \sum_{q,k} i\omega(k) f_0(k) \frac{M_{q0}(0,q,k) U_I((q,k))}{ik_0(k)} \tag{4.57}$$

Where, q indices correspond to frequency steps and k indices are the corresponding wavenumber steps. Using the above discussion we can now express the dimensionless power-extraction efficiency as

$$E = 1 - |T|^2 - |R|^2 \tag{4.58}$$

4.9 Hydrodynamics of the Compact Array

The compact 25-buoy array in Figure 4.2 was modeled in WAMIT to get its hydrodynamic coefficients. The buoy radius a^* was set at 1 m and the draft H^* was set at 1 m, with a packing ratio f = 0.2. Therefore, the inter-buoy distance d^* was set at 3.9633 m. The water depth was 100 m. The buoys were indexed as illustrated in Figure 4.2.

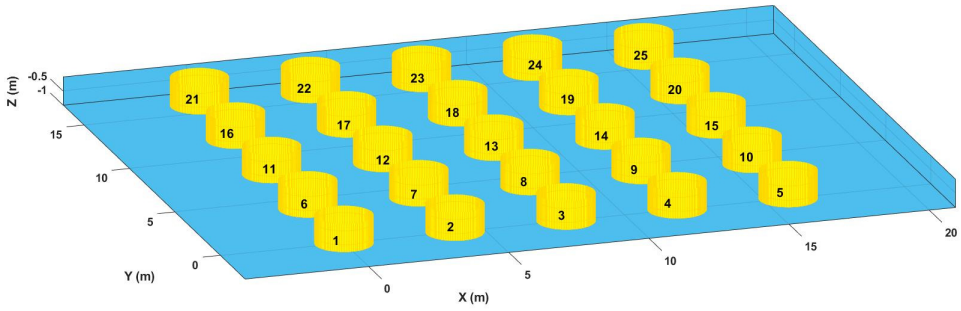

Figure 4.2: WEC array layout used for WAMIT analysis; A packing ratio of 0.2 was used to determine the mutual distances between the buoys. The incoming waves are in positive x direction and are uniform across y direction [56]

4.10 Results

The effect of hydrodynamic coupling on energy extraction is illustrated using the 25 WEC array shown in Figure 4.2. The WECs with greater hydrodynamic coupling

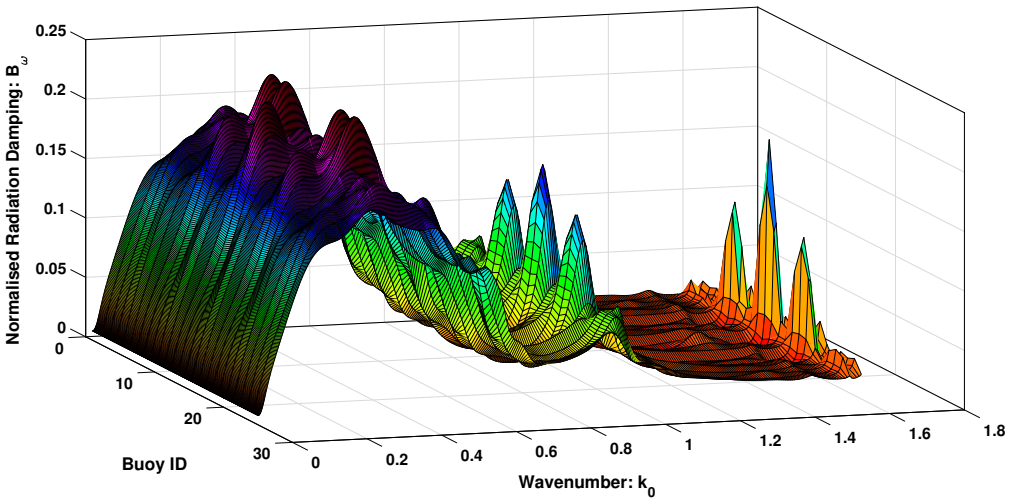

Figure 4.3: normalized radiation damping from WAMIT as a function of wavenumber and buoy ID. The buoys in the crowded parts of the array show additional peaks at higher wave-numbers due to hydrodynamic coupling [56]

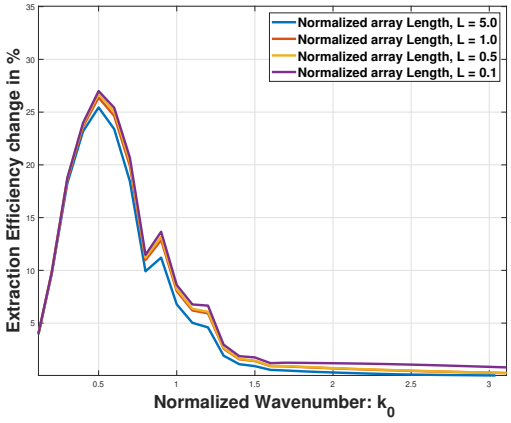

Figure 4.4: Percentage change in extraction efficiency after considering hydrodynamic radiation effects as a function of wavenumber. The change in extraction efficiency is shown for different normalized array lengths (L) [56]

have a higher radiation damping. The array layout and spacing considered here is similar to WECWAKES project [120]. The WAMIT generated radiation effects are shown in Figure 4.3 as a function of normalized wavenumber for each buoy. Each buoy is assigned a Buoy ID, corresponding to the indices shown in Figure 4.2. This

surface plot is the normalized damping plots of the buoys in the array stacked along Buoy ID axis.

The additional lobes for the nine buoys in the interior area of the array can be seen in Figure 4.3. This behavior is expected in coupled multi-body vibrating systems. It can be seen that the additional lobes are particularly high for Buoy ID 12, 13 and 14, and especially for Buoy ID 13. While a single isolated WEC buoy will have a single peak in hydrodynamic coefficients plots, hydrodynamic couplings in an array have additional lobes depending on the individual buoy's location in the array.

WAMIT analysis revealed that the WEC buoys with higher hydrodynamic coupling interactions in the interior of the array, had higher hydrodynamic radiation coefficients over a wider frequency range. This suggests that larger arrays have higher extraction efficiency over a wider frequency range as compared to smaller arrays.

The hydrodynamic reflection and transmission effects are calculated using the eigenvalue analysis of the system, parameterized by both packing density and wave speed as described in the previous sections. The energy extraction efficiencies are calculated by considering the energy dissipated due to the waves reflected by and transmitted through the array.

Figure 4.4 shows the difference between theoretical energy extraction with and without consideration of hydrodynamic coupling between the WECs. Consideration of

hydrodynamic coupling shows that up to 28% more energy can be extracted. The effect of WEC location in the array can be observed in the extraction efficiency plots, where peaks in the normalized radiation damping plot, Figure 4.3, are seen in the energy extraction efficiency plot of Figure 4.4. This shows that the array geometry is important for even small compact arrays.

4.11 Summary

This chapter compared the effect of incorporating hydrodynamic couplings to a compact array. It was found that the hydrodynamic coupling of the compact array devices enhances the energy extraction potential. This is because of higher hydrodynamic interactions manifested by higher radiation damping over a wider frequency range.

WAMIT modeling further illuminate the significance of such hydrodynamic interactions. Devices that had more neighbors, such that they were positioned more internally in the array, correspondingly showed higher energy extraction efficiency. This enhances the energy available for extraction because the device radiation damping increases for a wider frequency range due to increased device interactions in a compact array. Additionally, hydrodynamic couplings in a compact array increases retention of wave energy, such that less energy is transmitted through the array or bounced off as reflected energy. The work discussed in Chapter 4, can be experimentally tested

and verified by comparing the water elevations at different points within and around the array. The experimental testing can be done based on the physical modeling done as part of the WECWAKES project that modeled a 25 buoy WEC array [120].

Chapter 5

Radiation Force Modeling for a Wave Energy Converter Array

A WEC array requires real-time control whose design should exploit its model. The motivation and focus of this chapter are to generate passive transfer function arrays that model the radiation forces for an array of WECs. Time-domain motion dynamics for floating bodies are commonly described using Cummins' equation of motion for floating bodies. A wide range of control design methods requires a state-space or transfer function model instead of the time-domain model with convolution. The control design for WEC arrays, whether for analysis or implementation, is challenging because the Cummins' equation requires a convolution operation that calculates the radiation forces due to fluid-memory effects of the radiation field in real-time. Over

the years, researchers have presented Linear Time-Invariant (LTI) models that circumvent the convolution operation. The estimation method can be initialized using the radiation frequency response function (FRF) or the radiation impulse response function (IRF), followed by optimization using the radiation FRF. When the initial reference function was the IRF, the IRF was numerically integrated using Euler's method and Filon's quadrature formula to calculate the Fourier transforms needed to generate the IRFs. Overall, the direct estimation using radiation FRF as the initial reference was most accurate. After introducing a passivity-based approach to estimate radiation force transfer functions, the algorithm was extended to a WEC array. The effect of hydrodynamic coupling is investigated by comparing a sparsely spaced array and a compact array. The algorithm can be used for non-homogeneous WEC arrays that may not have the same geometry. The transfer function array models developed here are an important step towards designing motion control strategies that can respond to changing ocean conditions in real-time.

The rest of the chapter is organized as follows. The Section 3.3describes the pertinent equations of motion and develops a time-domain model for a WEC. The Section 5.1introduces the need for passivity in estimated LTI systems and outlines the physical properties of the radiation FRF that the LTI system is supposed to emulate. The Section 5.2 outlines the algorithm for the proposed approach. The algorithm's efficacy is demonstrated using a single-cylinder at two different scales in Section5.3.

The estimated system's accuracy is quantified in terms of its frequency response function (FRF) and passivity using the Input Passivity Index (ν). Section 5.5 describes the motion simulation using the estimated transfer functions and compares its performance to direct convolution. Following this, Section 5.6analyzes the results and discusses the observations. Finally, Section 5.7summarizes this chapter.

5.1 Passivity properties of the radiation FRF, $H_r(\omega)$, radiation IRF, $h_r(t)$, and estimated LTI system, $G(s)$

The properties of radiation effects are encapsulated in the radiation FRF $H_r(\omega)$; therefore, the estimated LTI system, $G(s)$, should preserve the physical phenomenon being approximated. The boundary conditions of the radiation FRF $H_r(\omega)$, and its time-domain counterpart radiation IRF, $h_r(t)$, are summarized in Table 5.1. Table 5.1 is similar to the properties discussed by Duarte et al., and Perez and Fossen [26, 93].

In Table 5.1, properties $1, 2$, and 3 are a consequence of the Riemann-Lebesgue Lemma, while the BIBO stability condition in property 4 establishes the input-output stability of the convolution for radiation forces [93, 115].

Property	**Implications**
1. $lim_{\omega \to 0} H_r(\omega) = 0$	There are zeros at $s = 0$
2. $lim_{\omega \to \infty} H_r(\omega) = 0$	Strictly proper
3. $lim_{t \to 0^+} h_r(t) \neq 0$	Relative degree 1
4. $lim_{t \to \infty} h_r(t) = 0$	Bounded Input Bounded Output (BIBO) stability
5. The mapping, $\dot{x} \to \vec{F}_R(t)$ is passive	$H_r(\omega)$, therefore $G(s)$ is Positive Real (PR)

Table 5.1
Properties of the radiation FRF $H_r(\omega)$, radiation IRF, $h_r(t)$, and estimated LTI system, $G(s)$, see [26, 93].

Property 5 in Table 5.1 entails the dissipativity property of the radiation FRF $H_r(\omega)$ since it starts as 0 and then converges to 0 since the radiation forces are dissipative. The Ogilvie equations indicate that the radiation IRF, $h_r(t)$, can be calculated using the radiation damping coefficients, $\mathbf{b}(\omega)$ [86]. The radiation damping coefficients, $\mathbf{b}(\omega)$, also starts from 0 and converges to 0 since the hydrodynamic theory dictates that the radiation damping coefficients, $\mathbf{b}(\omega) > 0, \forall \omega$. It can be therefore said; the radiation forces are passive since radiation forces are dissipative and they generate no energy. For linear systems, the passivity property is equivalent to positive realness [63, 115].

The estimated transfer functions are used to calculate the radiation force and are used in the negative feedback of the complete dynamic system. A challenging property of linear systems is that even if a system such as a transfer function is stable on its own when used in the closed-loop of the complete system, it can result in making the

overall system unstable. Therefore, system stability can be assessed by looking into its passivity property. Passivity implies that the physical system does not generate energy and can only store or dissipate energy. Therefore, the estimated transfer function array should be passive, i.e., positive real. This stability criterion has been recognized by various researchers, such as in [15, 26, 69, 91, 115]. The passivity condition essentially requires that the estimated LTI system, $G(s)$, or the radiation force transfer function array, populated by transfer functions between body velocity and radiation force, $\vec{F}_R(t)$, is positive semi-definite, which implies that the real part of the transfer function array is positive. Formally, the passivity condition for a transfer function array, which is a Multiple Input Multiple Output (MIMO) system, can be stated as discussed by Khalil [63]. Let G(s) be a $p \times p$ proper rational transfer function matrix, and suppose $det[G(s) + G(-s)^T]$ is not identically zero. Then G(s) is strictly positive real if and only if

1. G(s) is Hurwitz; that is, poles of G(s) have negative real parts

2. $G(s) + G(-s)^T$ is positive definite for all $\omega \in R$

3. Either $G(\infty) + G(\infty)^T$ is positive definite; or it is positive semi definite and $lim_{\omega \to \infty} \omega^2 M^T [G(j\omega) + G(-j\omega)^T] M$ is positive definite for any $p \times (p - q)$ full rank matrix M, such that $M^T [G(\infty) + G(\infty)^T] M = 0$, where, $q = rank[G(\infty) + G(\infty)^T]$. Additionally, if $G(\infty) + G(\infty)^T = 0$, then $M = I$, which is the case for radiation damping.

As discussed by Kottenstette et al., a system with a positive input passivity index ν implies positive-realness and hence passivity for an LTI system [68] also, as stated by Khalil, two passive systems where one system is in the negative feedback loop of the former system results in an overall passive system [63]. Also, if one of them is input passive and the other is strictly passive, the overall system is passive [63, 68]. Additionally, the lack of passivity of one can be made up by a higher passivity index of the other [63, 111]. Interestingly, if the viscous drag force (proportional to the velocity squared) is not ignored, the input passivity index of the plant will increase. This makes the plant $P(s)$ just barely passive, based on the input passivity index. Therefore, the radiation force transfer function must have a safe margin for the input passivity index to ensure the stability of the overall system by making up for the slim passivity index margin in the $P(s)$.

This chapter assesses the passivity using the input passivity index, ν, such that $\nu = \frac{1}{2} min_{\omega} \lambda_{min}(G(j\omega) + G^T(-j\omega))$, where λ_{min} are the minimum eigenvalues of $(G(j\omega) + G^T(-j\omega))$. For SISO LTI systems, the input passivity index corresponds to the horizontal distance of the Nyquist plot from the imaginary axis, or in other words, the real part of the Nyquist plot, since for a SISO LTI system, $(G(j\omega) + G^T(-j\omega))$ results in $2Re(G(j\omega))$, making $\nu = Re(G(j\omega))$. Note, for a scalar transfer function passivity corresponds to the Nyquist criterion for feedback systems, requiring the phase of the LTI system in question being within $[-\pi/2, +\pi/2]\ rad$.

Classical control methods such as the Nyquist plot can be used to assess the robustness of stability and passivity. However, assessing stability through a passivity-index based approach, as proposed here, has certain advantages, including,

1. Satisfying robust stability criteria such as $\mathcal{L}_2$ stability, and more generally, dissipativity,

2. Using passivity ensures mapping the estimated LTI system to the physical properties of the system being modeled,

3. Passivity-based stability analysis can be used for a MIMO system, such as Multiple Degree of Freedom (MDOF) analysis of a single body or multiple body arrays.

Note, the evaluation of stability is based on a real quantity - the input passivity-index. Interestingly, the analytic property of the radiation FRF is preserved when using the passivity-index based system estimation because the estimation method matches both the magnitude and phase of the radiation FRF. The estimated system does eventually converge because a passive system is also dissipative, thereby preserving the analytic property of the radiation FRF [67, 68].

There is, however, a trade-off between the stability of the estimated models and their fidelity to the physical system. While estimating, it must be kept in mind that, in

general, increasing the order of the estimated model may result in a better fit but sacrifice passivity (and thus, stability) and also risk overfitting.

Overfitting results in the estimated system having high-frequency poles (typically higher than 10 rad/s) that do not correspond to the actual physical system because marine systems are relatively very slow (typically operate within 0 to 4 rad/s). On the contrary, reducing the order of the estimated system will enhance passivity but sacrifice accuracy to the physical system being estimated.

It is proposed that the passivity property can be checked for, and the orders of the estimated transfer functions can be chosen through iterations, as discussed in [91, 115]. Many researchers, therefore, start with the smallest order possible, and then increase order while checking for model accuracy and passivity [91, 115].

The current state-of-the-art methods, therefore, check for passivity but do not enforce or guarantee the passivity in the estimated transfer functions [30, 31, 91, 115].

5.2 The Algorithm

The radiation force estimation strategy in three stages,

1. Generation of a reference for the radiation transfer function,

2. Iteration to obtain a low-order, accurate, and passive transfer function,

3. Final tuning to ensure minimum phase, such that at least one zero of the estimated radiation transfer function is at the origin (i.e., $s = 0$ is a zero).

From now on, the frequency domain approach will refer to the estimation using the radiation FRF, $H_r(\omega)$, while the time-domain approach will refer to the estimation using radiation IRF, $h_r(t)$. In Figure 5.1, the light blue line shows the frequency domain approach, which is also referred to as the direct estimation method in the literature [26]. The red downwards arrow on the top right of the Figure 5.1 shows the additional step of generating the radiation IRF, $h_r(t)$, for the time-domain approach. This is followed by an iterative estimation routine to satisfy the stability and accuracy conditions. Finally, an optimization routine ensures that the estimated transfer function is minimum phase.

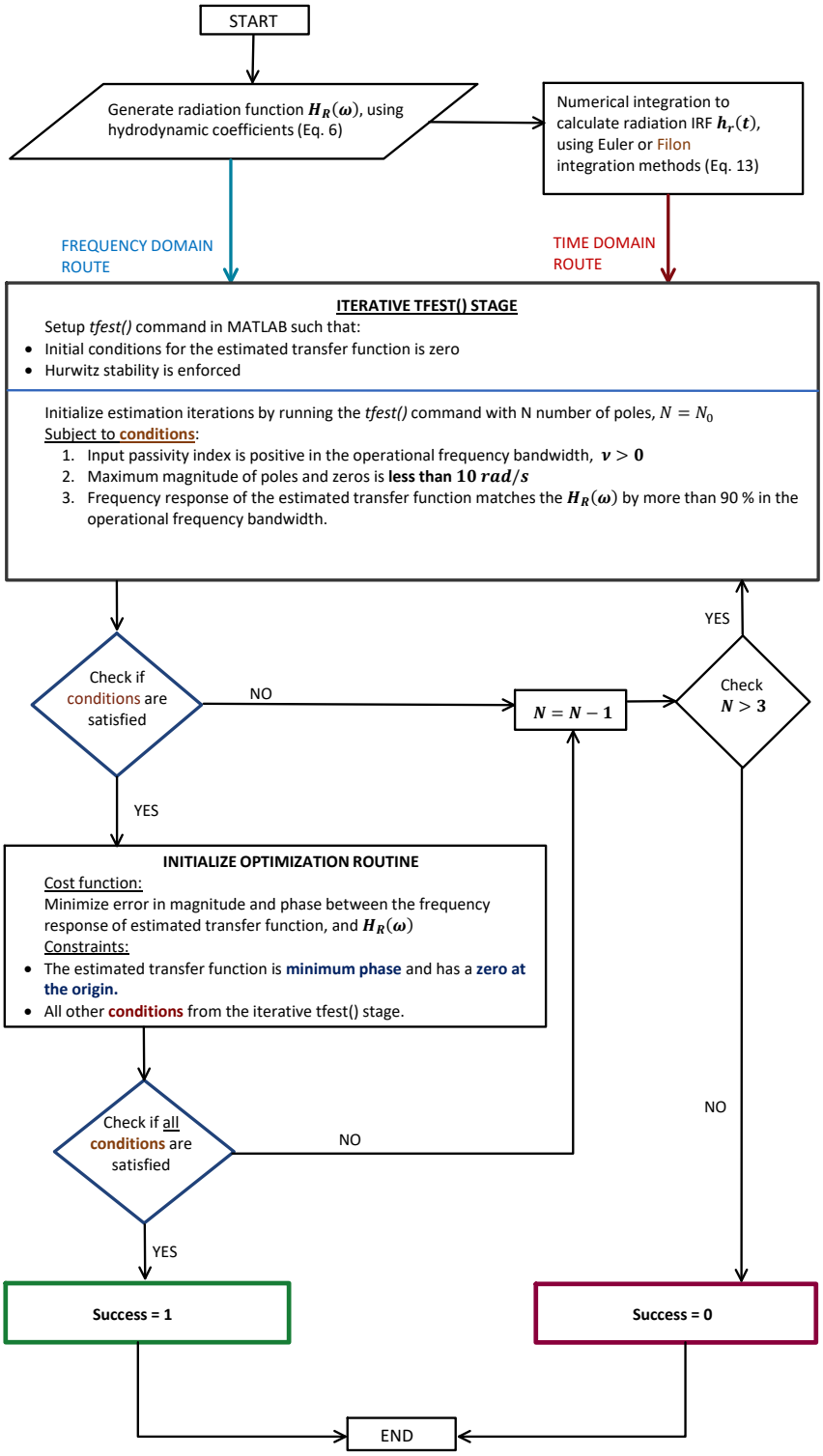

Figure 5.1: Algorithm for the estimation of radiation transfer function array $G(s)$.

5.2.1 Generation of a reference for the radiation transfer function

5.2.1.1 Frequency domain approach

For the frequency domain approach, the radiation FRF $H_r(j\omega)$ is generated using WAMIT as shown in Eq. 3.34. This function is then used as the reference function for the iterative estimation of radiation transfer functions. Since the radiation FRF is dissipative, it asymptotically approaches *zero*. In the discussion that follows the frequency at which the radiation FRF is less than 5% of its maxima ($f_0\ rad/s$ is greater than the frequency at the maxima) will be referred to as $f_0\ rad/s$.

5.2.1.2 Time-domain approach

The time-domain approach uses the radiation IRF, $h_r(t)$, as the reference for estimating the radiation transfer function. The radiation IRF is calculated by the numerical integration of the Ogilvie equation, which entails calculating the cosine transform of radiation damping coefficients as discussed in [86], such that,

$$h_r(t) = \frac{2}{\pi}\int_0^{\Omega} \mathbf{b}(\omega)\cos(\omega t)d\omega \tag{5.1}$$

Where Ω is the cut-off frequency at which the frequency domain radiation damping data is truncated. The radiation IRFs can be calculated using just the radiation damping function, $\mathbf{b}(\omega)$, as shown in Eq. 3.38 and 5.1. Note that alternatively, the radiation IRF, $h_r(t)$, can also be written in terms of the added mass, $\mathbf{a}(\omega)$. However, the radiation damping $\mathbf{b}(\omega)$ starts from zero and converges to zero asymptotically, while the added mass $\mathbf{a}(\omega)$ has a positive value at infinity, i.e., $\mathbf{a}_\infty > 0$. The added mass at infinity, $\mathbf{a}_\infty$, can therefore be a source of numerical errors from BEM solvers such as NEMOH or WAMIT [60, 133]. Additionally, as noted by Kriastansen et al., the radiation IRF, $h_r(t)$, converges faster when the radiation damping form of Eq. 3.38 is used [69].

The radiation IRF, $h_r(t)$, has a *cosine* function in its kernel and therefore is an oscillating function. The radiation FRF, $H_r(\omega)$, and hence the radiation IRF, $h_r(t)$, is often referred to as the *memory* effect function. Strictly speaking, the IRF still has energy after $t > \pi/\Delta\omega \ s$, where $\Delta\omega$ is the frequency step, thereby making the Discrete Fourier Transform of the $\mathbf{b}(\omega)$ *not an exact* quantity. This can be understood from hydrodynamics theory, such that, although the radiation effects are causal, they have effervescent local effects, manifested as added mass, and propagating effects, manifested as radiation damping that linger much later than the initial impulse, resulting in the *memory* effect [66]. As stated in Table 5.1, the radiation IRF, $h_r(t)$, converges to 0, but it does so much later than the initial impulse, owing to the *memory* effects. For accurate system identification, especially for MIMO systems,

the hydrodynamic coefficients must be generated at a fine resolution. So for the frequency resolution used in a subsequent example ($0.005\ rad/s$), the $\pi/\Delta\omega$ term would be 629 s. Even for a coarser frequency resolution of $0.02\ rad/s$ the $\pi/\Delta\omega$ is 157 s. Therefore, the calculation of the cosine transform in practice would require truncation. Note that although the radiation FRFs of auto-coupled modes (diagonal terms) do start from 0 and converge to 0, within relatively low-frequency bandwidths, the radiation FRFs of cross-coupled modes (off-diagonal terms) are highly oscillatory and do not converge to 0 until much higher frequencies than the auto-coupled modes. This makes the choice of an accurate numerical integration method critical. Note, that the time-domain modeling should be capable of adapting to novel WEC designs which may use other modes such as pitch or surge, or a combination of mode-couplings.

For the time-domain routes, two numerical integration methods were compared, namely, Euler integration and Filon's quadrature formula for trigonometric integrals, which can be seen as a special case of Adaptive Recursive Simpson's rule [39]. Note the *fft()* (Fast Fourier Transform) or the *dct()* (discrete cosine transform) commands in MATLAB can be used to generate the IRFs. However, this chapter investigated the effects of the numerical integration method (to generate the reference IRF), on the accuracy of the estimated LTI system. As mentioned earlier, the WAMIT manual recognizes the higher accuracy of Filon's integration method in Chapter 13 that describes the $f2t$ utility [133]. In an effort to have greater control over the sources of inaccuracies, Filon integration was implemented using custom code. Filon's method

is computationally less expensive than Simpson's rule, as best explained by L.N.G Filon's remarks that Simpson's rule requires finer step-sizes than his method [39]. Filon's method is capable of handling highly oscillating functions and, therefore, can capture the memory effects in the radiation IRF, $h_r(t)$, with much more accuracy.

The characteristic root error in the numerical integration methods needed to compute the radiation IRF, $h_r(t)$, indicates the accuracy of the numerical integration. The characteristic root error for Euler integration is proportional to the step size h [9]. For Filon's method, Barakat et al. show that the error in the numerical integration primarily depends on the rapidly oscillating part of the integrand [6]. Barakat et al. and Håvie observed the challenges regarding the expression for error in Filon's method while stating the error is proportional to the second derivative of the function [58]. Dominguez et al.discuss the stability and error for similar oscillatory integrals [24]. Dominguez et al. proved that the error in Filon's method for this context is an exponentially decaying function of step-size h and the number of discrete points N used in the numerical integration [24]. Therefore, Filon's method is stable and much more accurate than Euler's method when calculating the reference function for the transfer function estimation. This chapter calculates the radiation IRF, $h_r(t)$, using both Euler integration and Filon integration methods, and then compares the corresponding estimated transfer functions.

5.2.2 Iterative estimation of radiation transfer functions

This stage corresponds to the iterative loop initialized with N_0 poles in Figure 5.1. The estimation process is done using the *tfest()* command in MATLAB. The function uses iterative optimization to curve fit either impulse response data or frequency response data. The function has options that let the user enforce Hurwitz stability. This is done by reflecting poles estimated in the right-hand plane about the imaginary axis and starting the estimating optimization again. The estimated transfer function is then further refined using non-linear search optimization to get the best possible fit. The *tfest()* command by default estimates a $strictly-proper$ transfer function. The estimation process is carried out for each mode combination, resulting in a transfer function array, $G(s)$. For MDOF systems such as WEC arrays, mode-couplings include both intra-body and inter-body interactions, while for single body MDOF systems, mode-couplings include implying intra-body mode couplings. When estimating transfer function matrices, $G(s)$, the input passivity index (ν) characteristics correspond to the positive-definiteness of the transfer function matrix. The matrix of magnitudes of each individual transfer function in $G(s)$ can be seen as a Toeplitz matrix. It was observed that the ν of the entire transfer function matrix could be enhanced if the ν of the Toeplitz matrices making up the transfer function array increased [80]. Therefore, iterating on the order of the individual transfer functions in $G(s)$ to achieve more positive ν for each transfer function helps in estimating more

positive ν for the transfer function array $G(s)$.

The iterative estimation process using the *tfest()* command is initiated with the highest expected order, N_0. At each iteration, the *tfest()* command estimates a transfer function array $G(s)$. This $G(s)$ should then satisfy the following criteria,

1. $G(s)$ is bandwidth-limited passive, such that the input passivity index is positive ($\nu > 0$) for a defined frequency bandwidth,

2. $G(s)$ has accurate frequency response, such that the percentage fit between the frequency response of $G(s)$ and the radiation FRF $H_r(j\omega)$ is greater than 90% for a defined frequency bandwidth,

3. Finally, $G(s)$ should not have poles frequencies higher than $2f_0$ rad/s in the Laplace domain. This is necessary to avoid overfitting and avoiding poles that do not correspond to the physical phenomenon $G(s)$ is supposed to replicate. This upper bound was empirically set to about two times the frequency at which the radiation FRF converges to 0.

If the estimation process fails to find a $G(s)$ that satisfies these three criteria, the algorithm reiterates by reducing the expected order by one. This iterative process is deemed to fail if the estimated order has to be reduced below the third order. Note, that regardless of the initial reference function being the radiation IRF, $h_r(t)$, or the radiation FRF $H_r(j\omega)$, the iterative process compares the frequency response of $G(s)$

with the radiation FRF $H_r(j\omega)$, ensuring accuracy with the hydrodynamics radiation damping data.

5.2.3 Final optimization routine

The estimated $G(s)$ from the previous step serves as a very good initial guess for the final optimization. The estimated $G(s)$ from the iterative *tfest()* routine has very high accuracy and positive input passivity index ν. However, the $G(s)$ estimated from the iterative routine in the previous step often generates transfer functions that do not have a zero at the origin. The $G(s)$ is then subjected to optimization to enhance accuracy and passivity index characteristics while ensuring that the properties listed in Table 5.1 are exhibited by the estimated transfer function array $G(s)$.

The final optimization is set up so that the cost function is a weighted function formed by the sum of the absolute squared difference between the frequency response magnitude and phase of the transfer function array $G(s)$ and the radiation FRF $H_r(j\omega)$, such that,

$$J = \alpha \sum \left(|H_r(j\omega)| - |G(j\omega)| \right)^2 + \beta \sum \left(\angle(H_r(j\omega)) - \angle(G(j\omega)) \right)^2 + \gamma \left(\nu_{G(j\omega)} . \nu_{G(j\omega)}^T \right)^2 \tag{5.2}$$

where J is the cost function to be minimized by optimization, α is the weight for the magnitude difference, β is the weight for the phase difference, and γ is the weight for the input passivity index ν. The weights of the cost function are so chosen that both phase and magnitude of the optimized $G(s)$ are more accurately matched with the radiation FRF $H_r(j\omega)$ and a positive passivity index within the operational frequency bandwidth. Additionally, the frequency range over which the optimization is performed can also be chosen such that the accuracy and passivity characteristics are further improved.

The optimization is further subject to constraints such that the estimated $G(s)$ satisfies the properties laid out in Table 5.1 and meets the following criteria,

1. $G(s)$ must be minimum-phase and have a zero at the origin,
2. $G(s)$ must be strictly proper, i.e., has a relative degree of 1,
3. The input passivity index is positive, such that $\nu > 0$, for a defined frequency bandwidth,
4. All poles are less than $2f_0\ rad/s$,
5. The accuracy of the optimized $G(s)$ exceeds 90% for a defined frequency bandwidth.

Figure 5.2 shows the effect of optimization on the estimated $G(s)$ for the case of a

single heaving cylinder with a radius of 1 m and draft 1m. It can be observed that the optimized $G(s)$ has resolved the non-minimum phase issue in the $G(s)$ before optimization. The zero at the origin constraint helped in significantly enhancing the accuracy of the optimized $G(s)$ with respect to $H_r(j\omega)$ at low frequencies. The optimized $G(s)$ satisfied the properties listed in Table 5.1 for the frequency bandwidth in which hydrodynamic data was available.

The final optimization ensured that the $G(s)$ had a minimum phase. This also helped increase the input passivity index ν. As shown in Figure 5.1, should the optimization fail in satisfying all aforementioned conditions, further iteration is done by reducing the initial estimation order. Further refinement is subject to the empirical inverse relationship between the accuracy and the stability such that an increase in the accuracy typically decreases the passivity index and vice versa.

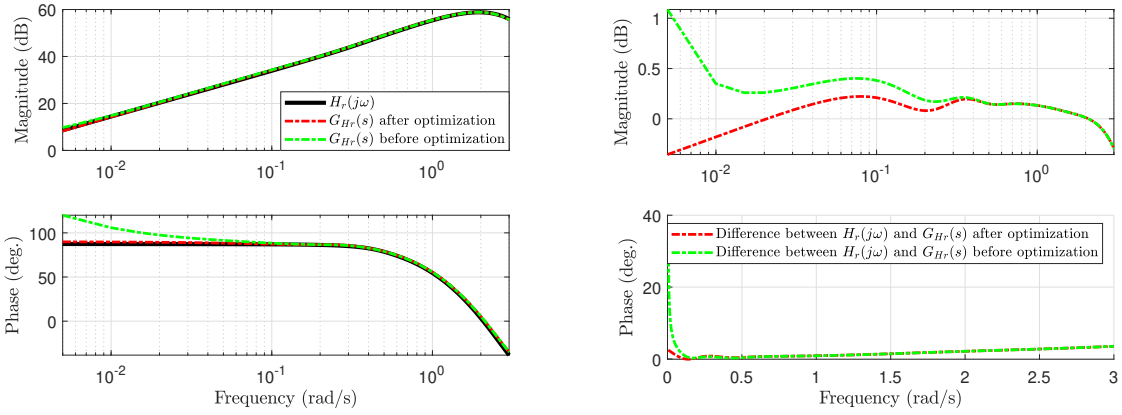

Figure 5.2: Comparison of the estimated $G(s)$ before and after the final optimization for the case of a single heaving cylinder with a radius of 1 m and draft 1m.

5.2.4 Scaling Scheme

Scalability of the estimated transfer functions is desirable for consistency in modeling the WECs at prototype-scale and deployment-scale. The algorithm can be scaled up or down by first normalizing the estimated transfer function using wave frequency, water density and the characteristic length, and then performing Froude scaling using the characteristic length for wave frequency and the pertinent hydrodynamics coefficients. The normalizing scheme for the added mass, radiation damping and the wave frequency can be expressed as [133],

$$\bar{\mathbf{a}}_{i,j}(\omega) = \frac{\mathbf{a}_{i,j}(\omega)}{\rho g L^k}; \quad \bar{\mathbf{b}}_{i,j}(\omega) = \frac{\mathbf{b}_{i,j}(\omega)}{\rho g \omega L^k};$$

where,

$$\begin{aligned} &k = 3 \quad \text{for} \quad (i, j = 1, 2, 3) \\ &k = 4 \quad \text{for} \quad (i = 1, 2, 3, \quad j = 4, 5, 6) \quad \text{or} \quad (i = 1, 2, 3, \quad j = 4, 5, 6) \\ &k = 5 \quad \text{for} \quad (i, j = 4, 5, 6) \end{aligned} \tag{5.3}$$

Since the radiation FRF as shown in Equation 3.34, the radiation FRF is expressed as, $H_r(j\omega) = [j\omega\tilde{\mathbf{a}}(\omega) + \mathbf{b}(\omega)]$, dividing the radiation FRF by $\rho g L^k$ will result in an expression in terms of the normalized hydrodynamic coefficients shown in Equation 5.3. This normalization scheme can be used to scale the radiation transfer functions. If the characteristic length of a given radiation force transfer function is, $L = L_0$, then

a radiation force transfer function function for a system that is scaled by a factor of $L = L_1$ can be scaled using the scaling factors necessary for scaling the corresponding radiation FRFs. Consider a system with a characteristic length $L = L_0$ and radiation FRF $H_{r0}(\omega)$, and an another system with characteristic length $L = L_1$ and radiation FRF $H_{r1}(\omega)$; then these radiation FRFs can be related using the ratio of the two characteristic lengths $L_{sc} = \frac{L_1}{L_0}$, such that,

$$H_{r1}(j\omega) = H_{r0}(j\omega)L_{sc}^{k}, \quad \text{whose frequency would scale as,} \quad \omega_1 = \omega_0 L_{sc}^{-\frac{1}{2}} \tag{5.4}$$

where the subscript *0* corresponds to the radiation FRF being scaled, the subscript *1* to the scaled up or down radiation FRF, while all other physical parameters will be scaled using Froude scaling respectively. Therefore, the estimated transfer functions can be scaled using a factor of L_{sc}^{k} such that,

$$G_1(s) = G_0(s)L_{sc}^{k} \tag{5.5}$$

while all other physical parameters are also scaled using Froude scaling. Note, the factor of L_{sc}^{k} can also be arrived upon by recalling that a ratio of some given radiation IRF, $h_r(t)$, and a scaled radiation IRF will also be a factor of L_{sc}^{k}. Therefore, if the estimated transfer functions accurately replicate the magnitude and phase of the corresponding radiation FRFs, the estimated transfer functions can be scaled by a factor of L_{sc}^{k}.

5.3 Case Studies

The algorithm is demonstrated using a single cylindrical buoy and a nine-buoy WEC array. The cylindrical WEC buoy represents a prototype that can be tested at a typical wave-tank facility. The incoming waves were set parallel to the $+x$-direction. An axisymmetric body makes for a good candidate for hydrodynamic analysis because of symmetry. This Section compares the accuracy and passivity characteristics of the estimated transfer functions' Frequency Response Function (FRF). Falnes et al., and Folley used the non-dimensionalized hydrodynamic coefficients while discussing the radiation FRF, and IRF characteristics [37, 40]. The estimated radiation transfer functions shown here can be conveniently non-dimensionalized and scaled using the cube of the characteristic length (represented as *ULEN* or L in WAMIT documentation).

For a single WEC, the estimation process generates a 6×6 transfer function array $G(s)$, whose diagonal elements correspond to self-interacting modes and off-diagonal elements correspond to coupled modes. This chapter shows the *Heave* mode only, but similar analyses can be carried out for other modes and mode couplings. For the single WEC case, the algorithm is demonstrated using a frequency domain route and two time-domain routes (see Section5.2.1). Henceforth, the estimated transfer function array, estimated using the frequency domain route, will be denoted by $G_{H_r}(s)$.

For time-domain routes, when the reference radiation IRF, $h_r(t)$, is calculated using Filon's integration, the estimated transfer function array will be denoted by $G_{Filon}(s)$, and when the radiation IRF, $h_r(t)$, is calculated using Euler integration, the estimated transfer function array will be denoted by $G_{Euler}(s)$.

The accuracy of the estimated transfer function array, $G(s)$, is demonstrated by comparing its FRF with the radiation FRF $H_r(\omega)$ matrix constructed with the purely *Heave* modes and their couplings. The passivity characteristics are quantified using the input passivity index ν, such that $\nu = \frac{1}{2} min_{\omega} \lambda_{min}(G(j\omega) + G(-j\omega))$, where λ_{min} are the minimum eigenvalues of $(G(j\omega) + G(-j\omega))$. The accuracy of the FRF is assessed using Normalized Root Mean Square Error (NRMSE) fitness percentage, such that,

$$NRMSE(\%) = 100 \times \left(1 - \frac{||y - \hat{y}||}{||y - mean(y)||}\right), \tag{5.6}$$

where y is the validation data, which would be the magnitude of the radiation FRF $H_r(\omega)$, while $\hat{y}$ would be the FRF of the $G(s)$ being assessed.

5.3.1 A Single WEC

The single WEC was modeled as a cylinder of radius of 1 m and draft 1 m, such that the radius to draft ratio is unity. The algorithm was initiated with an $N_0 = 10$ poles (see Section 5.2.2 and Figure 5.1). The higher-order transfer functions had high accuracy but did not satisfy the passivity requirements, while the converse was true for lower-order transfer functions. The final estimated transfer functions had satisfactory accuracy and had a positive input passivity index ν, for the frequency bandwidth in which radiation damping data from WAMIT was greater than 0. Convergence studies of the hydrodynamic coefficients generated by WAMIT. Appendix B discusses the convergence study for this case in greater detail. The comparison of different mesh resolutions shown in Appendix B helped choose a suitable mesh size that had negligible difference when compared to a much higher resolution mesh.

5.3.1.1 Comparison of Frequency Response of estimated transfer functions

Figure 5.3 shows the comparison of frequency response characteristics of $G_{H_r}(s)$, $G_{Euler}(s)$, and $G_{Filon}(s)$. Notice that all estimated transfer functions are minimum-phase. The phase plots show that the phase for all transfer functions stays between

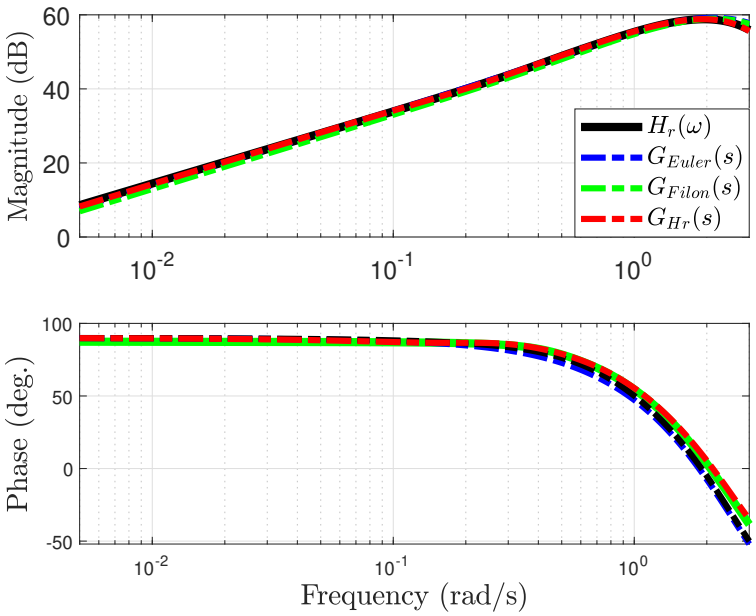

Figure 5.3: Comparison of magnitude and phase of $H_r(\omega)$ with FRFs of $G_{H_r}(s)$, $G_{Euler}(s)$, and $G_{Filon}(s)$ for a cylinder with a radius of 1 m and draft 1 m, in heave mode.

$\pm\pi/2$, which suggests positive-realness and passivity. This corresponds to the Nyquist plot being in the right-hand plane for a SISO system. The FRF of the estimated transfer functions is compared to the $H_r(\omega)$. All three routes are minimum-phase with phase plots between $\pm\pi/2$ rad. Figure 5.4 shows the NRMSE fit percentage for the frequency domain route and the two time-domain routes as a function of frequency by comparing the radiation FRF $H_r(\omega)$ and the FRFs of $G_{H_r}(s)$, $G_{Euler}(s)$, and $G_{Filon}(s)$. Using one method over the other can be decided based on a range of factors, such as operating frequencies and computational limits when using higher-order transfer functions Interestingly, for some frequencies between 0-2.0 rad/s, the $G_{H_r}(s)$ results in a poorer match than $G_{Euler}(s)$, owing to sensitivity in the frequency method, as discussed in Section5.6. However, for the overall frequency bandwidth, the

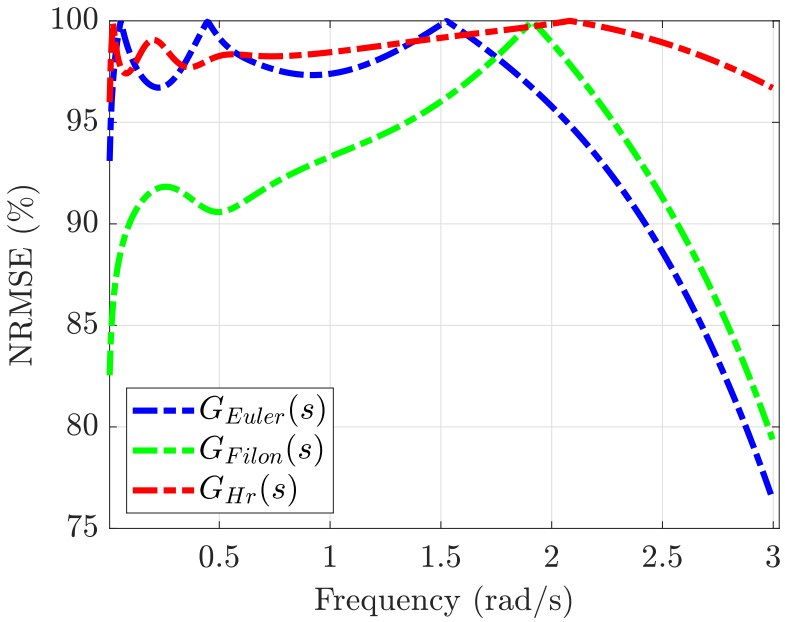

Figure 5.4: The Normalized Root Mean Square Error (NRMSE) fit between the magnitude of the radiation FRF $H_r(\omega)$, and the FRFs of $G_{Hr}(s)$, $G_{Euler}(s)$, and $G_{Filon}(s)$ for a heaving cylinder with a radius of 1 m and draft 1 m. The frequency range for this comparison is $0 - 3.0$ rad/s. For most frequencies, the FRF of $G_{Hr}(s)$ has the best match with the radiation FRF $H_r(\omega)$.

direct method, i.e., the frequency domain method, has the best accuracy performance, while $G_{Filon}(s)$ performs better than $G_{Euler}(s)$ at relatively higher frequencies.

5.3.1.2 Comparison of Input Passivity Index of estimated transfer functions

Figure 5.5 shows that the estimated transfer functions have a positive input passivity index between 0 to 4 rad/s. Therefore, the estimated transfer functions will have passivity for the frequency bandwidths where ν is positive. Since this chapter is

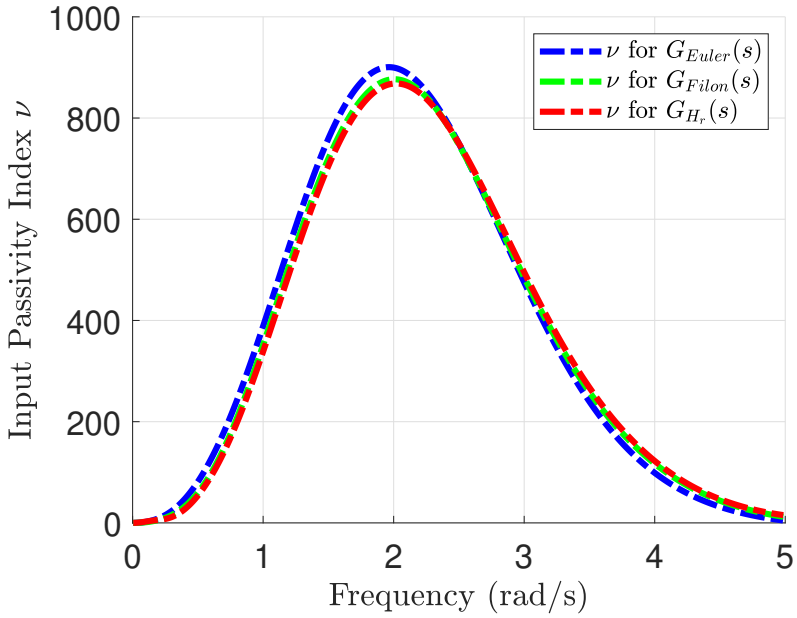

Figure 5.5: Comparison of Input Passivity Index, ν, for $G_{H_r}(s)$, $G_{Euler}(s)$, and $G_{Filon}(s)$ for a cylinder with a radius of 1 m and draft 1 m, in heave mode.

only using the heave mode, the transfer function system is a single transfer function corresponding to that mode, and therefore, the input passivity index reduces to the FRF of the corresponding estimated $G(s)$. In other words $\nu = \frac{1}{2} min_{\omega} \lambda_{min}(G(j\omega) + G(-j\omega)) = \frac{1}{2}(2G(j\omega))$ for SISO LTI systems. Note that for multi-mode analyses, such as MDOF systems or multibody systems, the transfer function system will be a MIMO transfer function matrix and therefore would not reduce to $G(s)$. As discussed in Section 5.1, stability analyses can also be done using the Nyquist criterion; however, it is limited to SISO systems. The input passivity index analyses shown here make the stability analyses simpler, especially for MDOF and multibody systems, as shown in the following Subsection.

5.3.2 A Homogeneous WEC Array of Nine Cylindrical WECS

For a WEC array, the self-interacting modes and their mutual couplings result in a $6N \times 6N$ radiation FRF array. The hydrodynamic coefficients were calculated using WAMIT and convergence studies helped decide appropriate mesh resolution (see Appendix B). For this chapter, only the *Heave* modes and their mutual couplings are considered, such that the radiation FRF array was a $N \times N$ array. Increasing the packing density of a WEC array affects the mode-couplings due to increased interaction between the array members. For the nine-buoy WEC array, the $G(s)$ was estimated using the frequency-domain route only. The $G(s)$ were estimated at different packing densities by varying the mutual distances d between the WECs. The mutual distances are based on the compact array's area fraction, a quantity defined here as a packing ratio, initially introduced by Garnaud and Mei for homogeneous compact arrays made up of cylinders [46]. The packing ratio, f is defined as,

$$f = \frac{\pi R^2}{d^2} \tag{5.7}$$

Where, R, is the radius of a single-cylinder, and d is the center to center distance between two adjacent cylinders. The $G(s)$ was estimated for the packing ratios of

1.257×10^{-3}, 5×10^{-3}, and 1×10^{-1} corresponding to the center to center distance between two adjacent bodies, $d = 50.00\ m, 25.06\ m$, and $5.60\ m$ respectively. The array layout is shown in Figure 5.6. The cylinders are assigned body indices, incremented along the $+x\ axis$ and then along the $+y\ axis$. The body indices are shown in figure 5.6.

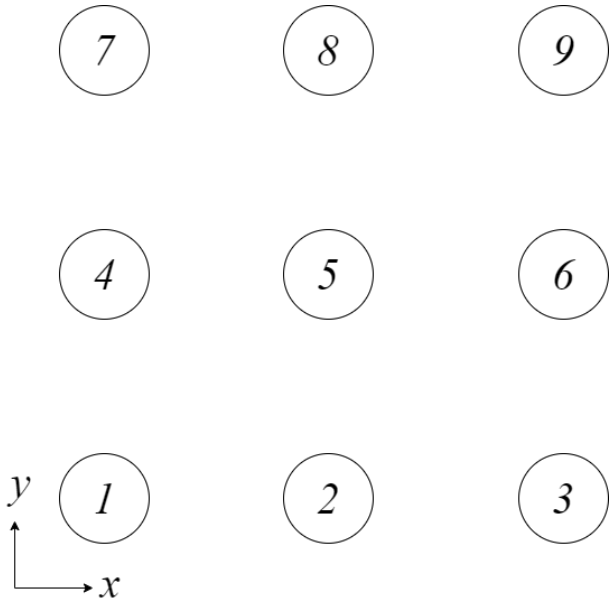

Figure 5.6: Compact array layout of 9 cylinders.

The WEC array has 9 cylinders of a radius of 1 m and draft 1 m, such that the radius to draft ratio is unity. In the discussion that follows, the indices of the data correspond to mode couplings. For instance, the data corresponding to $(1, 1)$ corresponds to body 1-body 1 mode coupling; in other words, this corresponds to the radiation force transfer function for body 1 in heave mode with no coupling since this mode combination is a diagonal element of the transfer function array. On the other

hand, the data corresponding to $(1, 5)$ corresponds to body 1-body 5 mode coupling, which is an off-diagonal term in the transfer function array $G(s)$; in other words, this corresponds to the radiation force transfer function for the body 1 in heave mode coupled with the heave mode of body 5.

5.3.2.1 Effect of packing density on $H_r(\omega)$ and $G(s)$

The magnitude of the diagonal mode-couplings corresponding to the self-interacting *Heave* is as much as 400 % higher than the maxima of the off-diagonal radiation FRFs. This shows that the off-diagonal terms representing the coupled modes have significantly less contribution to the buoy dynamics. Therefore, although some of the off-diagonal estimated transfer functions have low matches, their contributions do not impact the overall motion dynamics. This would be demonstrated by time histories of the motion dynamics discussed in the next Section. As discussed in Subsection 2.3.1, WEC arrays exhibit a 'trapping effect' which results in an increase in radiation damping coefficients for centroidal buoys with respect to the surrounding circumjacent buoys [56, 116]. Garnaud and Mei derived the modified wave potential for a compact array [46]. Husain and Parker expanded their work by including the contributions of the frequency-dependent hydrodynamic coefficients and showed that the radiation damping increases for the centroidal buoys in compact arrays due to hydrodynamic couplings [56]. The radiation damping coefficients (real-part of $H_r(\omega)$)

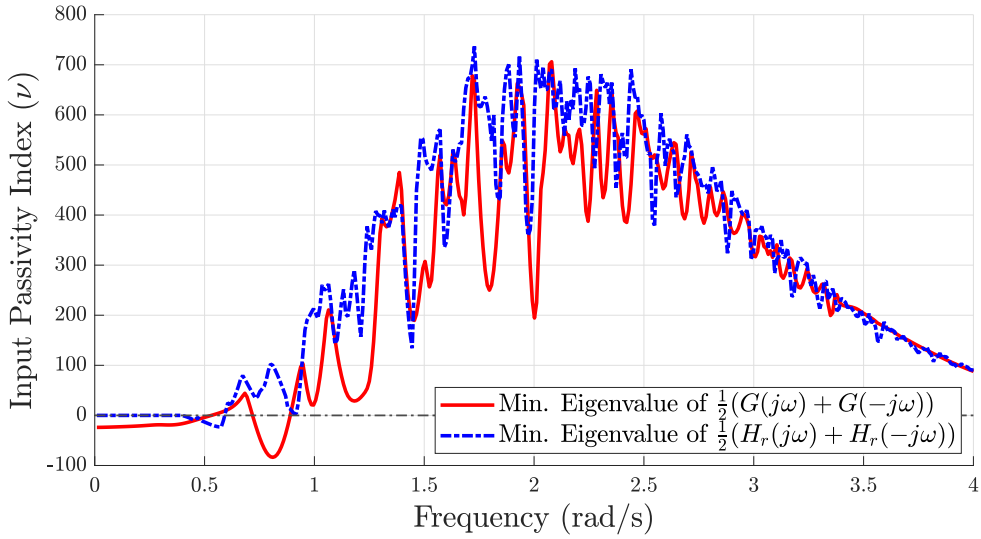

Figure 5.7: Input passivity index, ν, for nine-buoy WEC array with an inter-buoy distance of 50 m.

for the *Heave* mode for the buoy 5, which is surrounded on all sides, is slightly higher than the radiation damping of its neighbors. Decreasing the inter-buoy distance further increased the 'trapping effect'

Hydrodynamic couplings are quite significant as the packing density of the WEC array is increased as the inter-buoy distance is reduced from 50 m to 25.06 m, and finally to 5.6 m.

5.3.2.2 Effect of packing density on the Input Passivity Index, ν.

Figures 5.7 - 5.9 compare the input passivity indices of the estimated transfer function arrays of the aforementioned WEC arrays against the corresponding function formed

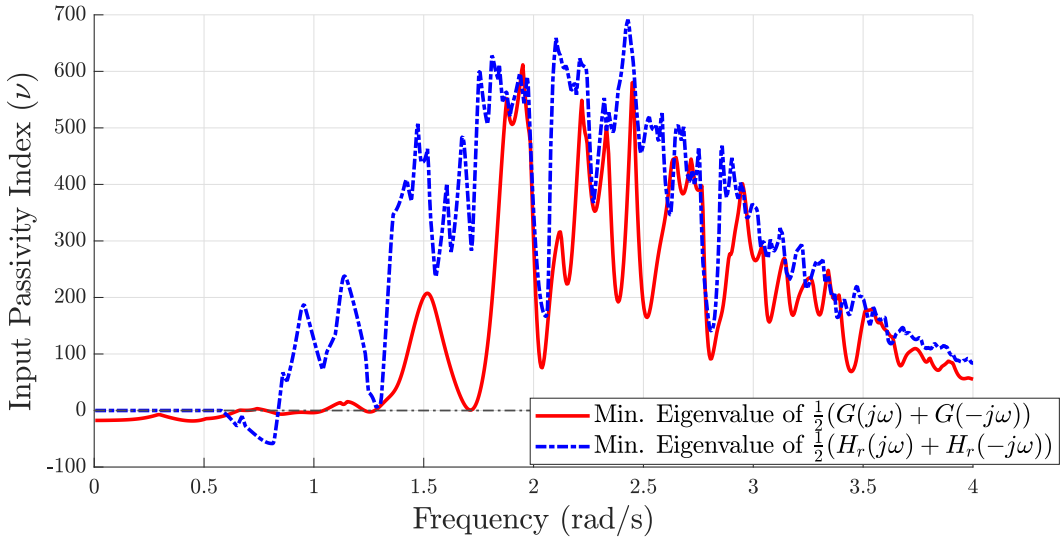

Figure 5.8: Input passivity index, ν, for nine-buoy WEC array with an inter-buoy distance of 25.06 m.

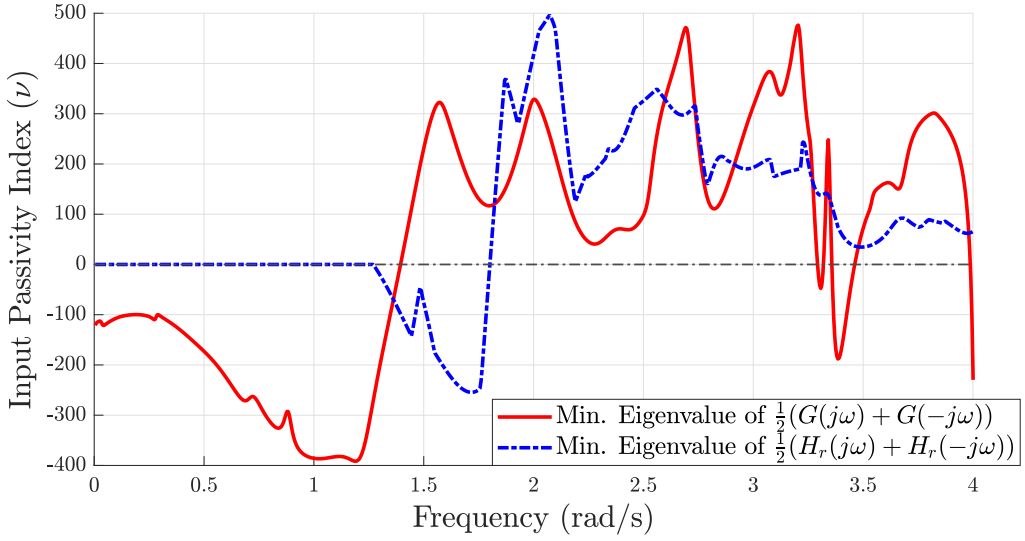

Figure 5.9: Input passivity index, ν, for nine-buoy WEC array with an inter-buoy distance of 5.6 m.

using the radiation FRF, $H_r(\omega)$, at each frequency step. While comparing Figure 5.7 with the input passivity index of the single-cylinder case in Figure 5.5, it can be observed that the ν for the WEC array has multiple local maxima or 'lobes'. These

lobes can be attributed to the hydrodynamic interactions and couplings in the WEC array. The radiation force is dissipative, and its IRF decays with time, so in the array, with an inter-buoy distance of 50 m, the wake of the radiation IRFs lose most of its energy by the time that radiation impulse reaches adjacent buoys. Reducing the inter-buoy distance increases the hydrodynamic coupling and increases the sensitivity of the numerical stability of the radiation force calculations. This phenomenon can be observed in the ν for the more compact array with an inter-buoy distance of 25.06 m by its loss in passivity. Notice in Figure 5.8 that the passivity, which indicates the energy dissipation drops for the reference radiation FRF as well. Although the overall system is dissipative, with an increase in packing density, as the hydrodynamic couplings increase, the *Heave* modes also have significant coupling with non-heave modes such as *Surge* and *Pitch*. This can be inferred by the increase in the magnitudes of mode-couplings between modes corresponding to different degrees of freedom. This results in the energy dissipation of only heave modes, and its couplings manifest a drop in passivity due to increased hydrodynamic couplings. The natural frequency of the cylinder with a radius of 1 m and draft 1 m is approximately 0.8 rad/s. As the numerical sensitivity of the passivity index increases with the packing density of the array, the energy dissipation at the resonance frequency and its harmonics decrease, as can be empirically observed from Figures 5.7 - 5.9.

The most compact array with an inter-buoy distance of 5.6 m shows a further decline in ν due to significantly higher hydrodynamic couplings. Note, as observed by

Taghipour et al. a lack of passivity doesn't necessarily mean lack of stability [115]. Further, the assumptions made in Table 5.1 do not hold for a compact array due to hydrodynamic couplings. As cited earlier, the wave potential in a compact array is modified, and therefore whilst analyzing the passivity of a compact array, all modes and their couplings (a $6N \times 6N$ array, where N represents the number of buoys) should be considered. However, this chapter is limited to the analysis of the heave modes and their couplings. The authors hypothesize that the transfer function array with all modes and their couplings (a $6N \times 6N$ array) would be a dissipative system and thus have a positive passivity index. As shown in the next Section, all array configurations have stable motion dynamics with high accuracy ($> 90\%$).

5.4 A Heterogeneous WEC Array of Cylindrical WECs and a CorPower Device

This Section demonstrates the algorithm using a heterogeneous array comprised of a CorPower device surrounded bu eight cylindrical WECs. The CorPower device specifications can be found at [135]. It can be described as a combination of three shapes: a cylinder of a diameter of 8.4 m and height of 4.6 m, over an inverted-truncated cone (inverted nightlamp-like shape) geometric Section whose top radius is 8.4 m and bottom radius is 1.25 m. The third and bottom-most part of the device

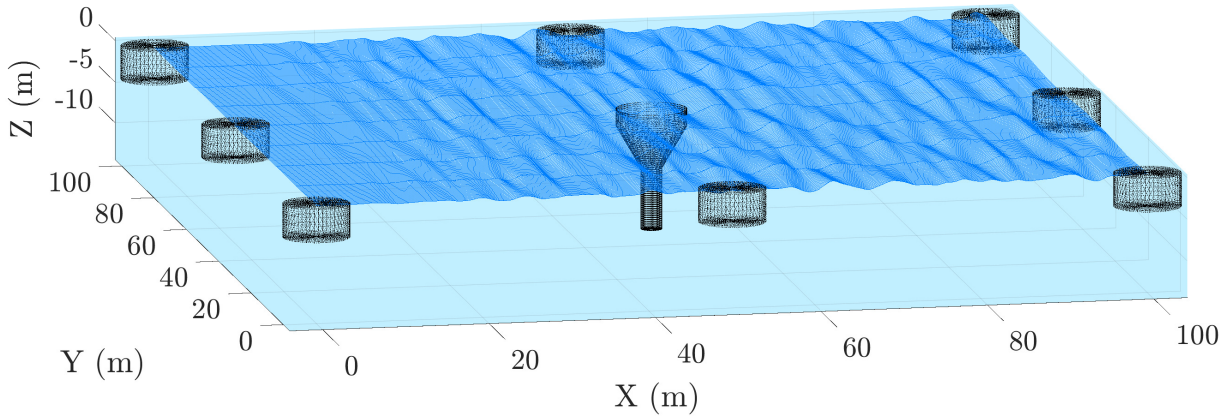

Figure 5.10: The spatial layout of the heterogeneous WEC array. The wave-field shown represents the PM spectrum used in this Section.

extends as a cylinder of radius 1.25 m for length of 7.32 m. The draft of the device is 14.5 m measured from the bottom-most surface of the device. The other WECs in the array had a cylindrical geometry of radius 4 m. The hydrodynamic coefficients were calculated using WAMIT and convergence studies helped decide appropriate mesh resolution (see Appendix B).

This heterogeneous WEC array was designed to represent a realistic deployable compact array. The distance between any two neighboring bodies was 50 m along the $+X-$axis and $+Y-$axis. The hydrodynamics were calculated assuming plane-progressive waves propagating along the $+X-$axis Figure 5.10 shows the heterogeneous WEC array's spatial layout.

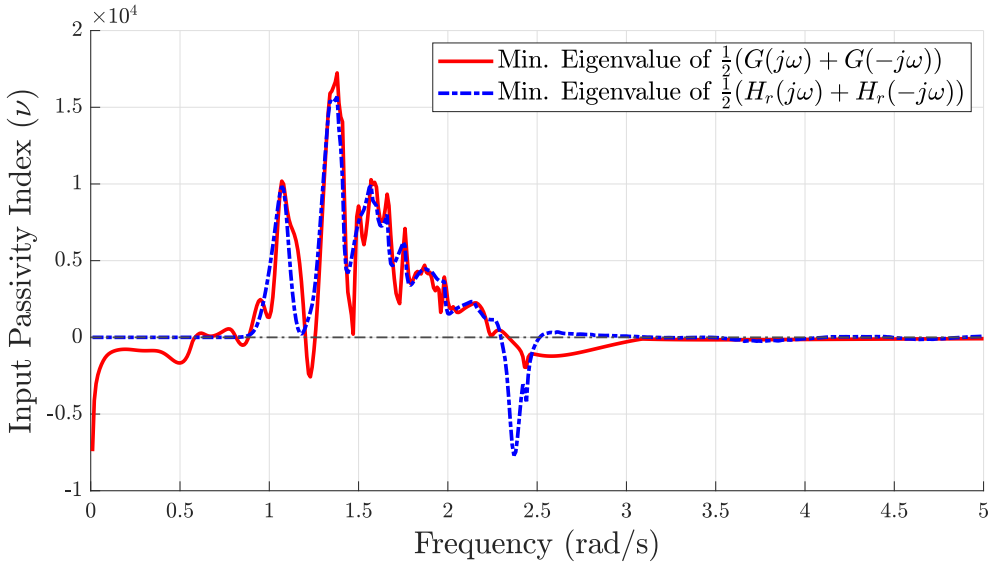

Figure 5.11: Passivity Index, ν, as a function of wave frequency.

5.4.1 Passivity Index, ν for the Heterogeneous WEC Array

The WECs in the heterogeneous array had a much higher volume (16 times of the cylinders in previous cases), and the heterogeneous array had much hydrodynamic interactions. The multiple lobes in the passivity index of the heterogeneous array in Figure 5.11 indicate hydrodynamic couplings in the system. Interestingly, the minimum eigenvalues of the radiation FRF are negative at higher frequencies, indicating couplings with other modes, such the energy in the heave modes is being dissipated using the other modes of the WECs. All estimated transfer functions matched with the corresponding reference radiation FRF by more than 90 % in terms of NRMSE error introduced in the previous cases.

5.5 Motion Simulations

A motion simulation model was created based on the Cummins' equation discussed in Section 3.3. Only heave mode is presented here, such that the generalized motion coordinates $\underline{q}(t)$ can be replaced by heave displacements, $\underline{x(t)}$. Also, the generalized external forces $\underline{Q}(t)$ can be replaced by the excitation force, $\underline{F_{exc}}(t)$, and control force, $\underline{F_c}(t)$.

Rewriting the Cummins' equation, (3.30) as,

$$\underline{\ddot{x}}(t) = \frac{1}{\mathbf{M} + \mathbf{a}_\infty} \left[\underline{F_{exc}}(t) + \underline{F_c}(t) - \underline{F_R}(t) - \mathbf{K}\underline{x}(t) \right] \tag{5.8}$$

5.5.1 The Single WEC Case

The dynamics equation shown in (5.8) is used to simulate the complete dynamics model in the time-domain. The complete dynamics model was set up in MATLAB-Simulink. The hydrodynamic coefficients were calculated at a water depth of 100 m. The excitation force was calculated offline prior to the simulation. The cylinder was approached by a regular wave of amplitude 0.25 m and wave period 6.22 *seconds*. For these motion simulations, no control force was applied, and the cylindrical body

only experienced the excitation force as an input.

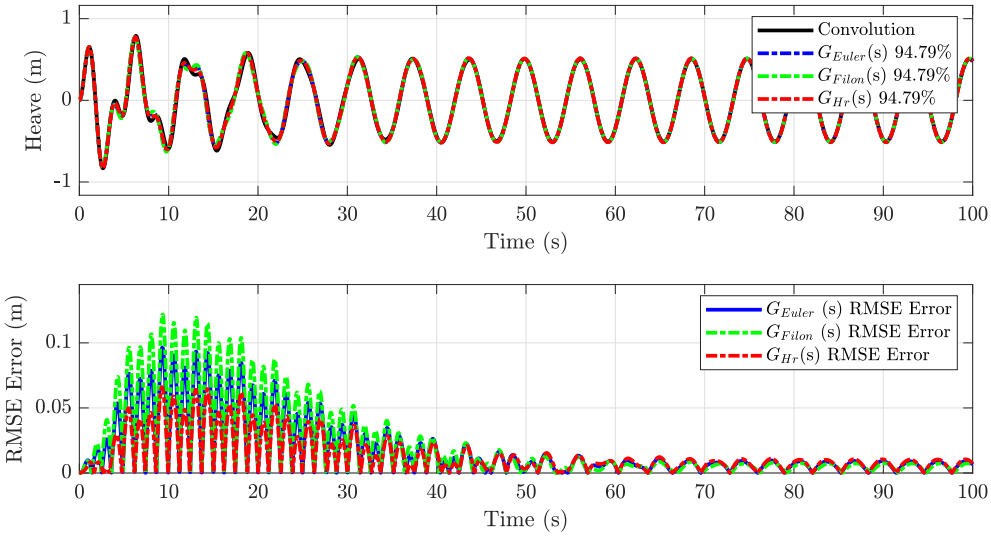

Figure 5.12: Body motion in heave mode for the cylinder with a radius of 1 m and draft 1 m (Small Buoy), when the radiation force is calculated using $G_{H_r}(s)$, $G_{Euler}(s)$, and $G_{Filon}(s)$ compared to the body motion in heave mode when the radiation force is calculated using the convolution. The overall NRMSE match is expressed as a fitness percentage in the legend of the upper plot, while the lower plot shows the root mean squared error (RMSE) as a function of time.

Figure 5.12 shows the heave motion characteristics for a period of 100 *seconds*. The simulation was first run such that the radiation force was calculated using direct convolution and then using the estimated transfer functions. These body-motion simulations were done in Simulink.

These simulations were run for only the heave mode but can be easily run for any other mode or mode combination, appropriately using the estimated transfer function matrices. Figure 5.12 shows the heave motion for a single regular wave. The models can be easily used for irregular waves if the wave input horizon can be reliably

predicted in advance.

Note that in Figure 5.12, the motion simulation shows some transient behavior at the beginning of the time history. It is the result of the buoys being released from rest at $t = 0$, while the fluctuating behavior seen at the start of the bottom figure in Figure 5.12 is numerical. This fluctuating behavior can be mitigated by using a *ramp* function as done in the WEC simulator package WEC-Sim [102]. However, such pre-processing or truncation was not done for this case to show the initial transient behavior. The overall NRMSE matches for all estimated transfer functions approach 99% if the initial 40 *seconds* of data is truncated.

After the initial transient behavior, the RMSE reduced significantly and converged for all three routes. This indicates that all routes have a similar impact on the overall motion dynamics once the initial numerical transient period is passed. Note that the dynamics model shown here used a linearized model, but the analyses shown here can be easily adapted for a model that uses non-linear Froude-Krylov forces as the external forces acting on the body.

5.5.2 The Homogeneous WEC Array Cases

A transfer function matrix $G(s)$ was formed using the body-only heave modes and the inter-body heave mode couplings. The dynamics equation of motion in (5.8) is

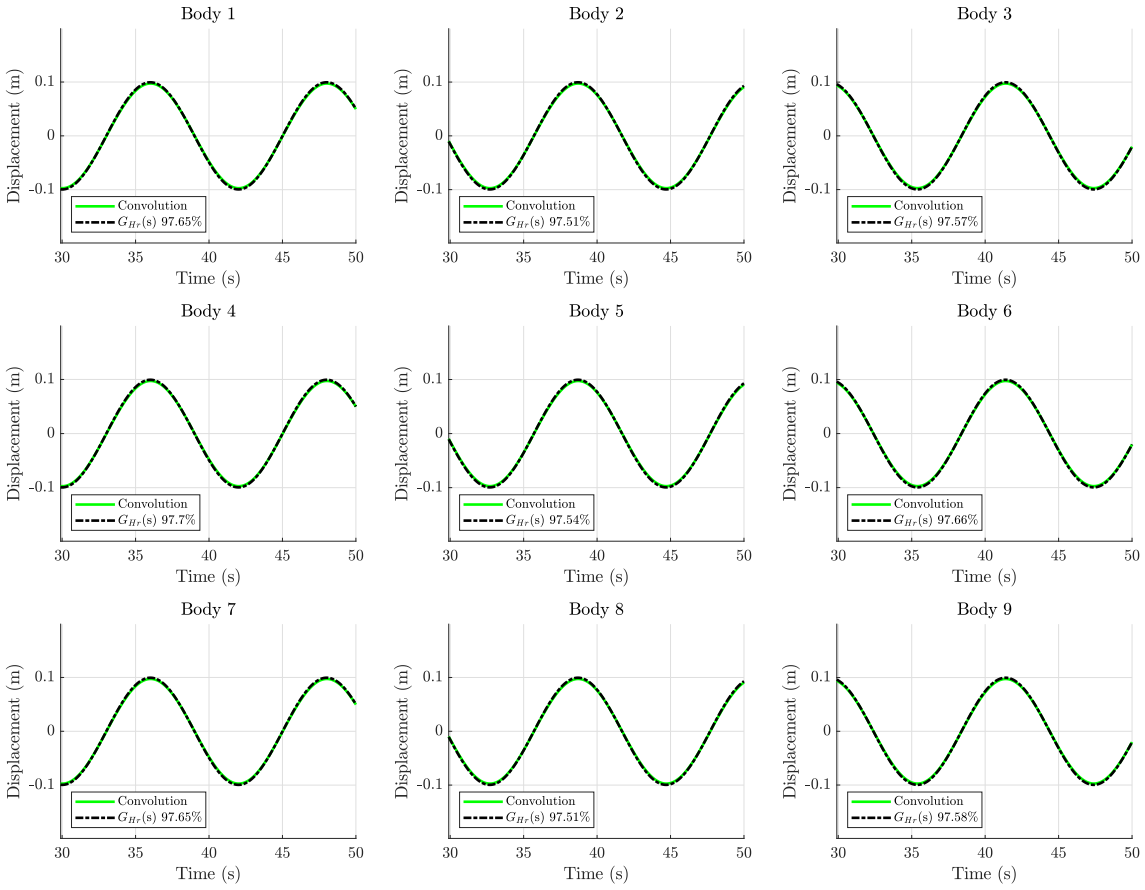

Figure 5.13: Displacements when $F_R(t)$ is calculated using estimated transfer functions, compared with displacement when $F_R(t)$ is calculated using direct convolution for the WEC array with an inter-buoy distance of 50 m.

used to simulate the complete dynamics model in the time-domain using MATLAB-Simulink. The excitation force was calculated offline to the simulation. The cylinders were approached by a regular wave of amplitude 0.25 m, , and wave period 12 s (wave frequency of $\pi/6$ rad/s). For these motion simulations, no control force was applied, and each cylindrical body only experienced the excitation force as an input.

Figure5.15 shows the heave motion characteristics such that the simulation was first

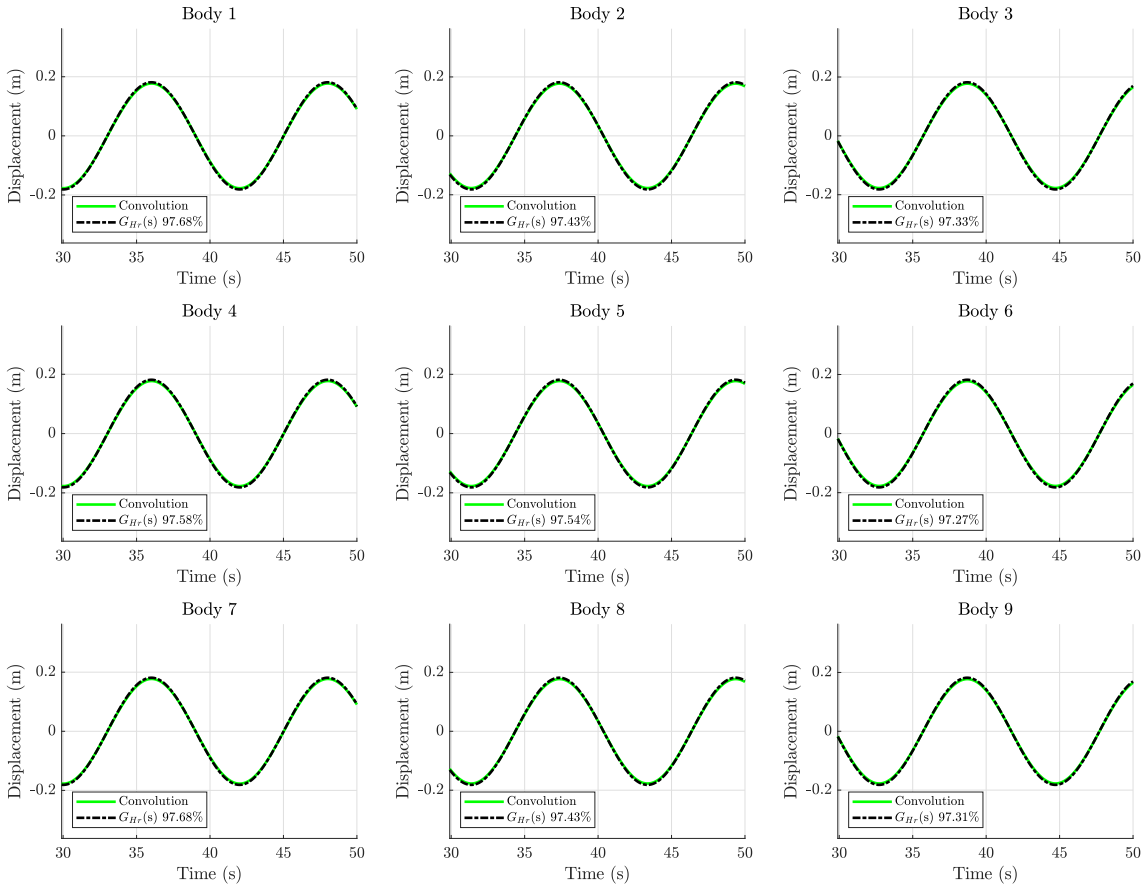

Figure 5.14: Displacements when $F_R(t)$ is calculated using estimated transfer functions, compared with displacement when $F_R(t)$ is calculated using direct convolution for the WEC array with an inter-buoy distance of 25.06 m.

run by calculating the radiation force using real-time convolution and then run again by calculating the radiation force using the estimated transfer function matrix. These simulations were run for only the heave mode but can be easily run for any other mode or mode combination, appropriately using the estimated transfer function matrices. The most compact array configuration showed a greater than 96 % match with the simulation that used the convolutions to calculate the radiation forces. The WEC

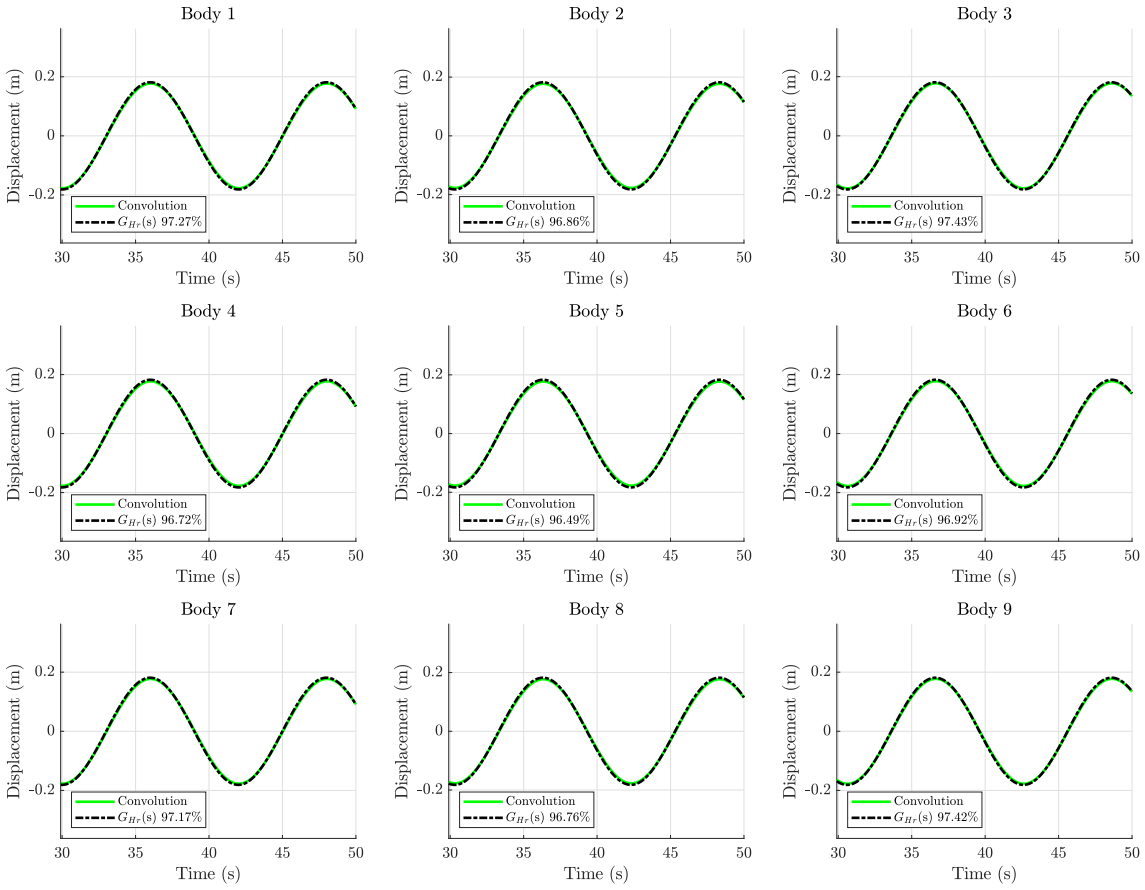

Figure 5.15: Heave displacements of the 9 body compact array when $F_R(t)$ is calculated using estimated transfer function array, compared with displacements when $F_R(t)$ is calculated using direct convolution for the WEC array with an inter-buoy distance of 5.6 m.

array configurations with greater inter-buoy distances had slightly better matches.

The wave inputs for the compact array vary depending on the body location. The WEC arrays were acted upon by a two-dimensional wave in the $x - z$ *plane*, so the wave elevation was the same across the y *axis*. However, for bodies along the x axis, the phase at which the bodies experienced the incoming wave was different.

The incident wave elevations experienced by the bodies were calculated using the wave propagation equation. Equation (5.9) uses the Cartesian coordinates such that x-direction is positive from left to right, while z-direction is positive when moving up. The general equation for wave elevation of a water wave propagating in positive x-direction can be described as [40, 85],

$$\eta(x, z; t) = \frac{\iota g A}{\omega} \frac{\cosh(k(z+h))}{\cosh(kh)} e^{kz} e^{-\iota(kx-\omega t)} \tag{5.9}$$

Where $\eta(t)$ is the temporal displacement in the x and z-direction. For surface waves, $z = 0$, and A is the amplitude of the water wave, (5.9) then reduces to

$$\eta(x, t) = \frac{\iota g A}{\omega} e^{-\iota(kx-\omega t)} \tag{5.10}$$

The argument in the exponential part of the equation ($e^{-\iota(kx-\omega t)}$ carries the phase information of the wave. Assuming that no phase is added to the wave as it progresses through the WEC array, equation (5.10) can be used to relate the phase at which the wave approaches a particular WEC buoy in the array. The inter-buoy spacings in the $+x$-direction were set at 50 m, 25.06 m, and 5.605 m. For the layout shown in Figure,5.6 the WEC array with inter-buoy spacing set at 5.605 m, the x coordinate of the bodies 1, 4, and 7, was 0 in (5.10). For bodies 2, 5, and 8, the x coordinate

was 5.605 m, and for bodies 3, 6, and 9, the x coordinate was 11.210 m. The percentages shown in Figures 5.13 - 5.15 are the NRMSE fit percentage between the body motion when the radiation force is calculated using the estimated transfer function arrays, compared to the body motion when the radiation force is calculated using the convolution of radiation IRF, $h_r(t)$, and body velocity.

As discussed for the single-cylinder case, the initial transient time histories for the WEC array buoys were truncated. The accuracy percentages in Figure 5.15 show the comparison between 20 s to 50 s. As before, the time-domain model can be simulated for irregular waves if the time history of the elevations can be reliably predicted before the simulation. These irregular wave elevation time histories can then be convoluted with the excitation force IRF to calculate the inputs to the WEC array buoys. Additionally, if the time histories for non-linear Froude-Krylov are provided, the model can accommodate such inputs.

Note the WEC arrays modeled here didn't incorporate the contributions of non-heave modes to heave time histories due to hydrodynamic coupling. A more realistic WEC array model would include the contributions of the support structure and moorings that would maintain the WEC array layout. This would further introduce forces and couplings of dynamics modes WEC buoys.

5.5.3 The Heterogeneous WEC Array Case

The heterogeneous WEC array was simulated with irregular waves modeled using the Pierson-Moskowitz spectrum, with a significant wave height, $H_S = 1\ m$ and a significant wave period of 8 s. This wave climate is representative of moderate swell seas.

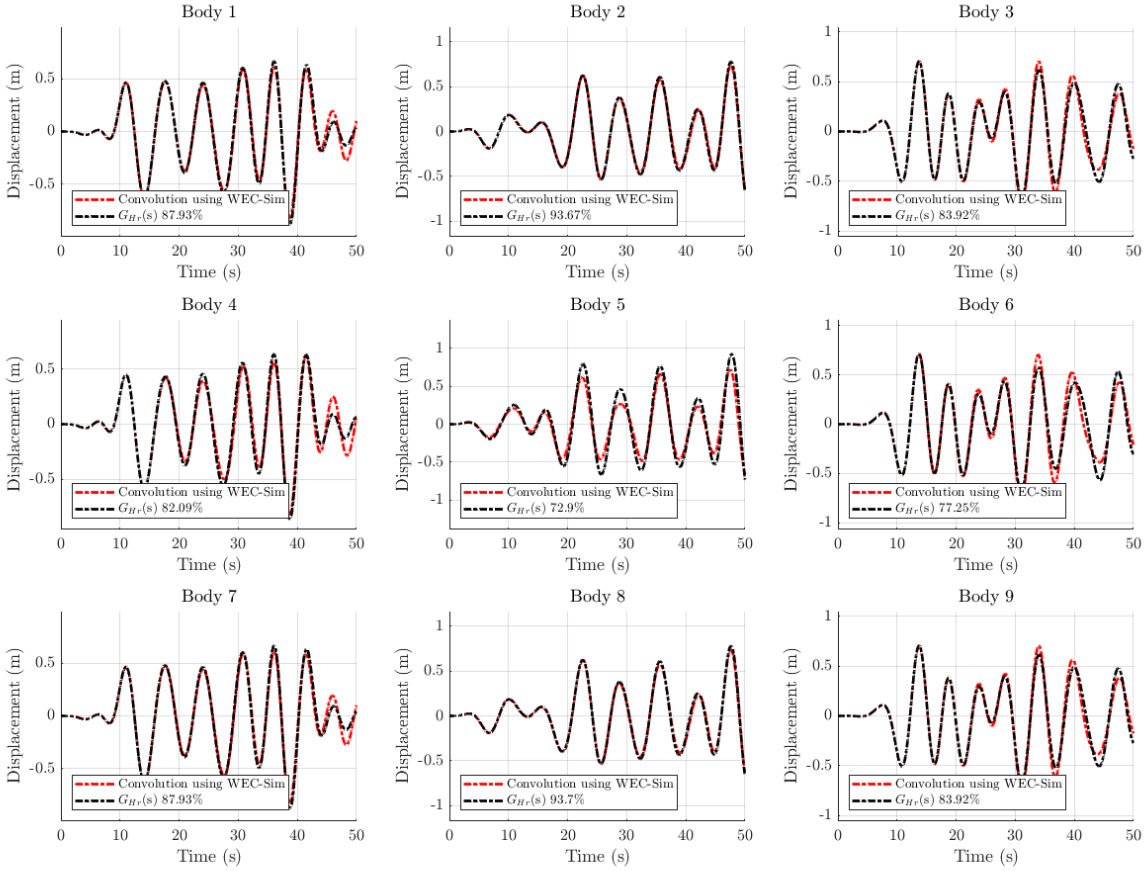

Figure 5.16: Heave displacements of the heterogeneous WEC array when $F_R(t)$ is calculated using estimated transfer function array, compared with displacements when $F_R(t)$ is calculated using direct convolution

5.6 Discussion

Frequency domain and time-domain estimation methods were used to estimate transfer functions between body velocity and radiation forces. Frequency domain estimation methods are the most direct route to generate the desired time-domain models. Over the years, many researchers have raised reservations over frequency domain estimation methods [91, 115]. Taghipour et al. point out that frequency domain approaches can result in overfitting because the approximated models can have higher than necessary orders [115].

Frequency domain estimation methods are more sensitive than the time-domain methods, especially to the numerical errors in the numerically calculated hydrodynamics coefficients at very low frequencies ($< 0.1\ rad/s$) and at very high frequencies ($> 10\ rad/s$) [91]. This sensitivity is an artifact of the hydrodynamics coefficients from BEM solvers such as WAMIT having numerical errors for very low frequencies and very high frequencies, especially for geometries with horizontal panels [133]. Also, for some cases, the generated radiation damping can have negative values or outliers at a few frequencies, especially around the body's natural frequency and irregular frequencies [40]. Therefore, direct estimation methods are further challenged when curve-fitting an equivalent LTI radiation force transfer function. Whereas, time-domain methods can desensitize the estimation process because the radiation IRF,

while incorporating the hydrodynamics, expresses the reference function with more data points. The calculated IRFs, to put it simply, smoothen out the hydrodynamic information over more data points, making the estimation less sensitive.

Perez and Fossen also point out that frequency-domain estimation methods match better for lower frequencies [91]. Therefore, the frequency domain estimation methods can be vulnerable to losing the nuances of the system's physical characteristics at higher frequencies, owing to their sensitivity and tendency to overfit by using higher orders. The literature overwhelmingly uses time-domain estimation methods to replace the radiation force $\vec{F}_R(t)$ convolution, which needs the calculation of radiation IRF, $h_r(t)$, as the estimation benchmark. The radiation IRF, $h_r(t)$, calculations are typically done using Euler integration or trapezoidal integration [1, 69, 91, 115, 142]. This chapter explored the effect of using a significantly more accurate integration method, Filon's integration method, formulated especially for kernels resembling the radiation IRF, $h_r(t)$. However, the higher accuracy in calculating the radiation IRF, $h_r(t)$ using Filon's integration method came at a higher computational cost.

5.6.1 The Single WEC Case

The estimated models were assessed on two metrics: how well the estimated models replicated the FRF of the radiation FRFs, and secondly, how well was the body

motion replicated when the radiation force was calculated using the estimated models as opposed to calculating the radiation force using convolution. Interestingly, the algorithm can achieve more accurate transfer functions using the direct estimation or frequency domain route despite its sensitivity while satisfying passivity conditions. The accuracy of time-domain methods can be improved by using the more accurate Filon's integration to calculate the radiation IRF, $h_r(t)$, especially at relatively higher frequencies.

Given how close the motion dynamics of the body are, it is very difficult to ascertain which estimated model is closest to the actual physical phenomena, especially since the hydrodynamic data, used for calculating the reference radiation FRF $H_r(\omega)$, and radiation IRF, $h_r(t)$, are based on hydrodynamic coefficients calculated using BEM solvers. This is especially applicable for the time-domain routes because the extent of numerical characteristic root error in the integration for Euler and Filon's method changes at each function evaluation of the IRF [6, 9].

As discussed in Section5.2.2, the algorithm tries to strike a balance between the accuracy of the estimated transfer function and its passivity characteristics by iterating upon the order of the estimated transfer function system. Empirically, increasing the order of the estimated transfer function system increases its accuracy while decreasing its passivity and vice versa.

The Boundary Element Method (BEM) algorithm used by WAMIT produces some

numerical discontinuities due to irregular frequencies, especially at higher frequencies when the hydrodynamic coefficients approach their asymptotic values. However, marine systems operate at relatively low-frequency bandwidths. For instance, JONSWAP and Bretschneider wave spectrums have the most energy concentrated between 0 to 1.5 rad/s [40, 66, 85]. Therefore, for marine applications, the estimated transfer functions should have passivity characteristics.

Interestingly, the comparison of body motions shows that the transfer functions from either approach achieve qualitatively similar results. Similar observations were made by Taghipour et al., suggesting that the body motions tend to be less sensitive to the otherwise sensitive LTI system estimation process [115]. However, effective and optimal motion-control design requires that the model-based controller be based on the physical phenomenon's most accurate representation.

Significantly, the estimated systems did not have high-frequency poles, despite estimated LTI systems being high order systems. Low order estimation methods compromise the accuracy of fit in favor of stability and robustness, resulting in underfitting, as was the case in [91, 115]. Conversely, high order estimation methods compromise guaranteeing stability and robustness because they have poles faster than the physical system's properties due to overfitting [91, 115]. The estimation algorithm succeeded in preventing underfitting and overfitting while guaranteeing Hurwitz stability and ensuring passivity.

5.6.2 The Homogeneous WEC Array Cases

The case studies that are shown here demonstrate that the algorithm can model accurate and stable motion-dynamics models of MDOF marine systems with various degrees of hydrodynamic coupling. The WEC array buoys at the inter-buoy distance of 50 m are practically hydrodynamically isolated from each other. Therefore, they have almost identical $H_r(\omega)$ and $h_r(t)$ characteristics. As the packing density increases, the hydrodynamic couplings increase. Each body experiences a unique wave field based on its location in the compact array and pertinent hydrodynamic couplings.

The off-diagonal terms representing the coupled modes of the radiation FRF have highly-oscillating functions but relatively low magnitudes. The off-diagonal terms were modeled with relatively higher-order transfer functions due to the sensitivity of the coupled modes. The magnitudes of the off-diagonal terms in the sparse array ($d =$ 50 m) are numerically small and highly oscillating, making the transfer estimation more challenging. For instance, the *Body* 1 to *Body* 9 interaction has a relatively lower match but represents the coupling between the bodies at the opposite corners of the compact array. However, the algorithm achieved better matches in the more compact arrays because of the relatively higher numerical magnitudes of the off-diagonal terms.

The input passivity index (ν) showed some interesting characteristics. The increase in hydrodynamic coupling can be seen in the ν characteristics. Notice that Figure 5.7 has a more oscillatory ν when compared to the ν shown in Figure **??**. And as the packing density is further increased, the ν characteristics become more oscillatory, as the ν characteristics show the loss of passivity at some frequencies. The decline in passivity can be attributed to the increased inter-mode couplings between heave and other modes (see 5.3.2.2).

The motion time-histories from the models using the convolution-based radiation forces were used as the reference for the time-domain performance of the models using the estimated transfer function array to calculate the radiation force. Ultimately, the body motion characteristics should replicate the motion characteristics calculated using Cummins' equation. As shown in Section5.5, all cases resulted in very accurate motion characteristics while staying stable. A numerical stable time-domain model that can be analyzed in the Laplace domain using the estimated LTI systems can eventually analyze multibody dynamics of more complicated models with the necessary control.

5.6.3 The Heterogeneous WEC Array Case

The heterogeneous WEC array case was a more realistic representation of ocean deployable WECs. This case can be considered a compact array, given that the inter-WEC distance of 50 m is about 6 times the diameter of the array members. The radiation force transfer functions were estimated with > 90 % accuracy for each mode considered. The motion dynamics comparison showed a modest decline in the match because an irregular wave climate was used. The motion dynamics matches were > 94 % when regular waves were used.

5.7 Summary

The real-time convolution operation needed to calculate radiation forces can be circumvented using estimated LTI systems. Motion control of floating marine structures requires the Cummins' equation to be modified, such that the radiation force is calculated using an LTI system.

This chapter presents an algorithm to calculate radiation forces experienced by floating marine structures using an LTI system. The algorithm enforces the stability of the complete dynamics model by ensuring the passivity of the estimated LTI system.

The passivity of estimated transfer functions and the complete dynamics model is assessed using the input-passivity index. The passivity-based algorithm facilitates motion control analyses of floating marine structures. The passivity criteria are more stringent than mere gain margin criteria by ensuring the stability of the complete dynamic models. Also, the passivity-based approach, unlike the Nyquist plot-based approach, can be extended to MDOF systems with multiple modes and bodies. The modeling architecture presented here can serve as a base dynamics model for marine hydrokinetics simulations. Such a base model can then integrate and compute control forces for a model-based controller deployed on sea-worthy devices.

Although closely related, both stability and hydrodynamic couplings can be characterized using the passivity index. Not only does the passivity index ensure numerical stability, but it also indicates the degree of stability quantified as the input passivity index. Motion simulations further confirmed that the estimated transfer function array could replace the convolution operation for MDOF floating marine structures. Further work on passivity-based control can be explored. The passivity-based time-domain methods presented here can help develop a robust model-based framework for motion-control and the establishment of Marine Energy Grids, especially for power management and power control. For hydrodynamically coupled MDOF systems, the input passivity index is an important criterion for model robustness. It can be a crucial design parameter guiding the WEC array layout design, motion modeling, and control.

Chapter 6

Storage Minimization of Marine Energy Grids using Polyphase Power

Multiple Wave energy converter (WEC) buoys can be used to establish a WEC array-powered microgrid collectively forming a Marine Energy Grid (MEG). A maritime domain with gravity waves will have significant spatial variability in phase, causing the power produced by a WEC array to have high peak-to-average ratios. Minimizing these power fluctuations reduces the demand for large energy storage by WEC array-powered DC microgrids while also reducing losses in the undersea cable to the shore. Designs that reduce energy storage requirements are desirable to reduce deployment

and maintenance costs. This work demonstrates that polyphase power, in conjunction with an energy storage system, can be used to maintain constant power. This work shows that an N WEC array geometry can be designed to reduce the energy storage requirements needed to mitigate the power fluctuations if the WEC array produces constant, polyphase power. Additionally, the conditions that identify the wave frequencies and control effort needed to produce polyphase power are developed. This Chapter also shows that increasing the number of WECs in an array reduces aggregate power fluctuations. Finally, WEC array power profiles are investigated using simulation results to verify the mathematical conditions developed for a three and six WEC case.

The recommendations made in this Chapter can be easily integrated with PTO force control strategies. This Chapter proposes that the WEC array PTO force control should be informed by the advantages of producing polyphase power. This Chapter demonstrates that a WEC array that produces polyphase power will require a smaller ESS and will require less controller effort when compared to nonpolyphase power.

The rest of this Chapter is organized as follows; Section 6.1 the mathematical conditions needed to design a WEC array that produces polyphase power. A simulation case study is presented in Sections 6.2 and 6.3. Finally, a summary is given in Section 6.4.

6.1 Constant Power WEC Array Conditions

This section develops the spacing, control force phasing, regular wave frequency and energy storage control conditions so that an ideal WEC array will produce constant power. The most general case is considered first followed by a homogeneous array whose sufficient conditions for constant power are greatly simplified.

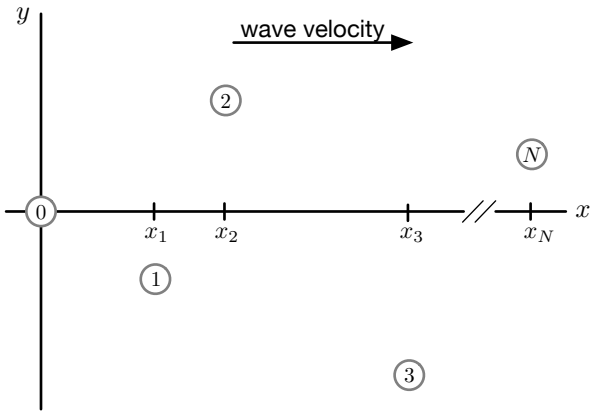

Figure 6.1: Top-down view of an N buoy WEC array. WEC motion is assumed to be in heave only [57].

Consider the N WEC array of Figure 6.1 where the devices are arranged such that their hydrodynamic coupling is negligible and they all receive the same wave forces. The vertical speed of the ith WEC is assumed to be

$$\dot{z}_i = v_i \cos(kx_i - \omega t) \tag{6.1}$$

where v_i is its amplitude, k the wave number, x_i the x component of its position vector

from the origin of the reference frame, ω is the temporal frequency and t is time. The wave number and frequency are related by the dispersion equation of Eq. 6.2

$$\omega^2 = gk \tanh(kh) \tag{6.2}$$

where g is the local gravitational acceleration and h is the water depth. Assuming that the ith WEC's control force is

$$F_{c,i} = k_{c,i} v_i \cos(kx_i - \omega t + \theta_i) \tag{6.3}$$

where $k_{c,i}$ scales and θ_i phase shifts the velocity. The ith WEC power output is

$$p_i = k_{c,i} v_i^2 \cos(kx_i - \omega t) \cos(kx_i - \omega t + \theta_i), \quad 0 \leq \theta_i \leq \frac{\pi}{2} \tag{6.4}$$

where $\theta_i = 0$ yields maximum power and $\theta_i = \frac{\pi}{2}$ results in minimum power. The control law of Eq. 6.3 captures a wide range of control strategies, including the resistive approach used in the case studies in Sections 6.2 and 6.3. Summing Eq. 6.4 over all N WECs, employing some trigonometry and defining $2A_i = k_{c,i} v_i^2$, the array power is

$$p = \sum_{i=0}^{N-1} A_i \left[\cos\left(2(kx_i - \omega t) + \theta_i\right) + \cos\theta_i\right] \tag{6.5}$$

To achieve constant power $\dot{p}$ must be zero for all time leading to the condition

$$\sum_{i=0}^{N-1} A_i \sin\left(2(\phi_i - \omega t)\right) = \cos 2\omega t \sum_{i=0}^{N-1} A_i \sin 2\phi_i - \sin 2\omega t \sum_{i=0}^{N-1} A_i \cos 2\phi_i = 0 \tag{6.6}$$

where

$$\phi_i = kx_i + \frac{1}{2}\theta_i \tag{6.7}$$

This results in two simultaneous equations, Eq. 6.8, that when satisfied, ensures the array power is constant. For a given regular wave, k or ω, and specified WEC spacing, x_i, there are $2N$ free parameters - A_i and the θ_i of Eq. 6.7.

$$\begin{aligned} \sum_{i=0}^{N-1} A_i \sin 2\phi_i &= 0 \\ \sum_{i=0}^{N-1} A_i \cos 2\phi_i &= 0 \end{aligned} \tag{6.8}$$

If the WEC spacing is fixed, then these constant power conditions are satisfied for only a set of specific wave numbers k. This may seem limiting, however, Eq. 6.7 illustrates that by adjusting the WEC control phase, θ_i, it is possible to achieve constant power for a continuous variation in k with some sacrifice of output power. Reducing an individual WECs power output by adjusting its θ_i may be justifiable since maintaining the array's constant power reduces: (1) power loss due to storage cycling, (2) storage capacity requirements and (3) losses arising from transmitting sinusoidal power from the array.

To quantify the array storage requirements, consider the case where Eq. 6.8 is not satisfied. The array's power output due to the WECs, Eq. 6.5, will be sinusoidal. A storage device can be added to the array that absorbs and contributes energy such that the net power transmitted from the array is again constant. Considering the storage device as the N^{th} "WEC" in the array, the polyphase conditions of Eq. 6.8 become

$$\begin{aligned} \sum_{i=0}^{N-1} A_i \sin 2\phi_i &= -A_N \sin 2\phi_N \\ \sum_{i=0}^{N-1} A_i \cos 2\phi_i &= -A_N \cos 2\phi_N \end{aligned} \tag{6.9}$$

The magnitude and phase of the storage power, A_N and ϕ_N, are

$$\begin{aligned}(2A_N)^2 &= \left(\sum_{i=0}^{N-1} A_i \sin 2\phi_i\right)^2 + \left(\sum_{i=0}^{N-1} A_i \cos 2\phi_i\right)^2 \\ \tan\phi_N &= \frac{\sum_{i=0}^{N-1} A_i \sin 2\phi_i}{\sum_{i=0}^{N-1} A_i \cos 2\phi_i}\end{aligned} \tag{6.10}$$

where A_N can be used to determine the storage capacity based on the expected wave frequency, array configuration, and the use of θ_i to trade-off power output for storage capacity.

As an example, consider an $N = 5$ array where the WECs have identical power output, $A_i = A$, when operating at peak capacity, $\theta_i = 0$. For a wave frequency $\omega = \omega_0 = 0.3237\,\text{rad/s}$, or $k = 0.0126\,\text{m}^{-1}$ where the depth is $h = 100\,\text{m}$, the total power is constant when $\phi_i = \{0°, 72°, 144°, 216°, 288°\}$ for $i = 0 \ldots 4$ as shown in Figure 6.2a.

Now consider the case where the wave frequency is reduced by 20%, $\omega = 0.8\omega_0$, but the WEC spacing is unchanged, resulting in a sinusoidal total power output shown in Figure 6.2c. In this example $x_i = 100i\,\text{m}$, but any appropriate spacing would suffice. The array can be brought back to constant power in two ways: (1) through storage control or (2) adjusting the control force phasing, θ_i, of Eq. 6.3. Figure 6.2c shows the storage solution using Eq. 6.10 where $A_N = 0.6215$. The required storage capacity, E, is the magnitude of the integral of the storage power, in this case $E = A_N/0.8\omega_0$.

Another approach to securing constant power is to control the phase angle θ_i. These can be found by solving a constrained optimization problem: Calculate the θ_i^* that minimize $J = \sum \theta_i$ subject to the equality constraints of Eq. 6.8 and $0 \leq \theta_i \leq \frac{\pi}{2}$. The motivation for this particular J is to keep the individual WEC output as close as possible to the maximum. It's important to note that alternative cost functions can be used that may be better from an array perspective. The results for $J = \sum \theta_i$ are shown in Figure 6.2d where $\theta_0^* = \theta_3^* = 0$ and $\theta_1^* = 52.5°$, $\theta_2^* = 11.4°$ and $\theta_4^* = 30.0°$. While constant power was achieved, the array power was reduced from 2.5 to 2.3 or about 8%. This could be an acceptable reduction depending on the availability of array storage or the loss incurred transmitting the sinusoidal power of Figure 6.2b. It's important to note that as the number of WECs in the array increases, the array power penalty decreases dramatically. For example, if 10 WECs are used, the power reduction is about 0.1% for the same 20% change in wave frequency.

Next, consider the special case where all the WEC's are identical, $A_i = A$. Without any loss of generality, the reference frame origin can be placed at the 0th WEC as shown in Figure 6.1. The constant power conditions in this situation are

$$\begin{aligned} \sum_{i=1}^{N-1} \sin 2\phi_i &= 0 \\ \sum_{i=1}^{N-1} \cos 2\phi_i &= -1 \end{aligned} \tag{6.11}$$

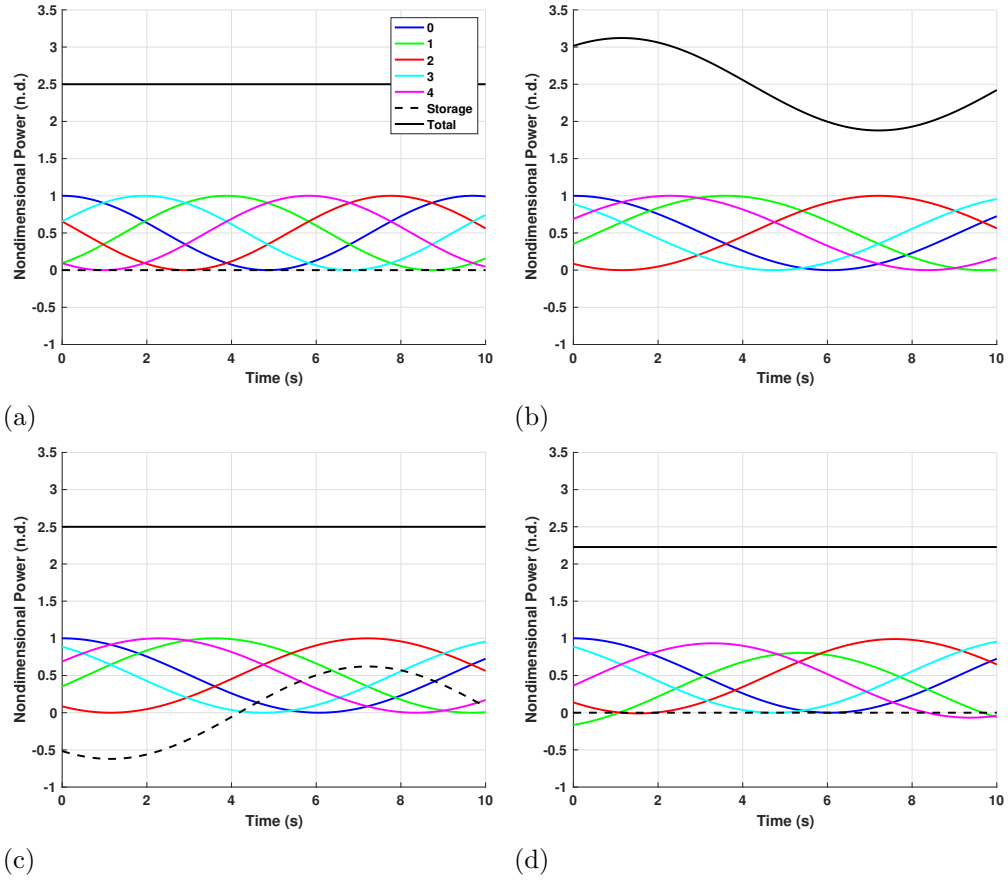

Figure 6.2: Five-WEC array example illustrating (a) constant power when the wave frequency, ω_0 satisfies the polyphase conditions, ($\omega = \omega_0$, $\theta_i = 0$, $A_N = 0$) (b) the effect on power when $\omega \neq \omega_0$ ($\omega = 0.8\omega_0$, $\theta_i = 0$, $A_N = 0$), (c) using storage to achieve constant power ($\omega = 0.8\omega_0$, $\theta_i = 0$, $A_N = 0.6215$) and (d) using θ_i to achieve constant power without storage ($\omega = 0.8\omega_0$, $\theta_i = \theta_i^*$, $A_N = 0$) [57].

For $N = 3$ the solution is $\phi_1 = 120°$ and $\phi_2 = 240°$ and for $N > 3$ there are multiple solutions. Using Eq. 6.7, the ϕ_i can be attained using a variety of spacing, x_i, and control phasing, θ_i.

Applying two additional conditions: (1) equal spacing, $x_i = Li$, where L is the distance between any two WECs and (2) peak power operation, $\theta_i = 0$, the constant power sufficient conditions can be written using closed-form set operations. To show

this, arithmetic progression expressions are substituted into Equation 6.11 as shown in Eq. 6.12.

$$\begin{aligned}\sum_{i=0}^{N-1}\sin\left(2kLi\right) &= \frac{\sin\left(NkL\right)}{\sin\left(kL\right)}\sin\left((N-1)kL\right) = 0\\ \sum_{i=0}^{N-1}\cos\left(2kLi\right) &= \frac{\sin\left(NkL\right)}{\sin\left(kL\right)}\cos\left((N-1)kL\right) = 0\end{aligned} \tag{6.12}$$

If the wave length, $\lambda = \frac{2\pi}{k}$ is known, Eq. 6.12 can be manipulated to create the sufficient conditions for the set of separation distances, $\{L\}$,

$$\{L\} = \left\{\frac{m\lambda}{2N}\right\} - \left(\left\{\frac{m\lambda}{2(N-1)}\right\} \cup \left\{\frac{m\lambda}{2}\right\}\right) \; m = 1 \ldots M \tag{6.13}$$

where the subtraction symbol is the relative compliment operator and M, R and Q are ≥ 1 and wavelength and wavenumber are related by $\lambda = \frac{2\pi}{k}$. The number of separation distances returned is M. Similarly, if the separation distance L is specified, then the sufficient condition for the set of wavelengths, $\{\lambda\}$, that yield constant power are

$$\{\lambda\} = \left\{\frac{2NL}{m}\right\} - \left(\left\{\frac{2(N-1)L}{m}\right\} \cup \left\{\frac{2L}{m}\right\}\right) \; m = 1 \ldots M \tag{6.14}$$

Figure 6.3 helps to visualize the possible spacing solutions given a wave frequency ω_0 for the five-WEC array considered earlier. In this case the wavelength was set to $\lambda_0 = 60\,\text{m}$ corresponding to $\omega_0 = 1.1036\,\text{rad/s}$ when the water depth is $h = 100\,\text{m}$. The most densely packed solution is shown with the blue circles and the most sparse solution shown with red circles. They both have the $0th$ WEC in common at the origin. The horizontal lines are the phase angles calculated earlier and the diagonal lines repeat according to the wavelength. Valid solutions must span all five phases, $\phi_i = \{0°, 72°, 144°, 216°, 288°\}$ for $i = 0 \ldots 4$, while intersecting the diagonal wavelength lines.

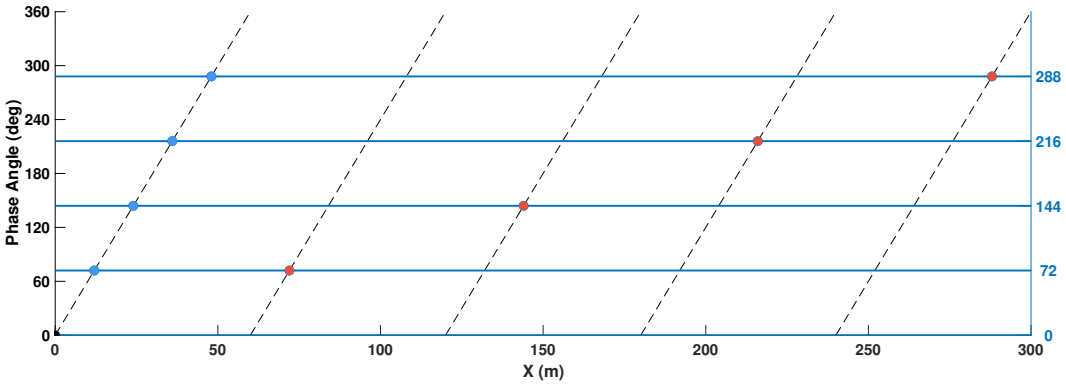

Figure 6.3: Two spacing solutions for the five-WEC array example introduced earlier. The phase, ϕ_i described by Eq. 6.8, is plotted with respect to the buoy location x_i. The 0th WEC for both solutions is at the origin shown as a black circle. A tightly packed solution is shown with blue circles while a sparsely packed solution is shown in red [57].

6.2 Simulation Case Study

While the previous development was motivated by the WEC array application, it did not consider the WEC's dynamic response. Thus, it was applicable to any set of N generators but ignored the more realistic WEC response to waves. In this section constant power conditions are explored using WEC array dynamic models. Three and six-WEC arrays were considered for the special case described above where their inter-WEC spacing, $L = 100\,\mathrm{m}$, was constant, and their power outputs were identical, $A_i = A$. The WEC array simulation included a storage controller that ensured the total power was constant regardless of the wave frequency or spacing. The simulation was executed by sweeping through a range of wave frequencies where the storage power sinusoidal amplitude was used to assess performance. Similar to the analysis above, the six-WEC array was less sensitive to variations in the conditions that yielded constant power than the three-WEC array.

The WEC array model consisted of N cylindrical buoy point absorbers each with 1.0 m radius and 1.0 m draught. It was assumed that their constant, inter-WEC spacing L was sufficiently large so there was no dynamic coupling. Furthermore, all the WECs incident waves had the same properties and so their power outputs were identical as mentioned above. The local water depth was $h = 100\,\mathrm{m}$.

The ith WEC's dynamic model was adapted from [66, 85] and is shown in Eq. 6.15 where the i subscripts are omitted for brevity.

$$(m + a_\infty)\ddot{z} = F_e + F_c + F_r + F_s \tag{6.15}$$

The added mass at the infinite frequency is denoted by a_∞, and the forces on the right are: excitation, F_e, control, F_c, radiation, F_r, and hydrostatic F_s. The expressions for each are,

$$\begin{aligned} F_e &= \int_{-\infty}^{\infty} \Big[h_{exc}(\tau)\eta(t-\tau) \Big] d\tau \\ F_c &= -k_c \dot{z} \\ F_r &= -\int_0^t h_r(t-\tau)\dot{z} d\tau \\ F_s &= -k_s z \end{aligned} \tag{6.16}$$

where h_{exc} is the excitation impulse response function, $\eta(t-\tau)$ is the wave elevation, h_r is the radiation impulse response function and k_s is the linear hydrostatic stiffness constant. The z and $\dot{z}$ correspond to the vertical WEC displacement and velocity respectively. The hydrostatic stiffness constant and other hydrodynamic coefficients were generated using the boundary element solver in the hydrodynamic analysis software WAMIT.

a) The excitation force IRF, $h_{exc}(t)$.

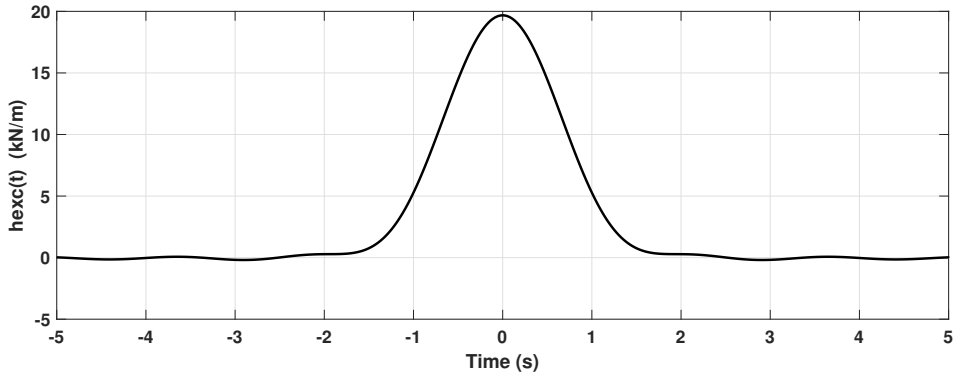

b) The radiation force IRF, $h_r(t)$.

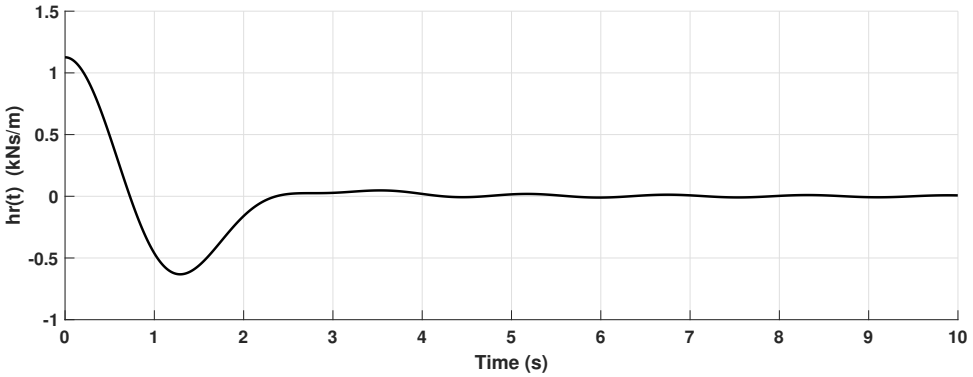

Figure 6.4: The impulse response functions experienced by each WEC. The inter-WEC spacing was $L = 100\,\text{m}$, and no significant hydrodynamic coupling could be observed for the cylindrical WECs with 1.0 m radius and 1.0 m draught [57].

The h_{exc} and h_r were computed using the Fourier-transform of the frequency-dependent excitation force and radiation damping hydrodynamic coefficients, respectively and are shown in Figure 6.4. Similarly, the added mass at infinite frequency was found to be $a_\infty = 1950.6\,kg$, and the hydrostatic stiffness was found to be $k_s = 3.1\,kN/m$. The rate feedback control law, F_c, is a subset of the family introduced earlier in Eq. 6.3. The excitation force contains the dynamic Froude-Krylov and diffraction forces. The linear assumptions require that the incoming waves have

small amplitude and steepness and that the WEC motions are also small.

The peak RMS power and energy were calculated for the last $100\,s$ of the simulations (total run time being $500\,s$) to avoid the initial transient behavior. The peak RMS power, as shown in Figure 6.5 was calculated using the storage power sinusoidal amplitude in Equation 6.10. The energy spent by the ESS was calculated by integrating the storage power over the last $100\,s$, which in this case would be $E = A_N/\omega$. Notice, in Figure 6.5, the ESS power increases with an increase in wave frequency while the ESS energy is less sensitive to increase in wave frequency because as the power increases, so does the wave frequency. Therefore, the ESS specifications should be informed by both the power and energy requirements.

The ith WEC's power output is given by Eq. 6.4, with $\theta_i = 0$, and the total WEC power by Eq. 6.5. When the array conditions are such that constant power is achieved, the total power will be $p = \frac{1}{2}NA$. This value was used as the reference for the storage controller, which simply added the necessary power to make up the difference between the reference and the instantaneous, total WEC power output.

6.3 Results

For both the 3-WEC and 6-WEC arrays, the simulation was used to assess the storage needed to produce constant power with inter-WEC spacing held at $L = 100\,\mathrm{m}$. The incident wave amplitude was 0.25 m and the wave frequency was stepped for a total of 1000 frequencies between 0.75 to 1.75 rad/s . At each frequency, the simulation was allowed to run for 500 seconds. The simulated storage power for both cases are shown in Figure 6.5. The constant power frequencies are shown as red dots as computed by the $\{\lambda\}$ set of Eq. 6.14. As expected, these match well with the minima of the simulated storage power.

One of the primary differences between the three and six-WEC arrays is their sensitivity to variations in wave frequency. If the objective is to reduce the amount of oscillation in the array power, the least desirable situation is when the wave frequency corresponds to a local maximum in the storage plots. Selecting a spacing that allows that avoids maxima for the expected wave frequency variation is more easily achieved for the six-WEC array. This storage "flatness" increases dramatically with N.

a) Three-WEC Array

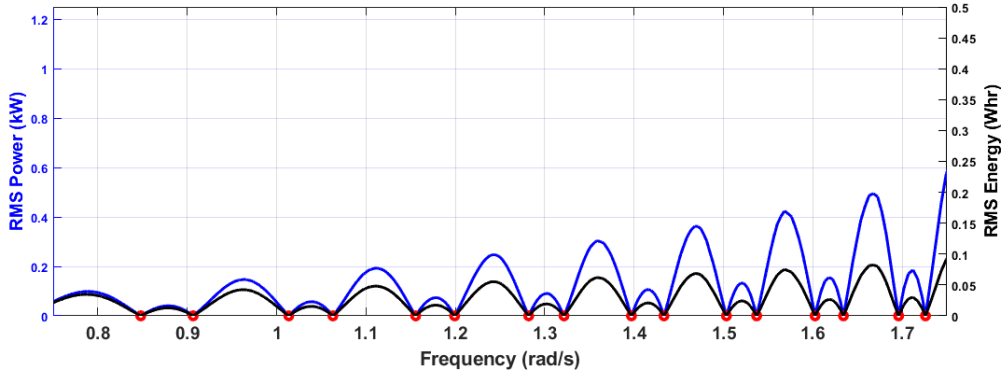

b) Six-WEC Array

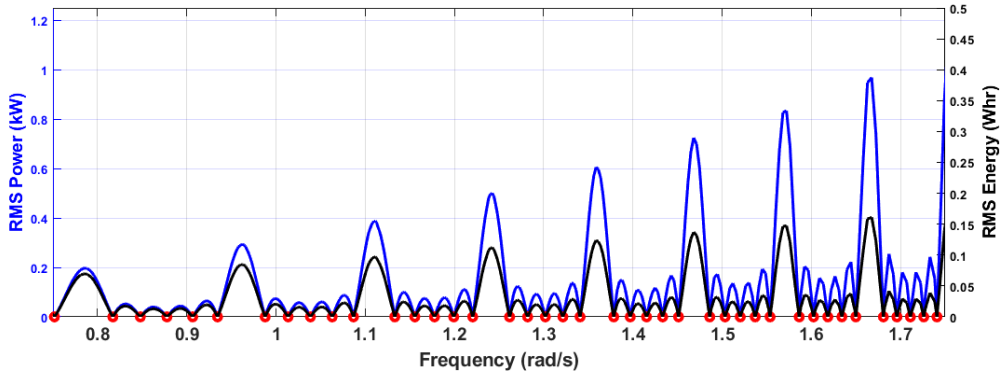

Figure 6.5: Storage power and energy, as a function of wave frequency (0.75 rad/s - 1.75 rad/s), required to ensure that the WEC array power was constant for both three and six-WEC arrays. The inter-WEC spacing was $L = 100\,\text{m}$. The storage energy requirements are less sensitive to increases in wave frequency when compared to storage power [57].

6.4 Summary

Energy generated by a single wave energy converter needs modulation, but a network of WECs with staggered phases can complement each other to result in constant power that can be integrated to a marine energy grid. Increasing the number of WECs in a WEC array reduces the fluctuations in the aggregate power produced by

the WEC array. If the WECs constituting the WEC array produce polyphase power, the fluctuations in the net power produced by the WEC array can be mitigated. This work shows that the phase of the ocean waves can inform the layout of a WEC array to produce polyphase power. The simulation model also demonstrates that the control effort to maintain constant power requirements can be significantly reduced if a WEC array produces polyphase power. Additionally, the constant total power is less susceptible to transmission losses for the undersea transmission lines. Finally, polyphase power generation capabilities can significantly reduce the size of the ESS needed for the power management of a MEG.

This work can be extended to irregular wave conditions with different wave periods and directions. The majority of the energy in the incoming wave is concentrated in a narrow bandwidth of wave periods. For instance for Pierson-Moscowitz spectrum most of the energy is concentrated between the wave periods of $6-10\ s$. Linear theory can be used to describe most irregular wave spectra using 5 to 10 significant wave periods and their corresponding wave heights. The conditions developed in this work used the summation of sinusoidal series to identify conditions needed for generating polyphase. These conditions can be extended to irregular waves by including the significant wave periods and wave heights in the summation of the sinusoidal series used to develop such conditions. Additionally, asymmetric hull design of the WEC can further assist in achieving polyphase condition. Ultimately, the power produced by a deployed WEC array is bound to have some fluctuations. However, this work

tries demonstrate that the phase of the waves received at individual WECs in an array should be a consideration in control design for power-management of WEC array based Marine Electric Grids.

Chapter 7

Conclusions and Future Work

This work analyzed the physical phenomena that affect WEC arrays, addressed the challenges in their numerical modeling, and proposed grid integration strategies. This work developed a metric to evaluate the theoretical limit of the energy available to a WEC array. This was followed by the development of a radiation force estimation algorithm to ensure the numerical stability of time-domain models. The algorithm was verified for WEC arrays with different packing densities. The algorithm was found to have a threshold for estimating passive models for the WEC array with respect to WEC array packing density. Lack of passivity does not necessarily mean instability, but the model is no longer guaranteed to be stable for all operating conditions, especially around the relevant, resonant frequencies. Overall, the estimated models simulated WEC array motion characteristics within 5 % even for the densest WEC

array simulated. The numerical WEC array models also exhibited the *trapping effect*, such that the available wave energy flux increased with an increase in hydrodynamic couplings. This corroborated the theoretical assumptions used to develop the WEC array performance metric. The oscillatory nature of wave energy resources challenges the establishment of Marine Energy Grids as they require a constant power source. The grid integration issues introduced by the oscillatory power profile of renewable energy sources are mitigated by Energy Storage Systems and can add high logistical and operational costs. This work recommended WEC array design considerations that could markedly reduce the Energy Storage System effort. This work used plane-progressive waves that oscillate in the vertical plane. The analyses shown here could be extended to circular waves and irregular waves. Additionally, a normalized version of the system identification algorithm could further extend the applicability of the proposed algorithm.

This work showed that, in a WEC array,

1. The hydrodynamic couplings can increase the energy that can be extracted,

2. The radiation damping hydrodynamic coefficients can be used as an indicator of hydrodynamic coupling and the theoretical limit of the energy that can be extracted,

3. The Linear Time-Invariant system identification of radiation force should enforce passivity to ensure the numerical stability of time-domain models,

4. Producing constant power is desirable for grid integration,

5. Layout design can help harmonize the power produced by the WEC array such that it produces constant power.

Multi-body dynamics analysis of WEC arrays remains challenging, especially when external mechanisms such as support structures and mooring forces are introduced. The current state of the art in multi-body dynamics is constrained due to the dense inertia matrices involved in WEC array multi-body dynamics due to the added-mass terms. Tools to solve such problems can be a significant contribution to WEC array research.

Lastly, access to WEC modeling tools remains a significant hurdle for the WEC research community and the emerging industry. The development of open-source tools can significantly increase the critical mass of people innovating, designing, testing WECs. The time-domain models discussed here can be extended to open-source code packages in the future.

References

[1] Alves, M., Vincente, M., Sarmento, A., and Guerinel, M. Implementation and Verification of a Time Domain Model to Simulate the Dynamics of OWCs.

[2] Ancellin, M., and Dias, F. Capytaine: a Python-based linear potential flow solver. *Journal of Open Source Software 4*, 36 (Apr. 2019), 1341. Number: 36.

[3] Anderlini, E., Husain, S., Parker, G. G., Abusara, M., and Thomas, G. Towards Real-Time Reinforcement Learning Control of a Wave Energy Converter. *Journal of Marine Science and Engineering 8*, 11 (Oct. 2020), 845.

[4] Babarit, A., and Delhommeau, G. Theoretical and numerical aspects of the open source bem solver nemoh. In *11th European wave and tidal energy conference (EWTEC2015)* (2015).

[5] Balitsky, P., Bacelli, G., and Ringwood, J. V. Control-influenced layout optimization of arrays of wave energy converters. In *International Conference on Offshore Mechanics and Arctic Engineering* (2014), vol. 45547, American Society of Mechanical Engineers, p. V09BT09A022.

[6] Barakat, R., and Parshall, E. Numerical evaluation of the zero-order Hankel transform using Filon quadrature philosophy. *Applied Mathematics Letters 9*, 5 (Sept. 1996), 21–26. Number: 5.

[7] Bechhoefer, J. Kramers–kronig, bode, and the meaning of zero. *American Journal of Physics 79*, 10 (2011), 1053–1059.

[8] Brando, G., Dannier, A., Pizzo, A. D., Noia, L. P. D., and Pisani, C. Grid connection of wave energy converter in heaving mode operation by supercapacitor storage technology. *IET Renewable Power Generation 10*, 1 (Jan. 2016), 88–97. Number: 1.

[9] Butcher, J. *Numerical Methods for Ordinary Differential Equations, 3rd Edition | Wiley*, 3 ed. 2016.

[10] Cauchy, A. L. *Théorie de la propagation des ondes à la surface d'un fluide pesant d'une profondeur indéfinie.* Paris, France, 1815.

[11] Chang, G., Ruehl, K., Jones, C. A., Roberts, J., and Chartrand, C. Numerical modeling of the effects of wave energy converter characteristics on nearshore wave conditions. *Renewable Energy 89* (Apr. 2016), 636–648.

[12] Child, B., and Venugopal, V. Interaction of waves with an array of floating wave energy devcies. In *Proc. 7th European Wave and Tidal Energy Conference* (2007).

[13] Clarke, J. A., Connor, G., Grant, A. D., and Johnstone, C. M. Regulating the output characteristics of tidal current power stations to facilitate better base load matching over the lunar cycle. *Renewable Energy 31*, 2 (Feb. 2006), 173–180. Number: 2.

[14] Clément, A., McCullen, P., Falcão, A., Fiorentino, A., Gardner, F., Hammarlund, K., Lemonis, G., Lewis, T., Nielsen, K., Petroncini, S., Pontes, M. T., Schild, P., Sjöström, B.-O., Sørensen, H. C., and Thorpe, T. Wave energy in Europe: current status and perspectives. *Renewable and Sustainable Energy Reviews 6*, 5 (Oct. 2002), 405–431.

[15] Coe, R. G., Bacelli, G., Wilson, D. G., and Patterson, D. C. Advanced WEC Dynamics & Controls FY16 Testing Report. Tech. Rep. SAND2016-10094, 1330189, Oct. 2016. Issue: SAND2016-10094, 1330189.

[16] Cook, M. D., Parker, G. G., Robinett, R. D., and Weaver, W. W. Decentralized Mode-Adaptive Guidance and Control for DC Microgrid. *IEEE Transactions on Power Delivery 32*, 1 (Feb. 2017), 263–271. Number: 1.

[17] Count, B. M. On the Dynamics of Wave-Power Devices. *Proceedings of the Royal Society of London. Series A, Mathematical and Physical Sciences 363*, 1715 (1978), 559–579.

[18] Count, B. M. Power/energy: Exploiting wave power: To realize the promise, engineers must deal with unique power-transfer modes, erratic seas, and unfavorable economics. *IEEE Spectrum 16*, 9 (1979), 42–49.

[19] Craik, A. D. The Origins of Water Wave Theory. *Annual Review of Fluid Mechanics 36*, 1 (2004), 1–28. _eprint: https://doi.org/10.1146/annurev.fluid.36.050802.122118.

[20] Cruz, J. M. B. P., and Salter, S. H. Numerical and experimental modelling of a modified version of the Edinburgh Duck wave energy device. *Proceedings of the Institution of Mechanical Engineers, Part M: Journal of Engineering for the Maritime Environment 220*, 3 (Sept. 2006), 129–147.

[21] De Silva, C. W. *Vibration: fundamentals and practice*. CRC press, 2006.

[22] Delhommeau, G. *Les problèmes de diffraction-radiation et de résistance de vagues: étude théorique et résolution numérique par la méthode des singularités*. PhD Thesis, Nantes, 1987.

[23] Delhommeau, G. Amélioration des performances des codes de calcul de diffraction-radiation au premier ordre. *Proceedings of the 2èmes Journées de l'Hydrodynamique, Nantes, France* (1989), 13–15.

[24] Dominguez, V., Graham, I. G., and Smyshlyaev, V. P. Stability and error estimates for Filon-Clenshaw-Curtis rules for highly oscillatory integrals. *IMA Journal of Numerical Analysis 31*, 4 (Oct. 2011), 1253–1280. Number: 4.

[25] Douce, J., Widanage, W. D., and Godfrey, K. R. Evaluation of the relationship between gain and phase using extrapolation techniques. *IET Control Theory & Applications 1*, 4 (2007), 1122–1130.

[26] Duarte, T., Alves, M., Jonkman, J., and Sarmento, A. State-Space Realization of the Wave-Radiation Force Within FAST. In *Volume 8: Ocean Renewable Energy* (Nantes, France, June 2013), American Society of Mechanical Engineers, p. V008T09A021.

[27] Edition, F., Journée, J., and Massie, W. Offshore hydromechanics, 2001.

[28] Environment. Microplastic permeates Mariana Trench and other deep sea points.

[29] Evans, D. V. Power From Water Waves. *Annual Review of Fluid Mechanics 13*, 1 (Jan. 1981), 157–187.

[30] Faedo, N., Peña-Sanchez, Y., and Ringwood, J. V. Passivity preserving moment-based finite-order hydrodynamic model identification for wave energy applications. 9.

[31] Faedo, N., Peña-Sanchez, Y., and Ringwood, J. V. Finite-order hydrodynamic model determination for wave energy applications using moment-matching. *Ocean Engineering 163* (Sept. 2018), 251–263.

[32] Faedo, N., Peña-Sanchez, Y., and Ringwood, J. V. Moment-matching-based identification of wave energy converters: the iswec device**this material is based upon works supported by science foundation ireland under grant no. 13/ia/1886. *IFAC-PapersOnLine 51*, 29 (Jan. 2018), 189–194. Number: 29.

[33] Faedo, N., Peña-Sanchez, Y., and Ringwood, J. V. Parameterisation of radiation forces for a multiple degree-of-freedom wave energy converter using moment-matching. International Society of Offshore and Polar Engineers.

[34] Faedo, N., and Ringwood, J. V. Moment-based constrained optimal control of wave energy converters: flap-type device**this material is based upon works supported by science foundation ireland under grant no. 13/ia/1886. *IFAC-PapersOnLine 51*, 29 (Jan. 2018), 50–55. Number: 29.

[35] Faedo, N., Scarciotti, G., Astolfi, A., and Ringwood, J. V. Energy-maximising control of wave energy converters using a moment-domain representation. *Control Engineering Practice 81* (Dec. 2018), 85–96.

[36] Faedo, N., Scarciotti, G., Astolfi, A., and Ringwood, J. V. Moment-based constrained optimal control of an array of wave energy converters. In

2019 American Control Conference (ACC) (Philadelphia, PA, USA, July 2019), IEEE, pp. 4797–4802.

[37] Falnes, J. *Ocean Waves and Oscillating Systems: Linear Interactions Including Wave-Energy Extraction*. Cambridge University Press, Cambridge, 2002.

[38] Falnes, J., and Budal, K. Wave-power absorption by parallel rows of interacting oscillating bodies. *Applied Ocean Research 4*, 4 (Oct. 1982), 194–207.

[39] Filon, L. N. G. iii. —on a quadrature formula for trigonometric integrals. *Proceedings of the Royal Society of Edinburgh 49* (1930), 38–47.

[40] Folley, M. *Numerical modelling of wave energy converters state-of-the-art techniques for single devices and arrays*. Academic Press is an imprint of Elsevier, London, UK, 2016.

[41] Folley, M., Babarit, A., Child, B., Forehand, D., O'Boyle, L., Silverthorne, K., Spinneken, J., Stratigaki, V., and Troch, P. A Review of Numerical Modelling of Wave Energy Converter Arrays. In *Volume 7: Ocean Space Utilization; Ocean Renewable Energy* (Rio de Janeiro, Brazil, July 2012), American Society of Mechanical Engineers, pp. 535–545.

[42] Forehand, D. I. M., Kiprakis, A. E., Nambiar, A. J., and Wallace, A. R. A Fully Coupled Wave-to-Wire Model of an Array of Wave Energy

Converters. *IEEE Transactions on Sustainable Energy 7*, 1 (Jan. 2016), 118–128. Number: 1 Publisher: Institute of Electrical and Electronics Engineers Inc.

[43] Fossen, T. I. Handbook of Marine Craft Hydrodynamics and Motion Control. 582.

[44] Fourier, J. Mémoire sur la propagation de la chaleur dans les corps solides, présenté le 21 Décembre 1807 à l'Institut national—Nouveau Bulletin des sciences par la Société philomatique de Paris. I. In *Paris: First European Conference on Signal Analysis and Prediction* (1807), pp. 17–21.

[45] Garnaud, X. *Wave Energy Extraction from buoys*. PhD thesis, Dec. 2009.

[46] Garnaud, X., and Mei, C. C. Wave-power extraction by a compact array of buoys. *Journal of Fluid Mechanics 635* (Sept. 2009), 389–413.

[47] Garnaud, X., and Mei, C. C. Bragg scattering and wave-power extraction by an array of small buoys. *Proceedings of the Royal Society A: Mathematical, Physical and Engineering Sciences 466*, 2113 (2010), 79–106. Publisher: The Royal Society Publishing.

[48] Garrison, C. J. Interaction of oblique waves with an infinite cylinder. *Applied Ocean Research 6*, 1 (Jan. 1984), 4–15.

[49] Giorgi, S., and Ringwood, J. V. Can Tidal Current Energy Provide Base Load? *Energies 6*, 6 (June 2013), 2840–2858. Number: 6 Publisher: Multidisciplinary Digital Publishing Institute.

[50] Gourlay, T. Comparison of WAMIT v7.3 with Marin model tests for side-by-side LNG carriers in waves. 11.

[51] Greenhow, M., Rosen, J. H., and Reed, M. Control strategies for the Clam Wave Energy Device. *Applied Ocean Research 6*, 4 (Oct. 1984), 197–206.

[52] Grice, J. R., Taylor, P. H., and Eatock Taylor, R. Near-trapping effects for multi-column structures in deterministic and random waves. *Ocean Engineering 58* (Jan. 2013), 60–77.

[53] Göteman, M., McNatt, C., Giassi, M., Engström, J., and Isberg, J. Arrays of point-absorbing wave energy converters in short-crested irregular waves. *Energies 11*, 4 (2018), 964. Publisher: Multidisciplinary Digital Publishing Institute.

[54] Haren, P., and Mei, C. C. An array of Hagen-Cockerell wave power absorbers in head seas. *Applied ocean research 4*, 1 (1982), 51–56. Publisher: Elsevier.

[55] Havelock, T. H. Waves due to a floating sphere making periodic heaving oscillations. *Proceedings of the Royal Society of London. Series A. Mathematical and Physical Sciences 231*, 1184 (July 1955), 1–7.

[56] Husain, S., and Parker, G. G. Effects of Hydrodynamic Coupling on Energy Extraction Performance of Wave Energy Converter Arrays. In *OCEANS 2018 MTS/IEEE Charleston* (2018), pp. 1–8.

[57] Husain, S., Parker, G. G., and Weaver, W. W. Storage minimization of marine energy grids using polyphase power. *Journal of Marine Science and Engineering 10*, 2 (2022).

[58] Håvie, T. Remarks on an expansion for integrals of rapidly oscillating functions. *BIT 13*, 1 (Mar. 1973), 16–29. Number: 1.

[59] Jafaryeganeh, H., Rodrigues, J. M., and Guedes Soares, C. Influence of mesh refinement on the motions predicted by a panel code. Oct. 2014, pp. 1029–1038.

[60] Jamet, S. NEMOH-Presentation, May 2021. Publisher: Sandrine Jamet.

[61] Kelvin, W. *Popular Lectures and Addresses*. No. v. 1 in Nature series. Macmillan and Company, 1891.

[62] Kelvin, W. T. B., and Tait, P. G. *Treatise on Natural Philosophy*. Clarendon Press, 1867. Google-Books-ID: 6odDAQAAMAAJ.

[63] Khalil, H. K. *Nonlinear Systems*, 3 ed. Prentice Hall, 2014.

[64] Kilcher, L., Fogarty, M., and Lawson, M. Marine Energy in the United States: An Overview of Opportunities. Tech. Rep. NREL/TP-5700-78773, 1766861, MainId:32690, Feb. 2021.

[65] Korde, U. Control system applications in wave energy conversion. In *OCEANS 2000 MTS/IEEE Conference and Exhibition. Conference Proceedings (Cat. No.00CH37158)* (Providence, RI, USA, 2000), vol. 3, IEEE, pp. 1817–1824.

[66] Korde, U. A., and Ringwood, J. *Hydrodynamic Control of Wave Energy Devices*. Cambridge University Press, Sept. 2016.

[67] Kottenstette, N., and Antsaklis, P. J. Relationships between positive real, passive dissipative, & positive systems. In *Proceedings of the 2010 American Control Conference* (Baltimore, MD, June 2010), IEEE, pp. 409–416.

[68] Kottenstette, N., McCourt, M. J., Xia, M., Gupta, V., and Antsaklis, P. J. On relationships among passivity, positive realness, and dissipativity in linear systems. *Automatica 50*, 4 (Apr. 2014), 1003–1016.

[69] Kristiansen, E., Hjulstad, and Egeland, O. State-space representation of radiation forces in time-domain vessel models. *Ocean Engineering 32*, 17 (2005), 2195–2216. Number: 17.

[70] Lamb, H. *Hydrodynamics*. Cambridge : University Press, 1916.

[71] Le Méhauté, B. *An Introduction to Hydrodynamics and Water Waves*. Springer Study Edition. Springer Berlin Heidelberg, 2013.

[72] Leishman, J. M., and Scobie, G. The Development Of Wave Power: A Techno-Economic Study. Report, Department of Industry: National Engineering Laboratory, UK, 1976. Accepted: 2020-10-08T12:39:01Z.

[73] Lucas, J., Salter, S., Cruz, J., Taylor, J., and Bryden, I. Performance optimisation of a modified Duck through optimal mass distribution. 10.

[74] Lucas, J. A. A. The dynamics of a horizontal cylinder oscillating as a wave energy converter about an off-centred axis. 261.

[75] Mavrakos, S., and McIver, P. Comparison of methods for computing hydrodynamic characteristics of arrays of wave power devices. *Applied Ocean Research 19*, 5-6 (1997), 283–291. Publisher: Elsevier.

[76] McCormick, M. E. Analysis of a Wave Energy Conversion Buoy. *Journal of Hydronautics 8*, 3 (1974), 77–82. _eprint: https://doi.org/10.2514/3.62983.

[77] McGuinness, J. P. L., and Thomas, G. Hydrodynamic optimisation of small arrays of heaving point absorbers. *Journal of Ocean Engineering and Marine Energy 2*, 4 (Nov. 2016), 439–457.

[78] McNeel, R., et al. Rhinoceros 3d, version 6.0. *Robert McNeel & Associates, Seattle, WA* (2010).

[79] Mei, C. C. Hydrodynamic principles of wave power extraction. *Philosophical Transactions of the Royal Society A: Mathematical, Physical and Engineering Sciences 370*, 1959 (Jan. 2012), 208–234.

[80] Mukherjee, B. N., and Maiti, S. S. On some properties of positive definite toeplitz matrices and their possible applications. *Linear Algebra and its Applications 102* (Apr. 1988), 211–240.

[81] Mynett, A. E., Serman, D. D., and Mei, C. C. Characteristics of Saiter's cam for extracting energy from ocean waves. 8.

[82] Nebel, P. Maximizing the efficiency of wave-energy plant using complex-conjugate control. *Proceedings of the Institution of Mechanical Engineers, Part I: Journal of Systems and Control Engineering 206*, 4 (1992), 225–236. Publisher: SAGE Publications Sage UK: London, England.

[83] Nebel, P. Synthesis of optimal control of a wave energy converter. Accepted: 2016-01-19T16:30:20Z Publisher: The University of Edinburgh.

[84] Newman, J. The Theory of Ship Motions. In *Advances in Applied Mechanics*, vol. 18. Elsevier, 1979, pp. 221–283.

[85] Newman, J. N. *Marine hydrodynamics*. MIT Press, Cambridge, Mass, 1977, 2018.

[86] Ogilvie, T. F. Recent Progress Toward the Understanding and Prediction of Ship Motions. *5th ONR Symp. on Naval Hydrodynamics* (1964).

[87] Parwal, A., Fregelius, M., Temiz, I., Göteman, M., Oliveira, J. G. d., Boström, C., and Leijon, M. Energy management for a grid-connected wave energy park through a hybrid energy storage system. *Applied Energy 231* (Dec. 2018), 399–411.

[88] Pena-Sanchez, Y., Faedo, N., and Ringwood, J. V. Moment-based parametric identification of arrays of wave energy converters* this material is based upon works supported by science foundation ireland under grant no. 13/ia/1886. In *2019 American Control Conference (ACC)* (Philadelphia, PA, USA, July 2019), IEEE, pp. 4785–4790.

[89] Penalba, M., Kelly, T., and Ringwood, J. Using NEMOH for Modelling Wave Energy Converters: A Comparative Study with WAMIT.

[90] Peng, X., Chen, M., Chen, S., Dasgupta, S., Xu, H., Ta, K., Du, M., Li, J., Guo, Z., and Bai, S. Microplastics contaminate the deepest part of the world's ocean. *Geochemical Perspectives Letters* (Nov. 2018), 1–5.

[91] Perez, T., and Fossen, T. I. Time- vs. Frequency-domain Identification of Parametric Radiation Force Models for Marine Structures at Zero Speed. *Modeling, Identification and Control: A Norwegian Research Bulletin 29*, 1 (2008), 1–19. Number: 1.

[92] Perez, T., and Fossen, T. I. A Matlab Toolbox for Parametric Identification of Radiation-Force Models of Ships and Offshore Structures. *Modeling, Identification and Control 30*, 1 (Jan. 2009), 1–15. Number: 1 Publisher: Norwegian Society of Automatic Control.

[93] Perez, T., and Fossen, T. I. Practical aspects of frequency-domain identification of dynamic models of marine structures from hydrodynamic data. *Ocean Engineering 38*, 2-3 (Feb. 2011), 426–435. Number: 2-3.

[94] Peña-Sanchez, Y., Faedo, N., and Ringwood, J. V. Hydrodynamic model fitting for wave energy applications using moment-matching: a case study. International Society of Offshore and Polar Engineers.

[95] Pidduck, F. B. The Wave-Problem of Cauchy and Poisson for Finite Depth and Slightly Compressible Fluid. *Proceedings of the Royal Society of London. Series A, Containing Papers of a Mathematical and Physical Character 86*, 588 (1912), 396–405. Publisher: The Royal Society.

[96] Pizer, D. Numerical Modelling of Wave Energy Absorbers.

[97] Preziuso, D. C., O'Neil, R. S., Alam, M. J. E., Bhatnagar, D., Bhattacharya, S. O., Ganguli, S., Yu, Y.-H., and Stark, G. Understanding the Grid Value Proposition of Marine Energy: A Literature Review. Tech. Rep. PNNL-28839, Pacific Northwest National Lab. (PNNL), Richland, WA (United States), July 2019. Issue: PNNL-28839.

[98] Retzler, C.-H. Long spine mooring. Tech. rep., The University of Edinburgh, 1986.

[99] Retzler, C.-H. Dynamics of a long flexible horizontal circular cylinder in water waves.

[100] Ringwood, J. V., Bacelli, G., and Fusco, F. Control, forecasting and optimisation for wave energy conversion. *IFAC Proceedings Volumes 47*, 3 (2014), 7678–7689. Publisher: Elsevier.

[101] Ross, D. *Energy from the Waves*. Elsevier, 2012.

[102] Ruehl, K., Ogden, D., Yu, Y.-H., Keester, A., Tom, N., Forbush, D., and Leon, J. WEC-Sim v4.4, Oct. 2021.

[103] Salter, S. Wave energy: Nostalgic Ramblings, future hopes and heretical suggestions. *Journal of Ocean Engineering and Marine Energy 2*, 4 (Nov. 2016), 399–428.

[104] Schwab, K. *The Fourth Industrial Revolution*, illustrated edition ed. Currency, New York, 2017.

[105] Seahaven Maritime Academy, UK. Unexplored Oceans - What Might We Find?

[106] Serman, D. D., and Mei, C. C. Note on Salter's energy absorber in random waves. *Ocean Engineering 7*, 4 (Jan. 1980), 477–490.

[107] Shi, F., Kirby, J. T., Harris, J. C., Geiman, J. D., and Grilli, S. T. A high-order adaptive time-stepping TVD solver for Boussinesq modeling of breaking waves and coastal inundation. *Ocean Modelling 43-44* (Jan. 2012), 36–51.

[108] Siddorn, P., and Eatock Taylor, R. Diffraction and independent radiation by an array of floating cylinders. *Ocean Engineering 35*, 13 (Sept. 2008), 1289–1303. Number: 13.

[109] Sjolte, J., Tjensvoll, G., and Molinas, M. Power Collection from Wave Energy Farms. *Applied Sciences 3*, 2 (June 2013), 420–436. Number: 2 Publisher: Multidisciplinary Digital Publishing Institute.

[110] Skyner, D. J. Solo duck linear analysis. Tech. rep., The University of Edinburgh, 1987.

[111] Slotine, J.-J. E., Slotine, J.-J. E., and Li, W. *Applied Nonlinear Control*. Prentice Hall, 1991. Google-Books-ID: cwpRAAAAMAAJ.

[112] Stefek, J., Bain, D., Yu, Y.-H., Jenne, D., and Stark, G. Analysis on the Influence of an Energy Storage System and its Impact to the Grid for a Wave Energy Converter. American Society of Mechanical Engineers Digital Collection.

[113] Stokes, G. G., Larmor, J., and Rayleigh, J. W. S. *Mathematical and physical papers*. Cambridge : University Press, 1880.

[114] Stokes, G. G., and Thomson, W. *The Correspondence Between Sir George Gabriel Stokes and Sir William Thomson, Baron Kelvin of Largs*. Cambridge University Press, Nov. 1990. Google-Books-ID: YrjkOEdC83gC.

[115] Taghipour, R., Perez, T., and Moan, T. Hybrid frequency–time domain models for dynamic response analysis of marine structures. *Ocean Engineering 35*, 7 (May 2008), 685–705. Number: 7.

[116] Taylor, J. R. M., Rea, M., and Rogers, D. J. The Edinburgh curved tank. 8.

[117] Thomas, G., and Evans, D. Arrays of three-dimensional wave-energy absorbers. *Journal of Fluid Mechanics 108* (1981), 67–88. Publisher: Cambridge University Press.

[118] Ticona Rollano, F., Tran, T. T., Yu, Y.-H., García-Medina, G., and Yang, Z. Influence of Time and Frequency Domain Wave Forcing on the Power Estimation of a Wave Energy Converter Array. *Journal of Marine Science and Engineering 8*, 3 (Mar. 2020), 171. Number: 3 Publisher: Multidisciplinary Digital Publishing Institute.

[119] Trinklein, E. H., Parker, G. G., Robinett, R. D., and Weaver, W. W. Toward Online Optimal Power Flow of a Networked DC Microgrid System. *IEEE Journal of Emerging and Selected Topics in Power Electronics 5*, 3 (Sept. 2017), 949–959. Number: 3.

[120] Troch, P., Stratigaki, V., Stallard, T., Forehand, D., Folley, M., Kofoed, J. P., Benoit, M., Babarit, A., Vantorre, M., and Kirkegaard, J. An overview of the WECwakes project: Physical modelling of an array of 25 wave energy converters. In *Proceedings of the 3rd IAHR Europe Congress, Porto, Portugal* (2014), vol. 16.

[121] UNESCO World Heritage Centre. Marianas Trench Marine National Monument.

[122] Unneland, K. Identification and Order Reduction of Radiation Force Models of Marine Structures. Publisher: Fakultet for informasjonsteknologi, matematikk og elektroteknikk.

[123] Unneland, K., Perez, T., and Egeland, O. MIMO and SISO identification of radiation force terms for models of marine structures in waves. *IFAC Proceedings Volumes 40*, 17 (2007), 235–242. Number: 17.

[124] US Department of Commerce, National Oceanic and Atmospheric Administration. Plastic in Mariana Trench.

[125] US Department of Commerce, National Oceanic and Atmospheric Administration. NDBC Moored Buoy Program, May 2021.

[126] US Department of Commerce, National Oceanic and Atmospheric Administration. Ocean Pollution, Sept. 2021.

[127] US Department of Commerce, National Oceanic and Atmospheric Administration. What percentage of the American population lives near the coast?, Apr. 2021.

[128] US Department of Commerce, National Oceanic and Atmospheric Administration, Fisheries. Marianas Trench Marine National Monument | NOAA Fisheries, Sept. 2021. Archive Location: Pacific Islands.

[129] US Department of Energy. Powering the Blue Economy, May 2021.

[130] US Fish and Wildlife Service. Mariana Trench Marine National Monument.

[131] VDI - nachrichten. Industrie 4.0: Mit dem Internet der Dinge auf dem Weg zur 4. industriellen Revolution - vdi-nachrichten.com, Mar. 2013.

[132] Walker, D. A., and Taylor, R. E. Wave diffraction from linear arrays of cylinders. *Ocean Engineering 32*, 17-18 (2005), 2053–2078. Publisher: Elsevier.

[133] Wamit, Inc. The State of the Art in Wave Interaction Analysis, May 2021.

[134] Weaver, W. W., Robinett, R. D., Parker, G. G., and Wilson, D. G. Distributed control and energy storage requirements of networked Dc microgrids. *Control Engineering Practice 44* (Nov. 2015), 10–19.

[135] WEC, C. CorPower Wave Energy Converter.

[136] Wehausen, J. V. The Motion of Floating Bodies. *Annual Review of Fluid Mechanics 3*, 1 (1971), 237–268. Number: 1 _eprint: https://doi.org/10.1146/annurev.fl.03.010171.001321.

[137] Whittaker, T., and Folley, M. Optimisation of wave power devices towards economic wave power systems. In *World Renewable Energy Conference* (2005).

[138] Wolgamot, H. A., Eatock Taylor, R., and Taylor, P. H. Radiation, trapping and near-trapping in arrays of floating truncated cylinders. *Journal of Engineering Mathematics 91*, 1 (Apr. 2015), 17–35. Number: 1.

[139] Wolgamot, H. A., Eatock Taylor, R., and Taylor, P. H. Effects of second-order hydrodynamics on the efficiency of a wave energy array. *International Journal of Marine Energy 15* (Sept. 2016), 85–99.

[140] Yemm, R., Pizer, D., Retzler, C., and Henderson, R. Pelamis: experience from concept to connection. *Philosophical Transactions of the Royal Society A: Mathematical, Physical and Engineering Sciences 370*, 1959 (Jan. 2012), 365–380.

[141] Yu, Y.-H., Tom, N., and Jenne, D. Numerical Analysis on Hydraulic Power Take-Off for Wave Energy Converter and Power Smoothing Methods. American Society of Mechanical Engineers Digital Collection.

[142] Yu, Z., and Falnes, J. State-space modelling of a vertical cylinder in heave. *Applied Ocean Research 17*, 5 (Oct. 1995), 265–275. Number: 5.

[143] Zhou, X., Abdelkhalik, O., and Weaver, W. Power Take-Off and Energy Storage System Static Modeling and Sizing for Direct Drive Wave Energy Converter to Support Ocean Sensing Applications. *Journal of Marine Science and Engineering 8*, 7 (July 2020), 513. Number: 7 Publisher: Multidisciplinary Digital Publishing Institute.

Appendix A

Frequency Domain Modeling of Salter Duck Arrays

Consider a wave energy converter in terminator configuration, i.e., the axis of the device is coplanar with the water surface and facing the incident waves. The axis is located at the hub of the central axis, and the incoming waves cause oscillations about it. The geometry is ellipsoid such that the attacking circular section (section facing incoming waves) has a much lower radius than the non-attacking rear circular section. The axis is located near the non-attacking section. Such a device was first investigated by Salter et al at the University of Edinburgh [103]. Therefore, the device is referred to as 'salter duck' in the literature [73, 74, 83, 96, 110]. Further, consider multiple such salter ducks held together by a spine in an arc. Retzler analyzed this

by modeling a flexible spine coplanar to the water surface and arching away from the direction of the waves [99].

A.1 Governing Equations

The fluid is assumed to be incompressible, irrotational, and inviscid so that a harmonic velocity potential ϕ exists where Cartesian coordinates system x, y, z is chosen with $z = 0$, the plane of the undisturbed free surface. The linearized free-surface condition is,

$$k\phi + \frac{\partial \phi}{\partial z} = 0 \text{ on } z = 0 \text{ and, } \; k = \frac{\omega^2}{g} \tag{A.1}$$

A harmonic velocity potential describing a wave with amplitude A, making an angle β with the positive x-axis is described by Evans [29] and Retzler [99] as,

$$\phi(x, y, z) = \frac{gA}{\omega} e^{ikx\cos\beta + iky sin(\beta - kz)}, \quad \text{where, } \omega = gk\tanh(kh) \tag{A.2}$$

The phase velocity is given by,

$$\vec{V_p} = \frac{\omega}{k} = \sqrt{gj \tanh{(kh)}} \tag{A.3}$$

In deep water $kh \gg 1$ and $\tanh{(kh)} = 1$, therefore,

$$\begin{aligned} \frac{\partial \phi}{\partial x} &= \frac{gkA}{\omega} e^{kx} \cos{(kx - \omega t)} \\ \frac{\partial \phi}{\partial z} &= \frac{gkA}{\omega} e^{kx} \sin{(kx - \omega t)} \end{aligned} \tag{A.4}$$

The horizontal and vertical velocities differ by $\pi/2$ in phase so that for infinite depths and small waves, the particles move in approximately circular paths with radii decreasing exponentially with depth. For finite depths, particles move in ellipses, which get flatter as the water gets less deep [29, 66].

A.1.1 Hydrodynamics of Multiple Ducks

The general equation for a body oscillating in water can be given by,

$$[\vec{m} + a_{i\omega}]\ddot{\vec{x}} + [b_i(\omega) + c_d]\dot{\vec{x}} + k_i x_i = F_{f_i}(\omega) e^{i\omega t} + F_C(\omega) \tag{A.5}$$

Where the $a_{i\omega}$ denotes the frequency-dependent added mass and $b_i(\omega)$ denotes the

frequency-dependent radiation damping. The quantity added mass denotes the rate at which the body exchanges energy with the waves it creates with its oscillation, whereas $b_i(\omega)$ denotes the rate at which the body radiates energy to the far-field. The excitation force comprises of the diffraction force $F_{f_i}(\omega)$, control force $F_C(\omega)$, and radiation force $F_R(\omega)$.

Haskind relation given by Equation A.6, simplifies Green's second identity to give a relation for diffraction force [37],

$$F_{f_i}(i\omega) = -i\omega\rho \iint \left(\phi_0 \frac{\partial \phi_i}{\partial n} - \phi_i \frac{\partial \phi_0}{\partial n} \right) \tag{A.6}$$

where ϕ_0 is the incident wave potential, and ϕ_i corresponds to the body index in the array. The expression is integrated over S_∞ which represents a cylinder at infinity surrounding the body in the far-field. It is assumed that the velocity flux for radiation ϕ_R and velocity flux for diffraction ϕ_D, are outgoing in the far-field. Salter duck can be considered as a two-dimensional body which can be considered as a beam sea device. If the device crest length is considered L and the far-field radiated wave amplitude is denoted by (A) with subscript UW denoting up-wave and DW denoting down-wave directions, the Haskind relation in Equation A.6 can be simplified to give,

$$F_{f_i}(i\omega) = \rho g \mathcal{A}_{UW}(i\omega) L \tag{A.7}$$

The radiation damping for a single mode i can be given by Haskind-Hanoka relation [29, 37, 66]given by Equation A.7 as,

$$b_i(\omega) = \frac{|F_{f_i}(i\omega)|}{8P_W L\gamma}, \quad \text{where, } \gamma = \frac{|\mathcal{A}_{UW}(i\omega)|^2}{|\mathcal{A}_{UW}(i\omega)|^2 + |\mathcal{A}_{DW}(i\omega)|^2} \tag{A.8}$$

Korde shows that Green's second identity when applied to the radiation potential and just the body disturbed part of the diffraction potential ($\phi_s = \phi_0 - \phi_D$), and the respective conjugates quantitatively link the radiation behavior of the device in calm water to the reflection/transmission of incident waves when the device is held fixed.

$$R(i\omega)\mathcal{A}^*_{UW}(i\omega) + T(i\omega)\mathcal{A}^*_{DW}(i\omega) + \mathcal{A}_{UW}(i\omega) \tag{A.9}$$

The device will experience radiation denoted by $\mathcal{A}_{UW}(i\omega)$ and $\mathcal{A}_{DW}(i\omega)$ and also reflection/transmission as measured by $R(i\omega)$ and $T(i\omega)$. Evans and Korde describe a relation for which describes the efficiency for energy conversion by taking the ratio of power absorbed and the power incident on the device [29, 66],

$$\eta = \gamma - \frac{\mathcal{A}_{UW}(i\omega)a^* - \gamma}{\gamma}, \quad \text{where,} \quad \alpha = \frac{\omega U_i(i\omega)}{gA} \tag{A.10}$$

where $U_i(i\omega)$ denotes the oscillation velocity complex amplitude. Equation A.10

explains the importance of velocity control for efficient energy absorption. If $U_i(i\omega)$ is controlled optimally such that $\mathcal{A}_{UW}(i\omega)a^* = \gamma$, the device can have the maximum possible efficiency such that $\eta = \eta_{max} = \gamma$ [29, 66].

Coming back to the discussion of salter ducks, the geometry of the device entails that the down wave transmissions approach zero, i.e., $\mathcal{A}_{DW} = 0$. This results in γ becoming 1. This is a very appealing feature of the salter ducks as this results in approaching 1, i.e., 100% of the energy can be absorbed by the salter ducks by virtue of geometry. Since multiple salter ducks are considered here, each of the devices will experience a force due to the wave radiated by other devices. Therefore, matrices for radiation damping and added mass must be considered. Due to Newton's III law, reciprocity entails symmetry in radiation damping, added mass, and forces resulting in hydrodynamic coupling. As pointed out by Falnes and Korde, each device can be considered as six oscillators (for 6 DOFs). For N bodies, therefore, there are $6N$ oscillators. Corresponding parameters are then denoted by the subscript i in the following equations such that $i = 6(p-1)+j$, where p denotes the index of the body being considered and j the considered mode. When considering the excitation force, the oscillating body with complex velocity amplitude $\hat{u}_i$ radiates a wave that acts on oscillator i with an additional complex amplitude $-Z_{ii}u_I$. Using the principle of superposition, the total force acting on oscillator i becomes,

$$(\hat{F}_{(t,i)} = \hat{F}_{(e,i)} - \Sigma Z_{ii}\hat{u}_i \tag{A.11}$$

where the sum is taken over all oscillators, including oscillator number i. The complex matrix $\mathbf{Z}$ is the radiation-impedance matrix and can be decomposed in radiation resistance and radiation reactance matrices such that [29]

$$\mathbf{Z} = \mathbf{R} + i\omega\mathbf{m} \tag{A.12}$$

Where $\mathbf{m}$ is the hydrodynamic added mass matrix. Falnes and Kurniawan give a relation for far-field wave elevation as,

$$\eta_{d,r,g} = -\frac{i\omega}{g} C_{d,r,g}(\theta)(kr^{-\frac{1}{2}} + e^{-ikr+\cdots}), \quad \text{as,} \quad kr \to \infty \tag{A.13}$$

where $\eta_{d,r,g}$ denotes diffraction, radiation and outgoing wave elevations. It should be pointed out that the wave elevation $\eta_0 = Ae^{-ikr\cos(\beta+\theta)}$, where β is the angle of the incident wave from the horizontal x-axis. It should be noted that the excitation force is also a function of as the angle of the incident wave becomes crucial because the arched arrangement of the salter ducks on the spine will entail different angles of approach.

A.1.2 Hydrodynamics of the Curved Spine

The dynamics in the pitch mode for a single salter duck is discussed by Count, Cruz et al Lucas et al [17, 20, 73, 74].

The single duck pitches about an off-centered axis. Therefore, the Cummins' equation can be modified to consider the pitch mode and then expanded to consider multiple devices.

If an ideally rigid curved spine is considered, the rigid spine will constrain some degree of freedoms for the device array. Since the spine would be rigid it would allow pitching about it as an axis for the salter ducks. However, the salter ducks would not be able to surge, heave (independent of each other), sway, roll, and yaw about their own body axes. The dynamics of the spine were investigated by Retzler, where he considered the spine to be a beam under bending [99]. For the structure of the beam, two approaches can be taken, such that either the spine is a continuous spine with individual salter ducks hinged on it so that they pitch along a continuous spine; another approach would be to consider the curved spine connecting only the adjacent ducks. If the spines are considered to be a beam, bending would occur in the horizontal local x direction and the vertical local z direction. For the salter ducks, this would result in an additional surge and heave displacements along with a yaw

and roll angular displacements respectively. Considering the crest of the wave long enough such that it doesn't result in twisting torsion in the spine beams, the spine would not add to the pitch of the salter ducks. However, the pitching of the salter ducks would introduce some torsional twists in the spine depending on the relative difference of the pitch angular displacement of adjacent salter ducks. If the crest of the wave is considered long enough and the relative capture length of the salter ducks is less than the length of the spine connecting them, axial displacements of the beam and hence sway on the salter ducks, due to the wave-induced axial displacement of the beam can be ignored. However, sway in the salter duck may be introduced due to the axial displacement in the spine caused by the relative difference in the surge of other salter ducks. The shear in the spine would not be considered as the difference in the force acting upon different points on the beam facing the incident wave can be ignored to cause shear on the spine.

A.1.3 Dynamics of Bending Spine

Retzler considers the beam model for the spine in the horizontal local x axis (normal to the axis of the spine) where the incoming wave makes an angle β with the x-axis [98, 99]. Defining the equations of motion in x direction for a beam of elasticity E

and sectional moment of inertia I, one can write,

$$F = -EI\frac{\partial^4 x}{\partial y^4} \tag{A.14}$$

Where length of the spine is along y-axis and x-axis is normal to the axis and in the plane of $z = 0$. Therefore, the dynamics equation can be expressed as,

$$-(\mathbf{m_b} + \mathbf{a_{b,m}})\ddot{x} - Z\dot{x} + EIx^{iv} = W_{xx}A_{xx} \tag{A.15}$$

Where, $\mathbf{m_b}$ is the mass of the beam, $a_{b,m}$ denotes the frequency-dependent added-mass, Z is the impedance damping and includes the frequency-dependent radiation damping term, iv denotes the fourth differential of x, W denotes the wave force coefficient and A denotes the wave amplitude. Defining k as the wave number such that

$$k = \frac{2\pi \sin\beta}{\lambda} \tag{A.16}$$

where β is the wave angle to x-axis. The fourth order linear non-homogeneous equation in x (Equation A.14) can be solved by undetermined coefficients. Assuming steady state sinusoidal conditions the force can be expressed as $WA_0e^{i(t-ky)}$. Therefore

$$x = x_0e^{i(t-ky)} \;\; ; \dot{x} = i\omega x; \ddot{x} = -\omega^2 x; x^{iv} = k^4 x(28) \tag{A.17}$$

Therefore, rewriting in frequency domain as,

$$-(\mathbf{m_b} + \mathbf{a_{b,m}})\omega^2 x - Zi\omega x + EIk^4 x = W_{xx}A_{xx} \tag{A.18}$$

And,

$$x = \frac{W_{xx}A_{xx}}{(\mathbf{m_b} + \mathbf{a_{b,m}})\omega^2 - Zi\omega - EIk^4} \tag{A.19}$$

Equation A.19 indicates that resonance would occur when the inertia term is canceled by its added spring term. The homogenous equation given by Equation A.19 can be solved by substituting $x = x_0 e^{\mu y}$

$$(\mathbf{m_b} + \mathbf{a_{b,m}})\omega^2 x_0 e^{\mu y} - Zi\omega x_0 e^{\mu y} - EIk^4 x_0 e^{\mu y} = 0 \tag{A.20}$$

$$\mu = \sqrt[4]{\frac{(\mathbf{m_b} + \mathbf{a_{b,m}})\omega^2 - Zi\omega}{EI}} \tag{A.21}$$

Using De Moivre's theorem

$$x = x_0 e^{i\omega t}[e^{-iky} + \Sigma_0^3 C_j e^{\mu j y}] \tag{A.22}$$

The four coefficients $C_{0,1,2,3}$ can be worked out by using the boundary conditions such that, at the ends of the beam, the bending moments and the shears must be zero

$$EI\frac{\partial^4 x}{\partial y^4} = 0; \quad z = 0, L; \quad EI\frac{\partial^3 x}{\partial y^3} = 0; \quad z = 0, L \tag{A.23}$$

The four boundary conditions help in the solution for unknowns in C such that,

$$\begin{aligned}\left[\frac{\partial^2 x}{\partial y^2}\right]_0^L &= x_0\left[-k^2 e^{-iky} + \Sigma_0^3 C_j \mu_j^2 e^{\mu j y}\right]_0^L = 0 \\ \left[\frac{\partial^3 x}{\partial y^3}\right]_0^L &= x_0\left[ik^3 e^{-iky} + \Sigma_0^3 C_j \mu_j^2 e^{\mu j y}\right]_0^L = 0\end{aligned} \tag{A.24}$$

By elimination and substitutions with μ, values of x as a function of time and distance y down the spine can be worked out. For each axis frequency-dependent values need to be substituted accordingly, along with the respective mass and elasticity of the beam. Respective wave parameters such as ω, A and k (using $\omega^2 \sin\beta/g$ for deep water) are also respectively substituted. As discussed at the beginning of this section, bending would also occur in the vertical local z direction. The relations in the z-direction will have a similar form. However, there would be a difference in wave amplitude A in the surge and heave modes. Retzler points out that the amplitude in heave mode will be a constant, but in surge mode its multiplied by the cosine of the wave angle such that,

$$A_s = A_h \cos\beta \tag{A.25}$$

Retzler refers to Garrison's work in deducing that each strip of the beam is unaffected by its neighbor using strip theory until radiated wave angles are such that crest lengths are in the comparable order of the spine's beam segment, this corroborates the assertion made in the beginning of this section [48, 99]. Using beam theory, the moment M for the beam can be given by,

$$M = \frac{EI}{R} \tag{A.26}$$

Where R is the radius of curvature of the beam and is large, the angle θ gives the angle of a spine joint, given the pitch of the joints is h such that,

$$\theta = \frac{h}{R} \tag{A.27}$$

Given the spine has stiffness $\sigma\ Nm/rad$

$$M = \sigma\theta, \quad \text{then,} \quad MR = \sigma\theta\frac{h}{\theta} = \sigma h = EI \tag{A.28}$$

Similarly, if joint damping is then beam damping becomes h. the aggregate relation for flexural rigidity can therefore be given by,

$$EI = h\left(s_r + \frac{1}{\frac{1}{\sigma} + \frac{1}{s_t}}\right) \tag{A.29}$$

where, s_r is the reference spring, commanded spine stiffness is given by σs and intrinsic

stiffness of the spine segment is s_t. Therefore, the final equation for bending moment can be given by,

$$M = (\sigma + i\omega\delta)h\frac{\partial^2 x}{\partial y^2} \tag{A.30}$$

The above relations can then be used for a similar analysis in the heave mode i.e. z direction. From above discussion, it can be deduced that resonance will occur in the spine when the spring terms cancel the inertial terms and the impedance. The value of k increases with angle of incidence reaching a peak at $\beta = \pi/2$. Therefore, with drop in frequency the resonance moves to larger angles of incidence, but since β is limited to $\pi/2$ there will be a frequency below which no resonance will occur. From above relations, it can also be seen that at 0 wave angle the k will also become 0 and therefore no bending will occur. Also, at resonance, $(\mathbf{m_b} + \mathbf{a_{b,m}})\omega^2 = (EI + \text{added spring})k^4$. Therefore, the bending moment at resonance is proportional to $\sqrt{EI}$. Retzler further expands the continuous beam model as a discrete model and works out a nodal analysis, such that the spine is segmented and not continuous.

A.1.4 Torsion due to pitching salter ducks

Since the incident wave approaches at an angle and due to the distance separating the salter ducks, the salter ducks would not pitch in phase, such that the pitch angular displacements for adjacent salter ducks will be different. The difference in

the pitch angular displacement will introduce a twist in the connecting spine beam. The pitch angular displacement was expressed earlier as for a single duck. Therefore, the difference between two adjacent salter ducks' pitch angular displacement can be given by, $\epsilon_n - \epsilon_{n+1} = \partial\epsilon$. Therefore, the torsion for the horizontal spine can be given by [21],

$$T = GJ_t \frac{\partial \epsilon}{\partial y} \tag{A.31}$$

Where, J_t is the torsional parameter which is $\pi r^4/4$ for a solid circular cross section and G is the torsional modulus. Therefore, the torsional dynamics equation can be given by,

$$-(\mathbf{m_b} + \mathbf{a_{b,m}})\ddot{\epsilon} - Z\dot{\epsilon} + G\frac{\pi r^4}{4}\frac{\partial \epsilon}{\partial y} = 0 \tag{A.32}$$

As for bending discussed above one can write,

$$\epsilon = \epsilon_0 e^{i(\omega t - ky)}; \quad \dot{\epsilon} = i\omega\epsilon; \quad \epsilon^i = k_t x \tag{A.33}$$

Therefore, the dynamics equation can be rewritten as,

$$(\mathbf{m_b} + \mathbf{a_{b,m}})\omega^2\epsilon - Zi\omega\epsilon - GJ_t k_t \epsilon = 0 \tag{A.34}$$

A.1.5 Effect of bending moment of spine on salter ducks

As discussed earlier in this section, the bending of the spine in surge mode will entail yaw and surge effects. The angle θ represents the angle at the ends of the spine due to bending. θ can be accommodated in the displacement matrix in the time domain by adding to the salter duck's yaw angular displacement using the principle of superposition. The resulting additional small surge due to bending can be calculated by multiplying the distance of the point at which the spine is attached to the salter duck and the distance to the center of the salter duck such that the added surge term in the matrix becomes $\theta l/2$ (where l is the capture width of the salter duck). Similarly, in the heave mode, the heave of the spine due to bending in z direction will entail roll and heave effects on the salter duck. This workflow can be analogously used to work out the angle α at the ends of the spine due to bending. The small-angle α can be added to the roll angular displacement of the salter duck, and $\alpha l/2$ will be added to the heave displacement for the Salter duck displacement matrix using the

principle of superposition, such that,

$$\mathbf{x} = \begin{bmatrix} x + \theta l/2 \\ y \\ z + \alpha l/2 \\ \psi_1 \\ \psi_2 + \theta \\ \psi_3 + \alpha \end{bmatrix} \tag{A.35}$$

Where, $\mathbf{X}$ denotes the displacement matrix, which can then be plugged back in the dynamics equations discussed above. ψ_1 denotes the pitch angular displacement, ψ_2 is the roll angular displacement, and ψ_3 is the yaw angular displacement. The spine will also contribute to the hydrodynamic coupling and can be treated as an additional dynamically coupled body. The hydrodynamic coefficient matrices for frequency-dependent added-mass and frequency-dependent radiation damping can be numerically calculated using WAMIT.

A.2 Numerical Model for Salter Duck Array

A.2.1 Model Description

As discussed in the previous section a salter duck would encounter hydrodynamic couplings such that the motion in different degrees of freedom gets coupled with each other. When we analyze multiple such ducks, the motion in different degrees of freedoms of one duck would also get coupled with the motion of other salter ducks in their different degree of freedoms. The hydrodynamic coefficients can be calculated using the WAMIT package. This analysis will consider three such salter ducks arranged in an arc such that the arc is concave with respect to the incoming waves. A simple sinusoidal wave will be considered. Complex conjugate control will be used for the control force. Power generated due to pitch motion over a 10 second period will be calculated using the mean velocity and force for the pitch degree of freedom. The arc mooring interaction is not considered; therefore, the analysis will effectively consider an array of salter ducks in an arc. The discussion in previous sections can consider such moorings but would require a more thorough definition of moorings. Also, the WAMIT package cannot analyze multiple bodies of different geometries but can do calculations for an array of single body geometries.

A.2.2 Model Setup

WAMIT requires a geometric mesh file of the body under consideration. The geometry for a salter duck was described parametrically. The geometry was defined such that the two faces of the beak of the salter duck make an angle of 45° or $\pi/4$ rad with each other. The two faces are also tangential to the hub cylinder. Using sine triangle laws, the top extension of the beak that is the posterior side can be expressed as $x = R\frac{\sin(3\pi/8)}{\sin(\pi/8)}$ and the extension of the anterior face of the beak can be expressed as $d = \frac{R}{\sin \pi/8}$.

The mesh file needs a discretized definition of the geometry. This discretization was done using the NEMOH package, which can then be used as an input for the WAMIT package to generate the hydrodynamic coefficients. However, WAMIT could not solve the hydrodynamics for the body and ran into stack overflows. Similar problems were encountered by Lucas et al., and Lucas resolved this by considering a horizontal cylinder with an off-centered axis [74]. Lucas verified this approach using experimental testing and concluded that such a horizontal cylinder is a very close approximation of the salter duck geometry [73]. The equivalent horizontal cylinder is described such that the equivalent radius is $R_e = \frac{R - \frac{R}{\sin(\pi/8)}}{\cos \pi/8}$ and the offset of the axis of rotation e is: $e = R_e - R$.

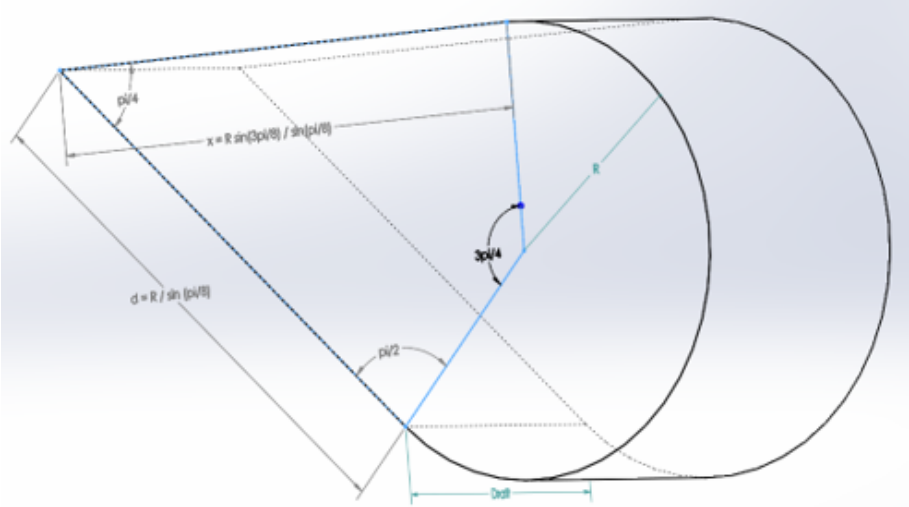

Figure A.1: The modified Salter-Duck geometry was used for this work.

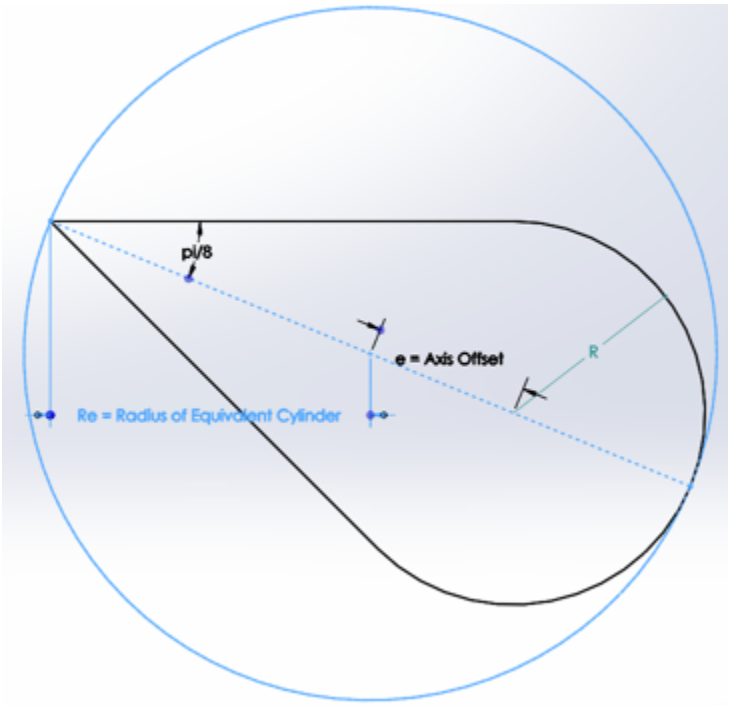

Figure A.2: Equivalent cylinder

The equivalent horizontal cylinders were described as a discretized mesh file, and three of them were arranged in an arc such that they made an angle of 60° with the adjacent duck from the center of the arc. As shown in Figure A.4, the mesh file was

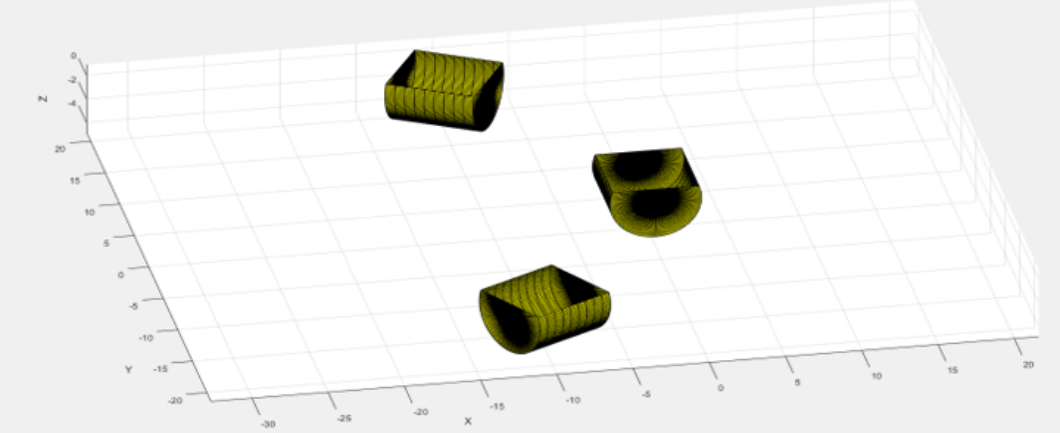

Figure A.3: The Salter Duck WEC array is used for the numerical modes=ls.

thus used as the input mesh file for WAMIT.

A.2.3 Hydrodynamic coefficients and Performance

The operating parameters were set such that the mean power could be compared to the results by Lucas. The diameter of the body was set at 6 m, and a sinusoidal wave of amplitude 0.1 m was used to run the simulations. The frequency for the incoming wave was varied from 0 to 5 Hz with graduations of 0.1 Hz.

The comparison of hydrodynamic coefficients and velocities shows that the central Salter Duck has higher numerical values of hydrodynamic coefficients. This translates to higher velocities and power profiles. The increase in hydrodynamic coefficients can be ascribed to the trapping-effect described by Sir Taylor et al. and is observed and discussed in Chapters 4 and 5.

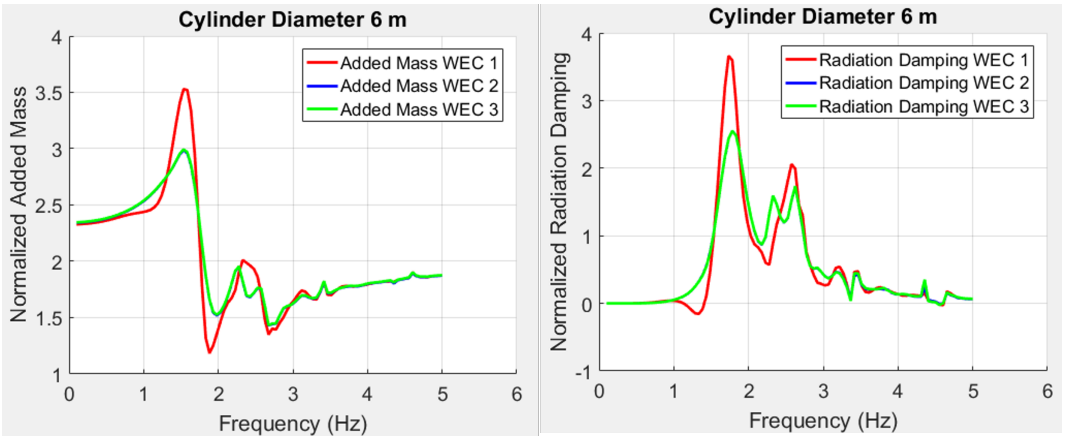

Figure A.4: The hydrodynamic coefficients of the Salter Duck WEC array. The normalization is done by dividing the added mass and radiation damping terms by the mass of the fluid displaced by the WEC body.

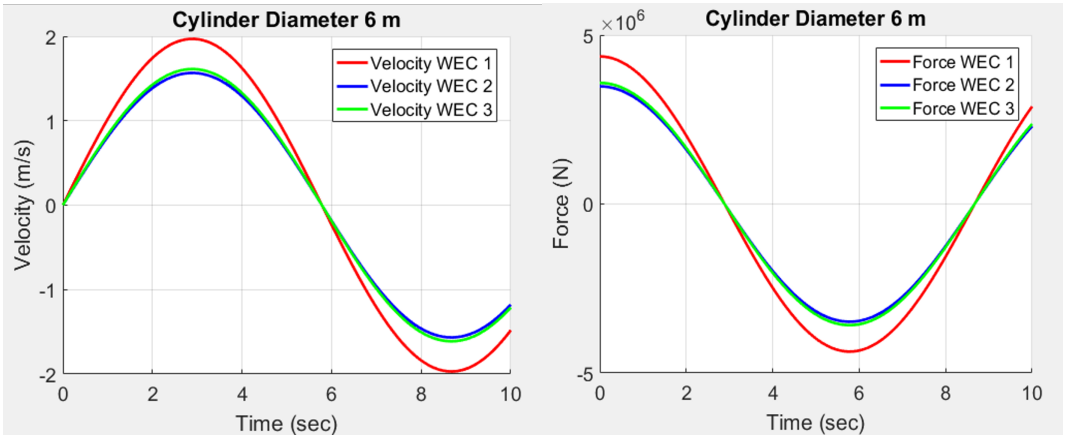

Figure A.5: Velocity and control force as a function of wave frequency. The control force was calculated using complex-conjugate control.

	WEC 1	WEC 2	WEC 3
Mean Reaction Force (off-center axis)	1.4 MN/m	1.12 MN/m	1.15 MN/m
Mean Absorbed Energy	1.48 GWh	0.93 GWh	0.98 MN/m

Table A.1
Performance characteristics of Salter Duck WEC array. WEC 1 was the central Salter Duck whereas WEC 2 and 3 were the peripheral Salter Ducks

The mean reaction force at the off-center axis was 1.59 MN/m according to work done by Lucas for a cylinder of diameter 6 meters. In contrast, the mean absorbed energy

was 0.5 GWh for a cylinder of radius 6 meters. The discrepancy can be attributed to the fact a regular sine wave was used for this analysis, whereas Lucas used the Bretschneider spectrum.

A.3 Conclusions

The hydrodynamics for wave energy converters in terminator configuration was analyzed. The hydrodynamics of salter ducks was looked into more closely. Relations were developed for an array of salter ducks moored together with a flexible spine in an arc layout. For the simulation analysis, the spine was assumed to be rigid and therefore constraining roll, yaw, heave, surge, and sway degree of freedoms. Analysis was done for a simplified yet equivalent model for a salter duck array of three devices. This analysis focused on the pitch degree of freedom and its hydrodynamic coupling due to multiple devices. For this analysis, the reactive forces, velocity, and power generated was calculated and compared to the analysis done by Lucas [73, 74]. Comparable results were obtained. The results highlighted the importance of array layouts and alluded that WEC devices can have better performance in an array. The simulation results from this analysis of multiple devices were relatively better than those from work done by Lucas for a single device. This is further corroborated by the better performance of the central device in the arc layout since the central device had the other two devices closer to itself as compared to the devices surrounding the

peripheral devices. It also became clear that the angle of approach of waves is critical to devices in terminator configuration. A mooring arc that has some flexibility with some control can, therefore, potentially substantially enhance performance by changing these angles of attack. Further work would entail the integration of hydrodynamics due to a flexible spine and the constraints it would impose, especially on the surge and heave degree of freedoms. The design of the spine would have to be optimized such that it enhances favorable mode couplings and enhances performance. A controller for this mooring arc can potentially significantly enhance performance. The terminator salter ducks have significantly higher efficiency than other devices, but this advantage gets reduced if the angle of attack of the waves is non-favorable. This can be mitigated by a controllable spine that optimizes the approach of the incoming waves.

Appendix B

Convergence Studies of BEM-code Generated Hydrodynamic Coefficients

The hydrodynamic coefficients generation from a BEM-code like WAMIT can be computationally expensive. The computational costs are closely related to the mesh discretization of the geometry of the floating structure. Convergence studies are recommended when conducting BEM runs to investigate the trade-offs associated with mesh discretization, computational costs and computational precision [59]. The Response Amplitude Operator (RAO) of a floating body requires the knowledge of hydrodynamic coefficients and the hydrostatic stiffness. Therefore, the RAO can be

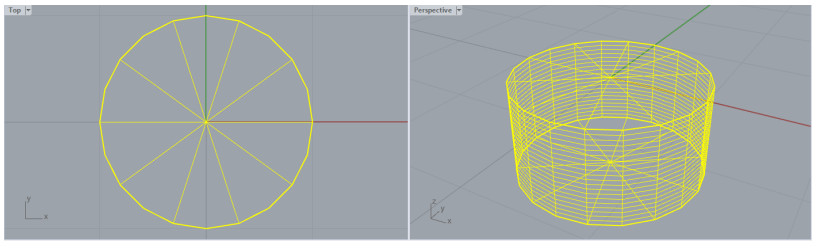

Figure B.1: The cylinder discretized using 420 panels.

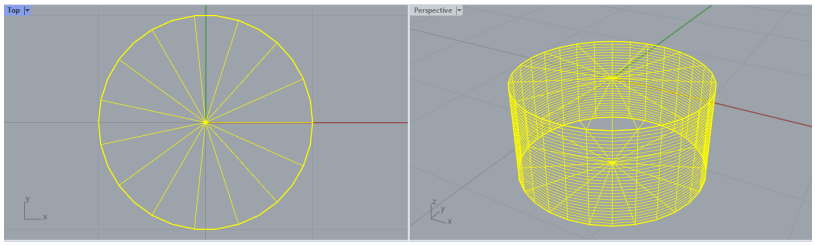

Figure B.2: The cylinder discretized using 930 panels.

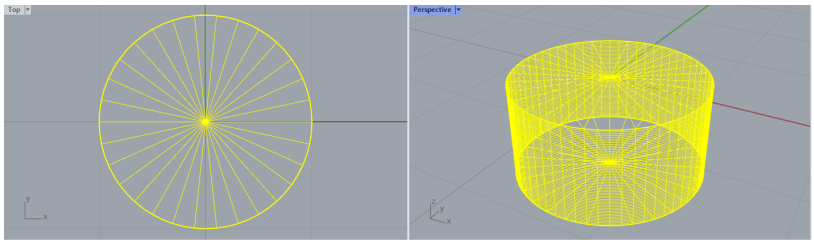

Figure B.3: The cylinder discretized using 3660 panels.

used as a measure for the convergence of magnitudes and phases for the computed hydrodynamic coefficients [50]. Over the years several researchers have compared and found WAMIT as a reliable BEM modeling platform for WECs, and used the WAMIT generated results to evaluate the performance of other BEM codes such as NEMOH and Capytaine developed at École centrale de Nantes [2, 60, 89].

The RAO for a floating body using the hydrodynamics coefficients introduced in Section 3 can be expressed as [37],

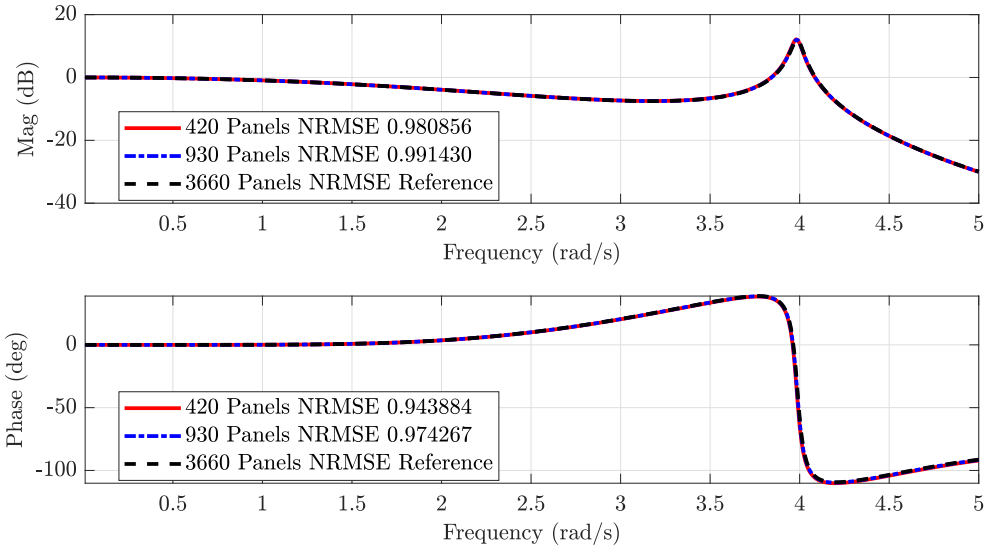

Figure B.4: The RAO magnitude and phase for a cylinder discretized using 420, 930, and 3660 panels.

$$\zeta_i(j\omega) = \frac{F_{fi}(j\omega)}{-(m_i + a_i(\infty)\omega^2 + j\omega b_i + k_i} \tag{B.1}$$

where, $\zeta_i(j\omega)$ is the displacement RAO, and $F_{fi}(j\omega),\ a_i(\infty),\ b_i,\ k_i$, are the excitation force, added mass at infinity, radiation damping, and hydrostatic stiffness respectively. Consider a cylinder of radius 1 m and draft 1 m. The said cylinder was discretized using 3660, 930, and 420 panels. Figures B.1-B.3 show three different discretization resolutions. The mesh resolution was controlled using Rhinoceros 3D [78]. On closer inspection, it can be observed that the cylinder with the lowest resolution mesh could not achieve the curvature observed at higher mesh resolutions. The RAO for the three discretized cases was evaluated by comparing the NRMSE for the cases with 420 panels and 930 panels against the case with 3660 panels. Figure B.4 shows the

comparison of magnitude and phase of the RAO. This comparison is indicative of the typical recommended workflow for BEM based computations [133]. Additionally, for simple geometries analytical closed-form solutions can further increase confidence in the numerically computed hydrodynamic coefficients.

Appendix C

Letters of Permission

This appendix shows the relevant permissions to reuse content. The first permission letter corresponds to Chapter 4 reusing content from [56]. The second permission letter corresponds to Chapter 6 reusing content from [57].

Figure C.1: Permission to use the content from IEEE explore

Michigan Tech

Sal Husain <shusain@mtu.edu>

[JMSE] Manuscript ID: jmse-1541636 - Open Access Details

Szabolcs Szima <szima@mdpi.com> Mon, Feb 14, 2022 at 4:28 AM
To: Sal Husain <shusain@mtu.edu>
Cc: jmse@mdpi.com

Dear Mr. Husain,

Thank you for your email.
Our journal is an Open Access journal, meaning that all articles are made available to the public after publication. Regarding your request to reuse the content of your published article, we can assure you that since this is published under an open access Creative Common CC BY license, any part of the article may be reused without permission, provided that the original article is clearly cited. For additional information please visit the following website:

https://www.mdpi.com/openaccess

Regarding the issue with your ORCID, we apologise for the inconvenience, our department that handles edits after publication has been notified about the mistake and this will be corrected shortly.

Published articles usually take a few weeks to be indexed but this period can be as high as 4 - 8 weeks. As Google Scholar is an independent identity, we cannot give you an exact time-frame when your publication will appear in their database.

Thank you for choosing JMSE as a venue of your research. If you have any other questions, don't hesitate to contact us.

Kind regards,
Dr. Szabolcs Szima
Assistant Editor, MDPI Romania
Avram Iancu 454, 407280 Floresti, Cluj, Romania
Tel.: +40 0364 150134
Email: szima@mdpi.com

Disclaimer: MDPI recognizes the importance of data privacy and protection. We treat personal data in line with the General Data Protection Regulation (GDPR) and with what the community expects of us. The information contained in this message is confidential and intended solely for the use of the individual or entity to whom they are addressed. If you have received this message in error, please notify me and delete this message from your system. You may not copy this message in its entirety or in part, or disclose its contents to anyone.

On 2/11/2022 9:12 PM, Sal Husain wrote:
> Dear Dr. Szima,
> Hope you are doing well.
>
> I wanted to request the journal to give me permission to use the content
> of the paper in my dissertation. If you could please issue a letter or a
> statement that confirms
> this, it would be most appreciated.
>
> Also, I wanted to check in with you on the ORCID issue. Looks like it
> hasn't been updated yet. I was curious when would the paper be available
> on Google Scholar?

Figure C.2: Permission to use the content from Journal of Marine Science and Engineering